HI SURVEY OF LOCAL GROUP DWARF GALAXIES

By

BRENDA NAMUMBA

Dissertation submitted in fulfillment of the requirements for the degree of Doctor of Philosophy

in the
Faculty of Science
Department of Astronomy
University of Cape Town

March 2019

Supervisor:
Prof. C. Carignan (University of Cape Town)

TABLE OF CONTENTS

AUTHOR'S DECLARATION

I, Brenda Namumba, know the meaning of plagiarism and hereby certify that all the work in this document, save for that which is properly acknowledged, is my own.

SIGNED: Signed by candidate DATE: March 2019

ABSTRACT

This thesis investigates the HI properties of 3 dwarf irregular galaxies and one blue compact dwarf galaxy of the Local Group. The data set of each dwarf irregular galaxy was obtained with the Karoo Array Telescope (KAT-7) while the blue compact dwarf was observed with the Dominion Radio Astrophysical Observatory (DRAO) synthesis telescope. While the main purpose of KAT-7 was to test technical solutions for MeerKAT, its capabilities, and that of DRAO, have enabled us to produce interesting Square Kilometer Array (SKA) pathfinder science. The compact configuration of the two telescopes, coupled with low system temperatures (T_{sys}) provide a unique HI dataset on nearby dwarf galaxies; sensitivity to extended HI emission while providing intermediate resolution to derive the large scale kinematics. The following properties are investigated in details: i) the HI distribution, ii) kinematics and mass distribution, iii) star formation thresholds, and iv) possible mechanisms for the chaotic HI structure and kinematics in a blue compact dwarf galaxy.

The main results of our study are: from the HI distribution, the KAT-7 results have revealed even more neutral gas mass in the outer disk of NGC 6822. We detect 23% more HI mass in NGC 6822 than what was detected with the Australian Telescope Compact Array (ATCA). The KAT-7 results have been able to show an overestimate of the HI extent previously reported for Sextans A using Effelsberg observations. For IC 10, the complex HI features detected with DRAO are by a factor of ~ 2 more extended than previous interferometric HI studies.

Rotation velocities are derived for each galaxy. For NGC 6822, the rotation curve probes the gravitational potential out to 5.8 kpc, ~ 1 kpc further than existing measurements. The rotation curves of Sextans A and B decline in the outer regions and extends out to 3.5 kpc and 4 kpc respectively. The central region of IC 10 has a regularly rotating disk, and the rotation velocities rise slowly in the inner region < 0.35 kpc. Beyond this radius the velocities are almost constant until the last point where it rises again reaching a maximum velocity of ~ 30 km s^{-1}.

Mass models are used to describe the distribution of dark matter. The dark matter models used are the Navarro-Frenk and White (NFW) and pseudo-isothermal (ISO) sphere. The dark matter distribution in dwarf irregular galaxies is better described by the ISO model when a mass to light ratio of 0.2 is used. This M/L value was derived for the Spitzer 3.6 μm band surface brightness profiles. The galaxies are dark matter dominated at all radii, and the stellar potential is insignificant to account for the total observed kinematics. In the case of IC 10, the kinematics of the inner disk can be described without the need of a dark matter halo. This result does not exclude the possible presence of dark matter on larger scales.

Critical densities for gravitational instabilities are calculated using a one-dimensional Toomre-Q and cloud-growth based on shear criterion for the 3 dwarf irregular galaxies. In all cases, we find that in regions of star formation, the cloud growth criterion based on shear explains better the star formation. This suggests that the local shear rate could be a key player in cloud formation for irregular galaxies.

Simulations are carried out to investigate if an interaction between IC 10 and M 31 can reproduce the observed HI morphology and kinematics of IC 10. The simulations are carried out using the GALACTICS code. From these simulations, it is unlikely that the HI features we see in IC 10 are caused by an interaction with M 31. The features seen in the simulations are both larger and at lower column density than what can be reached by current observations. The HI extensions with different kinematics seen south, east and west of the main core of IC 10 are more likely the result of accretion.

I confirm that I have been granted permission by the University of Cape Town's Doctoral Degrees Board to include the following publications in my PhD thesis, and where co-authorships are involved, my co-authors have agreed that I may include the publications:

Chapter 2: Namumba, B., Carignan, C., Passmoor, S., de Blok, W.J.G. 2017, HI Kinematics, Mass Distribution, and Star Formation Threshold in NGC 6822, using the SKA pathfinder KAT-7, Monthly Notices of the Royal Astronomical Society, 472, 3761. This chapter has been published in the Monthly Notices of the Royal Astronomical Society Journal.

In this chapter, I present a detailed study of the HI properties of NGC 6822 with KAT-7. Data calibration and reduction were done by myself under the supervision of my supervisor and Dr. Sean Passmoor. I describe, in detail, the tilted ring model, mass models, and star formation threshold models that have been used in this study. I compare the KAT-7 results with previous NGC 6822 results obtained with ATCA observations.

Chapter 3: Namumba, B., Carignan, C., Passmoor, S. 2018, HI observations of Sextans A and B with the SKA pathfinder KAT-7. Monthly Notices of the Royal Astronomical Society, 478, 487. This chapter has been published in the Monthly Notices of the Royal Astronomical Society Journal.

In this chapter, I present the study of the HI distribution, kinematics, and star formation thresholds of Sextans A & B with KAT-7. KAT-7 data reduction and calibration was done by myself using a software package CASA. Results obtained from this study have been compared with the LITTLE THINGS data on Sextans A & B obtained using the VLA.

Chapter 4: Namumba, B., Carignan, C., Foster, T., Deg, N. 2018, HI observations of IC 10 with the DRAO synthesis telescope. This paper has been submitted to the Monthly Notices of the Royal Astronomical Society and is awaiting comments from the reviewer.

In this chapter, we present new HI observations of IC 10 from the DRAO synthesis telescope. The HI distribution of the extended HI disk and the kinematics of the inner disk of IC 10 are presented. We ran simulations to investigate if an interaction between IC 10 and M 31 can reproduce the complex HI structure of the outer disk of IC 10.

Signed by candidate	March 2019
Signature	Date
Brenda Namumba	NMMBRE001
Student name	Student number

DEDICATION

Kuwakwasi wane,
John Simumba ne Edah Namuwelu,
mwampa amano yomwawanayo,
inchito yo ikulanjizya ulukundo lwinu na vyonsi vyo mwasambilizya.
Nachita inchito yo kwe mwemwe nulukundo!

To my parents,
John Simumba and Edah Namuwelu,
you passed a set of exceptional genes to me,
this work is a sign of your endless love, support and encouragement.
I dedicate my PhD research thesis to you with love!

ACKNOWLEGEMENT

This journey has been a life-changing experience for me and it would not have been possible without the help and presence of many people in my life. First and foremost, I would like to thank God, the Almighty for giving me strength, knowledge, and good health throughout my research work. It is by your grace that I could travel through this endeavor successfully.

I consider myself fortunate indeed to have had an opportunity to pursue my Ph.D under the supervision of *Prof. Claude Carignan*. I am grateful for his invaluable guidance throughout this research. His presence, empathy, enthusiasm, immense knowledge, and great sense of humor have deeply inspired me. He has taught me how to carry out research and present work as clearly as possible. I remember many times when I felt discouraged and unsure of the worth of my own work. It was he who never failed to offer encouragement and support. Je n'aurais pas imaginé avoir un superviseur et guide aussi merveilleux pour mes études doctorales. Merci beaucoup!

I wish to extend my thanks to my collaborators: I am indebted to *Dr. Sean Passmoor* for taking time from his busy schedule to attend to me whenever I needed help. His in-depth discussion and guidance on data reduction skills and various research problems helped me accomplish my project. It has certainly been a pleasure working with you for my PhD. Thank you!

Dr Erwin de Blok, I acknowledge the incredible value of having a chance to collaborate with you on NGC 6822, your thoughts and support are much appreciated. Thank you for being very accommodative in my visit to ASTRON. Dank je!

Special thanks goes to *Dr. Tyler Foster*, *Dr. Kothes Roland*, *Dr. Gray Andrew*, and the entire team at the DRAO observatory for going an extra mile to ensure that I had IC 10 data on time. *Tyler*, your quick response to emails is very much appreciated. I am grateful!

Dr. Nathan Dag, thank you for sparing time from your busy schedule to collaborate with me on my last project, not forgetting the many times I have been to your office to ask for help on various research problems. Thank you for being accommodating!

Last but not the least, many thanks to my loving parents. You gave me an opportunity to choose my path and you have been my pillar throughout my journey. I am forever grateful to have you in my life. To my brothers John, Sailas, and James, much love for you guys. Your chats always made me feel closer to home. Natasha baiche! To all my friends, too many to mention, thank you all for being part of my journey. I love you all!

TABLE **Page**

FIGURE **Page**

CHAPTER 1

INTRODUCTION

Understanding how galaxies form, evolve, and interact with one another is of fundamental astrophysical interest. The formation and evolution of galaxies depend on a diverse suite of factors such as star formation and the environment in which the galaxies exist. These factors are often seen in form of feedback, gas accretion, dynamical interactions, or mergers and are clearly visible in the outskirts of galaxies. There are many different approaches for studying the evolution of galaxies and one of the most reliable is to look at the physical parameters of galaxies using their neutral hydrogen gas (HI). This is because hydrogen (in its molecular form H_2), the raw material from which stars form, plays an important role in the various processes that occur in galaxies. Much of what we can infer on galaxy formation and evolution is founded upon our knowledge of nearby galaxies. The close proximity of nearby galaxies allows us to resolve these objects, making it possible to obtain an unobscured view of the properties of the emitting gas and the overall dynamics of the InterStellar Medium (ISM). Nearby dwarf galaxies provide a unique opportunity to address key science questions regarding galaxy evolution. They are the least massive, yet most numerous galaxies found in the universe. In the cold dark matter (CDM) paradigm of hierarchical galaxy formation models, larger and more metal rich galaxies were formed by the merger of smaller galaxies (e.g, Navarro et al. (1995)). Therefore, dwarf galaxies are similar to the small original disks that formed larger galaxies. Analyzing their HI content is critical to further our understanding of their origin and evolution, clarifying their role in the context of current galaxy formation and evolution paradigms.

Nearby dwarf irregular galaxies (dIrrs) are prime HI observational targets for

studying the fundamental processes driving both star formation and the evolution of galaxies. This is because these galaxies are among the most prevalent star forming systems and have a relatively simple structure (they lack a dominant bulge or spiral arms), making it easier and reliable to determine the physical processes occurring in them.

In most cases, dwarf irregulars have HI reservoirs that extend to larger radii than the visible stars. Examples of such studies include; e.g., Huchtmeier et al. (1981); Wilcots & Miller (1998); Gentile et al. (2007); Kreckel et al. (2011); Schmidt et al. (2014). The HI rotation curves (RCs) derived from the extended HI disks have been able to give strong evidence for dark matter (e.g., Carignan & Purton (1998)). Many previous interferometric observations lack the sensitivity to detect the extended HI disks in dIrrs. Examples of such modest sensitivity studies include; Skillman & Bothun (1986); Côté et al. (2000); de Blok & Walter (2000); Kreckel et al. (2011); Hunter et al. (2012). Single dish observations are ideal for tracing the full HI extents as these instruments do not filter out any emission (Pisano, 2014; Stanimirovic, 2002). However, these instruments lack the spatial resolution to derive the kinematics of the galaxies. To address this problem, interferometers with short baselines that have better spatial resolution and are sensitive to large scale structures are well suited to such work.

A new generation of radio telescopes is being built. Examples include the Square Kilometer Array (SKA), which will be the world largest radio telescope. The SKA will provide a unique combination of sensitivity, speed, and resolution, allowing it to revolutionize the fields of study of galactic evolution. As we wait for the completion of the final phase of the SKA, its pathfinders such as the Karoo Array Telescope (MeerKAT), the Australian SKA pathfinder (ASKAP), and the Aperture tile in focus (Aperitif) focal plane array in the Netherlands are being built as a test bed for the SKA. In preparation for MeerKAT, South Africa built an engineering test bed array, the Karoo Array Telescope (KAT-7) (Carignan et al., 2013) which was completed in December 2010. The array was built with compact baselines (26 to 186 m) coupled with low system temperature ($T_{sys} \sim 26$ K) (Foley et al., 2016). While the main purpose of KAT-7 was to test technical solutions for MeerKAT, its unique capabilities allowed astronomers to produce cutting-edge early SKA science. The KAT-7 provided a unique dataset of observations of nearby galaxies. Its compact baselines and low system temperature provided the sensitivity to detect large scale extended HI structures while its intermediate spatial resolution allowed us to study the kinematics of nearby galaxies (high resolution arrays and single dish telescopes can produce data either with better resolution or high sensitivity but not both). This work used the KAT-7 and DRAO (Dominion Radio Astronomical Observatory) telescopes to study the physical properties of HI gas in nearby gas rich dwarf galaxies.

Table 1.1: Largest angular sizes (LASs) of different synthesis telescopes.

Telescope	B_{min} (m)	Ant. diam (m)	LAS min. baseline (arcmin)	LAS shadow lim. (arcmin)
1	2	3	4	5
DRAO	13	9.0	33.4	48.1
KAT-7	26.0	12.0	16.7	36.1
ATCA	31.0	22	14.0	19.7
VLA-D	35.0	25	12.4	17.3
WSRT-MS	36.0	25.0	12.0	17.3
GMRT	100.0	45	4.3	9.6

Notes. Column (1) gives the telescope name, column (2) the minimum baseline, column (3) the antenna diameter, column (4) LAS from the minimum physical baseline, and column (5) LAS down to the shadowing limit.

As illustrated by Lucero et al. (2015), the limit of an interferometer to detect the Largest Angular Sizes (LAS) depends on its minimum baseline (B_{min}).

$$\mathrm{LAS} = \frac{\lambda}{B_{min}} \tag{1.1}$$

where λ is the observing wavelength. Table 1.1 shows why KAT-7 and DRAO are suitable instruments for observing LAS. For example, if we consider the shortest physical baseline of KAT-7, its gain is ~ 33 per cent over the VLA, Westerbork Synthesis Radio Telescope (WSRT) and ATCA. In fact, when we consider the shadowing limit, the gain over the VLA, ATCA, and WSRT is a factor of 2 (36 versus 18 arcmin).

1.1 The Local Group Dwarf Galaxies

The Local Group (LG) is the group of galaxies gravitationally associated with two massive spiral galaxies, our own Milky Way (MW) and the Andromeda galaxy (M31). Other members of this group include: the third-largest spiral galaxy, M33, a smaller elliptical galaxy, M32, and ~ 100 dwarf galaxies (~ 52 dwarf spheroidals, ~ 28 dwarf irregulars, and ~ 12 transitional dwarf galaxies) (McConnachie, 2012). It is important to note that this is not the precise number of dwarf galaxies in the LG as new dwarf galaxies are still being identified at present. In our Local Universe, dwarf galaxies span a wide range in physical characteristics and occupy a diverse set of environments (e.g., Mateo (1998); Karachentsev et al. (2004)), making them unique astrophysical laboratories necessary for understanding galaxy formation and evolution. The Local Group is divided into three sub-groups (Mateo, 1998). The brightest members of these sub-groups include; the Galaxy and the Magellanic Clouds pair. The Andromeda galaxy and its two elliptical galaxies form the second largest subgroup. The third subgroup consists of a small sub-grouping of mostly dwarf irregular galaxies (Mateo, 1998). A potential fourth sub-group, which consists of NGC 3109, Sextans A, Sextans B and the Antila dwarf is, listed by Mateo (1998). Figure 1.1

Table 1.2: Local Group of Galaxies.

Galaxy name	Other Name	Type	Subgroup	M_V	D_{LG} (kpc)
WLM	DDO 221	IrrIV-V	*LG*	-14.5	925 ± 40
NGC 55		IrrIV	LG	-18.0	1480 ± 150
IC 10	UGC 192	dIrr	M 31	-15.7	825 ± 50
NGC 147	DDO 3	dSph/dE5	M 31	-15.5	725 ± 45
And III		dSph	M 31	-10.3	760 ± 40
NGC 185	UGC 396	dSph/dE3p	M 31	-15.5	620±25
NGC 205	M 110	E5p/dSph-N	M 31	-16.6	815 ± 35
M 32	NGC 221	E2	M 31	-16.7	805 ± 35
M 31	NGC 224	SbI-II	M 31	-21.2	770 ± 25
And I		dSph	M 31	-11.9	805 ± 40
SMC	NGC 292	IrrIV-V	MW	-17.1	58 ± 1.0
Sculptor		dSph	MW	-11.1	79 ± 4
LGS	Pisces	dIrr/dSph	*M*31	-10.5	810 ± 60
IC 1613	DDO 8	IrrV	M 31/LGC	-14.7	700 ±35
And II		dSph	M 31	-11.1	525 ± 110
M 33	NGC 598	ScII-III	M 31	-18.9	445±30
Phoenix		dIrr/dSph	MW/LGC	-10.1	445± 30
Fornax		dSph	MW	-13.3	138±8
EGB 0427+63	UGCA 92	dIrr	M 31	-12.6	1300±700
LMC		dIrrIII-IV	MW	-18.5	49 ± 1.2
carina		dSph	MW	-9.3	101±5
Leo A	DDO 69	dSph	MW/N3109	-11.4	690±100
Sextans B	DDO 70	dIrr	N3109	-14.2	1345 ± 65
NGC 3109	DDO 236	IrrIV-V	N3109	-15.7	1235±65
Antila		dIrr/dSph	N3109	-10.8	1235±65
Leo I	DDO 74	dSph	MW	-11.9	250±30
Sextans A	DDO 75	dIrr	N3109	-14.9	1440±110
Sextans		dSph	MW	-9.5	86±4
Leo II	DDO 93	dSph	MW	-9.6	205±12
GR 8	DDO 155	dIrr	GR 8	-11.6	1590±600
Ursa Minor	DDO 199	dSph	MW	-8.9	66±3
Draco	DDO 208	dSph	MW	-8.8	82±6
Sagittarius		dSph-N	MW	-13.4	24±2
SagDIG	UKS 1927-177	dIrr	LGC	-12.3	1060±160
NGC 6822	DDO 209	IrrIV-V	LGC	-15.2	490± 40
DD0 210	Aquarius	dIrr/dSph	LGC	-10.0	800±250
IC 5151		dIrr	LGC	-14.8	1590±200
Tucana		dSph	LGC	-9.6	880±40
UKS2323-326	UGCA 438	dIrr	LGC	-12.0	1320±350
Pegasus	DDO 216	dIrr/dSph	LGC	-12.9	955±50

Notes. Column 1, Name, Column 2, Hubble type, Column 3, subgroup attribution, Column 4, absolute V-band magnitude and Column 5 distances from the Milky way. Table and information taken from Mateo (1998) and van den Bergh (2000). The acronyms used are MW for the Milky Way subgroup, M31 for the Andromeda subgroup, and LGC for the Local Group Cloud.

shows a scaled 3-D representation of the Local Group and Table 1.2 gives some of the properties of the Local Group galaxies.

The defining distinction between dwarfs and giant galaxies is the global integrated luminosity. Galaxies with an absolute visual magnitudes fainter than V-Band (~ -18 mag) are considered to be dwarfs (McConnachie, 2012). Like the normal galaxies, dwarf galaxies are classified into different types depending on their optical appearance. Early-type dwarfs include dwarf ellipticals (dEs) and dwarf spheroidal (dSphs), while late-type dwarfs include dwarf irregulars (dIrrs) and blue compact dwarfs (BCDs). DSphs are rounder, faint, gas poor, supported mainly by random motions, and are dominated by an old stellar population. Due to their red color and smooth optical isophototes, dSphs appear to be a logical extension of the diffuse dE

galaxy structural family (Sandage & Binggeli, 1984; Ferguson & Binggeli, 1994) but most studies recognize the dSphs as a distinct class of galaxies (Gallagher & Wyse, 1994; Mateo, 1998; Kormendy, 2009). A study of different observed parameters in dwarf galaxies has shown that dSphs are more closely related to dIrrs than to dEs (Kormendy, 1985). DSphs tend to be clustered around the massive hosts such as the Milky Way (MW) and M31 (Dunn, 2010). DEs have a smooth appearance and are elliptical in shape, with the surface brightness largest in the center decreasing uniformly outwards. They host a mixture of stellar populations, and show a complex star formation history (Carraro et al., 2001). In the LG, all known dEs are located around M 31.

DIrrs are typically disky, gas rich, dominated by rotation, exhibit a variety of irregular shapes (Young & Lo, 1997; van Dyk et al., 1998), and are bluer in colour indicating on-going star formation. They are believed to have been formed by gas accretion onto potential wells of small dark matter halos. They tend to be isolated systems and are mostly found in the field or in the outskirts of galaxy clusters and groups. In most cases, the evolution of star formation is roughly constant in dIrr galaxies, although some of them show signatures of a pristine significant peak of star formation (Skillman, 2014). BCDs also known as amorphous dwarfs (based on their optical morphology, e.g., Gallagher & Hunter (1987)) are blue in color, gas-rich, and have low luminosity. These galaxies are known to undergo an intense burst of star formation which may comprise the entire galaxy. Their low metallicity (Izotov & Thuan, 1999) and high gas content (Thuan & Martin, 1981) implies that these systems are relatively young, but the detection of an extended redder stellar host in the vast majority of them has shown that most BCDs are actually older systems (e.g., Loose & Thuan (1986); James (1994); Cairós et al. (2001, 2002)). BCDs share many characteristics with dwarf irregular galaxies, and there is considerable overlap between the categories. One widely accepted definition of BCDs is "dwarf irregular galaxies whose optical presence is exemplified by an active region of star formation" (Sung et al., 2002). IC 10, which was originally known as a dIrr galaxy (Mateo, 1998), is now considered to be a BCD galaxy (Richer et al., 2001), making it the only starburst galaxy in the Local Group. BCDs are usually found in similar environments as dIrrs.

Observations have shown that the evolution of dwarf galaxies can be related on a continuous evolutionary track (Kormendy, 1987). This has been seen from the correlations between the effective surface brightness μ_{eff}, the effective radius R_{eff}, the total magnitude M, and the dark matter content in dEs, dIrrs and dSphs. The existence of the so called *transitional* dwarf galaxies with intermediate properties between the dIrrs and dSphs may serve as an evolutionary link between dIrrs and

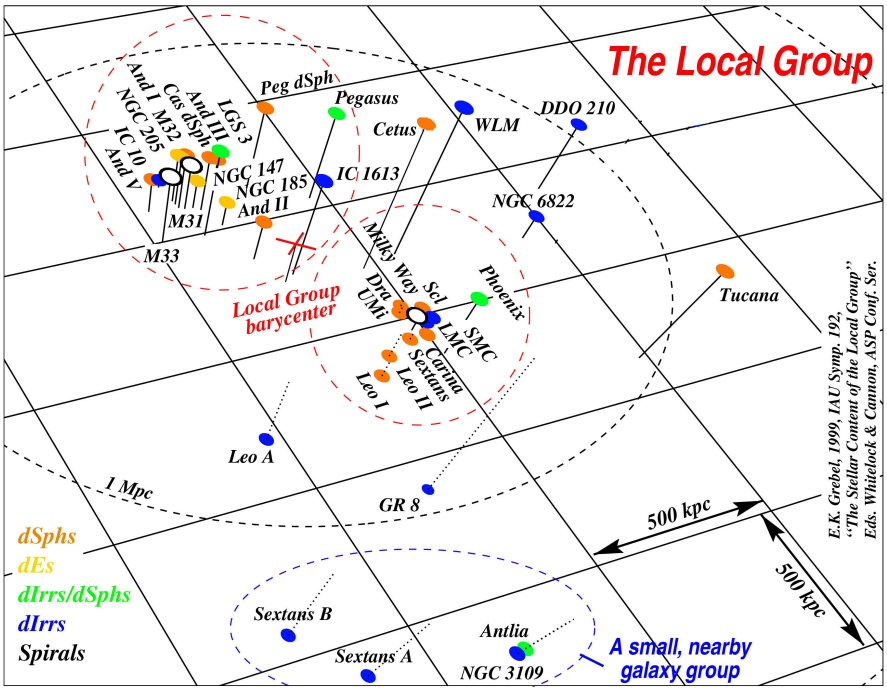

Figure 1.1: shows the 3-D simplified view of the Local Group. A 1 Mpc around the Local Group barycentre lies within the dashed ellipsoid mark. Galaxies above the plane are indicated by solid lines and below with dotted lines. Large spirals are shown in open symbols, dIrrs in blue symbols, dEs in yellow symbols, dSphs are shown in orange symbols, and dSph/dIrr transition types in green symbols (Grebel, 1999)

dSphs (e.g., Grebel et al. (2003)). The evolutionary track of galaxies in general has been explored in great detail using different parameter correlations (e.g., Kormendy (1985, 1987); Kormendy & Bender (2012); Kormendy & Freeman (2016)). Kormendy (1985, 1987) found a clearcut dichotomy between dE and dSph galaxies and was able to make a robust conclusion that dE and dSph galaxies are distinct types of stellar systems with different morphological processes and that dSphs are physically unrelated to dEs. On the other hand, they found a correlation between the continuous parameter sequence defined by dSphs and dIrrs which hints that the two galaxy types are related to each other. Dwarf spheroidals may be late-type galaxies that have lost their gas or processed it all into stars. Figure 1.2 illustrates well the dichotomy between the different types of galaxies.

Several mechanisms may transform a gas-rich into a gas-poor galaxy. A combination of ram pressure, tidal stripping, cosmic UV background radiation, and supernovae explosion is invoked to explain the transformation of a dIrr into a dSph galaxy (Dekel & Silk (1986); Mori et al. (1997); Mac Low & Ferrara (1999); Mori et al. (2002); Kawata et al. (2006)). In recent years, there has been some contro-

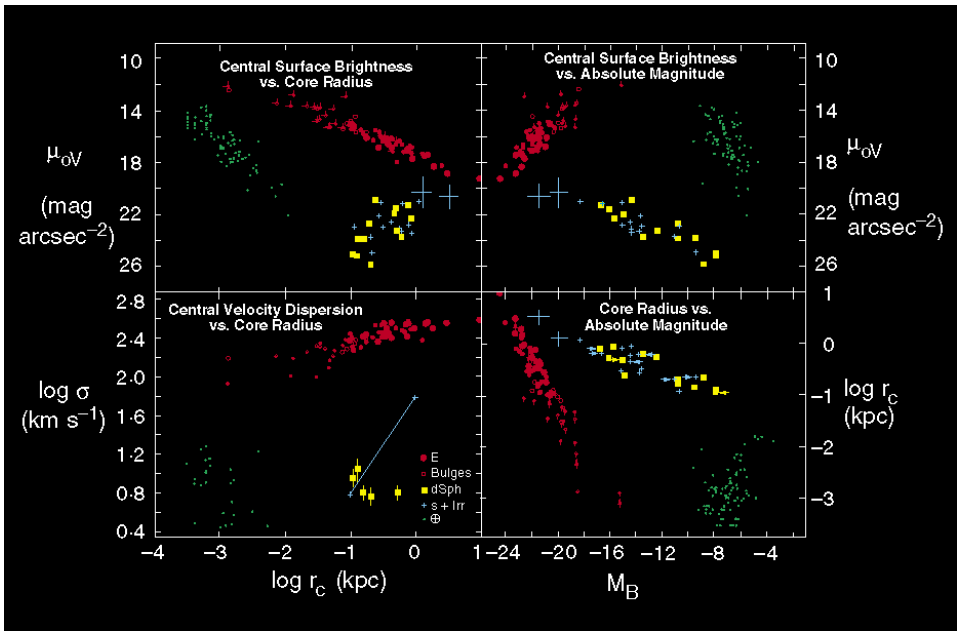

Figure 1.2: Shows the fundamental plane correlation between the seeing-corrected core radius r_c, the central surface brightness μ_{0V}, the central velocity dispersion σ, and the bulge absolute magnitude M_B (H_0 = 50 km s^{-1}/ Mpc) (Kormendy, 1987) of different morphological type galaxies. For all the galaxy types, larger symbols imply better resolution of the core. Elliptical galaxies are shown in filled and open circles, squares represent spheroidals, and dwarf spirals and irregular galaxies are represented by plus signs. Small dots present globular clusters. Two large crosses show the average of 13 and 19 small spiral galaxies from Freeman (1970)

.

versy about the existence of a clear distinction between dSphs and dEs (e.g., Jerjen & Binggeli (1997); Graham & Guzmán (2003); Ferrarese et al. (2006)). One of their argument for the sequences to be merged is that a correlation between the parameters of dSphs and dEs exist, and that the deviation is only seen when bright dEs are taken into account.

1.2 Properties of gas-rich dwarf galaxies

1.2.1 HI distribution and kinematics

In 1945, H.C. van de Hulst predicted that atomic hydrogen (HI) would emit electromagnetic radiation at the frequency of 1420.4 MHz (equivalent to the rest wavelength λ = 21 cm) due to a change in the energy state of the hydrogen atom (specifically, a spin-flip transition). The 21 cm emission line is a powerful tool for studying the HI distribution and kinematics of gas-rich galaxies since it is typically well detected beyond the optical disc and is not affected by dust. HI observations has lead to important discoveries over the years. For example, HI is a great tracer of how

interactions and merging events disrupt or construct galaxies in the Universe. The study of the HI distribution and kinematics of dIrrs have been an area of interest for many years. Early single dish HI observations of gas-rich dwarfs include; e.g., Volders & Högbom (1961); Epstein (1964); Huchtmeier et al. (1981); Huchtmeier (1979); Hunter & Gallagher (1985). These observations were useful for studying the global HI properties of galaxies but lacked the spatial resolution to resolve the galaxies. With the introduction of interferometers in the late sixties such as the Owens Valley Radio Observatory, and later the Westerbrok Synthesis Radio Telescope (WSRT), the Very Large Array (VLA), the Australia Telescope Compact Array (ATCA), and the Giant Metrewave Radio Telescope (GMRT), detailed investigations of the HI distribution and kinematics of selected nearby gas-rich galaxies have been made possible e.g., Skillman & Bothun (1986); Skillman et al. (1987); Shostak & Skillman (1989); Carignan & Beaulieu (1989); Côté & Freeman (1995); Hunter et al. (1998b); Skillman et al. (1987); Gentile et al. (2007); Kreckel et al. (2011). In recent years there has been a very large increase in the available HI data on nearby gas-rich galaxies from different surveys. Some of these surveys include WHISP (Westerbrok HI Survey of Irregular and Spiral Galaxies; van der Hulst et al. (2001)), FIGGS (Faint Irregular Galaxies GMRT Survey; Begum et al. (2008)), THINGS (The HI Nearby Galaxy Survey; Walter et al. (2008)), LITTLE THINGS (Local Irregulars That Trace Luminosity Extremes, The HI Nearby Galaxy Survey; Hunter et al. (2012)), VLA-angst (Very Large Array - survey of ACS Nearby Galaxy Survey Treasury; Ott et al. (2012)), HALOGAS (Hydrogen Accretion in LOcal GAlaxieS; Heald et al. (2011)), and LVHIS (Local Volume HI Survey; Koribalski et al. (2018)). HI blind surveys such as the HIPASS (HI Parkes ALL Sky Survey; Barnes et al. 2001; Meyer et al. 2004) and the ALFALFA (Arecibo Legacy Fast ALFA Survey; Giovanelli et al. (2005); Haynes et al. (2011)) have provided global HI data on dwarf galaxies.

Analyzed data from the surveys and previous observations have shown that the HI distribution in gas-rich dwarfs is often much more extended than the readily apparent optical emission (e.g., Huchtmeier et al. (1981); Meurer et al. (1996); Hunter et al. (2011); Schmidt et al. (2014); Meurer et al. (2018)). Some gas-rich dwarfs show a smooth extended HI disk Hunter et al. (2011), others have an extended choatic HI extended disk Hunter et al. (1998c), while in some cases we see an extended HI disk with starless clumps (Wilcots & Miller, 1998b). Studies of the neutral hydrogen component reveal that the HI distribution in most gas-rich dwarfs is characterized by holes, shells, and bubbles (e.g., Heiles (1979); Puche (1992); Wilcots & Miller (1998); de Blok & Walter (2000); Bagetakos et al. (2009)). It has been suggested that these structures are created by feedback from stellar processes although the premise that stellar winds and SNe are responsible for forming HI holes is still a question of debate (Warren et al., 2011). A study using the WHISP galaxies showed that about

half of the gas-rich dwarfs in their sample have asymmetric HI distribution (Swaters & Balcells, 2002). A large number of dwarf galaxies are accompanied by tails and filaments (Ashley et al., 2014). This suggests ongoing minor mergers and recent arrival of external gas. This has been regarded as a direct evidence of cold gas accretion in the local universe.

The HI kinematics of galaxies are well studied from their HI rotation velocities. The very first extragalactic systems to be mapped in HI and have their kinematics revealed were two late-types dwarfs: the Magellanic Clouds (Kerr & de Vaucouleurs, 1955). These observations clearly showed that the HI clouds were rotating. Subsequent studies revealed that most late-type dwarf galaxies were indeed rotating but with lower velocities than spiral galaxies (V $\sim$ 60 km s^{-1} or lower). These results were later confirmed with the introduction of interferometers because of the increased spatial resolution. The studies by Tully et al. (1978); Broeils (1992); Côté & Freeman (1995), led to the picture that gas-rich dwarf galaxies have low amplitudes, slowly rising rotation curves that keep rising to the last measured point. Dwarf galaxies have HI velocity dispersion between 10 - 15 km s^{-1} in the center which generally decrease in the outskirts of galaxies to $\sim$ 5 - 10 km s^{-1} (Tamburro et al., 2009). Generally, these HI line widths are thought to be due to turbulent velocities rather than thermal and natural broadening.

1.2.2 Star formation thresholds

The evolution of galaxies is strongly influenced by how quickly gas is converted into stars. Part of this thesis aims at understanding which models best describe regions of star formation in dwarf irregular galaxies. Dwarf irregular galaxies are unaffected by the presence of a bulge or spiral arms making them ideal candidates to test various star formation models. The ability of these models to accurately describe star formation properties of galaxies is crucial in understanding what mechanisms drive star formation and what key role the ISM plays in regulating star formation activities. One method of identifying sites of massive star formation in galaxies is to determine the gas densities above which stars can form. This is known as *the star formation threshold*. The existence of a surface density threshold (critical density, Σ_c) for star formation is usually explained using the Toomre (1964) gravitational instability criterion. The threshold density for instability is

$$\Sigma_c = \alpha_Q \frac{\Sigma_g k \sigma}{\pi G} \tag{1.2}$$

where σ is the velocity dispersion, k is the epicyclic frequency, and G is the gravitational constant. Kennicutt (1989) tested the hypothesis and concluded that the Toomre criterion may determine the observed star formation threshold gas densities in active star forming galaxies. This was done by deriving the ratio Σ_c/Σ_g of

gas surface density Σ_g to the critical density Σ_c. From a sample of 15 spiral galaxies and assuming a constant velocity dispersion of 6 km.s^{-1}, Kennicutt (1989) found that star formation was not detected beyond the point where the stability parameter $\alpha_c = \Sigma_g/\Sigma_c$ dropped below 0.63. He then deduced that in regions where $\alpha_Q \geqslant 0.63$, the disk is unstable to axisymmetric disturbances and large scale star formation is observed. Follow up studies with a larger sample consisting of 32 spiral galaxies Martin & Kennicutt (2001) reported an α_Q value of 0.69. Martin & Kennicutt (2001) observed that the simple Toomre criterion breaks down in certain conditions (e.g NGC 2403 and M33) due to limitations for clouds to form in the presence of low shear rates.

In most cases, the Toomre criterion fails to explain the star formation for low surface brightness galaxies (LSB). For LSB galaxies, their gas surface densities are mostly observed to be below the critical densities over most of their disks, and this has been used to explain the low level of star formation activities in these galaxies (van der Hulst et al. (1993); van Zee et al. (1996)). Similar results were later reported from subsequent studies on the star formation threshold of LSB galaxies (Hunter & Plummer (1996); Hunter et al. (1998); Warren et al. (2004); de Blok & Walter (2006)). Motivated by the failure of the Toomre criterion to explain star forming regions in dwarf irregular galaxies, Hunter et al. (1998) suggested an alternative description of the threshold that depends on the ability of a cloud to form in the in the presence of low shear. This criteria is well suited to irregular galaxies because of their slowly rising rotation curve. The threshold is based on the Oort's constant A which describes the shearing motion rather than the epicyclic frequency. The critical density in this case becomes:

$$\Sigma_A = \frac{\alpha_A A \sigma_g}{\pi G} \tag{1.3}$$

and $\alpha_A \sim 2.5$. Hunter et al. (1998) suggested that cloud formation in irregular galaxies may involve more of a competition between self gravity and shear than self gravity and Coriolis forces.

Other criteria such as the importance of the ISM pressure have been used to investigate the star formation threshold in galaxies. The hypothesis that hydrostatic pressure alone determines the ratio of atomic to molecular gas averaged over a particular radius in disk galaxies has been used to investigate the star formation threshold in galaxies. The hypothesis implies that the transition radius, the location where the ratio is unity, should always occur at the same value of stellar surface density in all galaxies (Blitz & Rosolowsky, 2004).

1.2.3 Galaxy dynamics

Baryonic matter, which makes up gas and stars in the galaxies and intergalactic medium, contributes only ~ 5% to the energy-matter density budget of the Universe. The other 95% is split into two components: 25% consists of matter that emits no measurable amount of light (dark matter), while the remaining 70% consists of what is known as dark energy. The first hint for dark matter dates to the mid-1930's following observations of the kinematics of galaxies in the Coma cluster (Zwicky, 1933). Zwicky was able to show that the gravitational mass of a galaxy cluster was much larger than the luminous mass inferred from the observed starlight. The evidence for dark matter, known as the *mass discrepancy* or *missing mass problem* comes from the observed rotation velocities of disk galaxies. Observed velocities stay flat up to large radii, which implies that galaxies should be surrounded by great quantities of non-luminous matter distributed beyond the visible part of galaxies (Rubin et al. (1964); Roberts (1966); Freeman (1970); Bosma (1978)), see Figure 1.3.

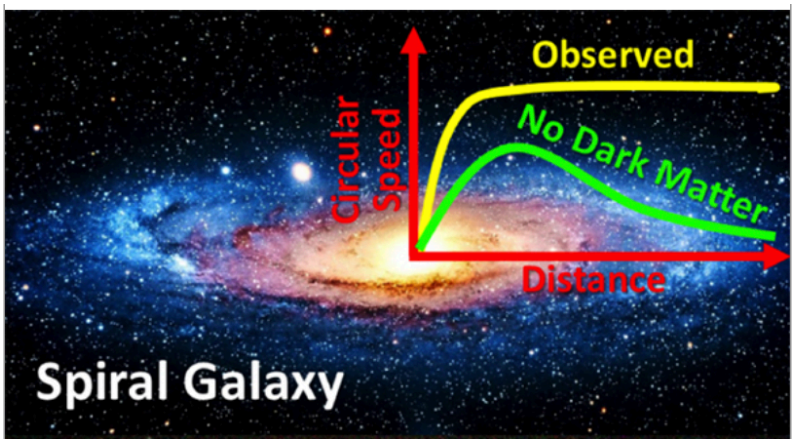

Figure 1.3: Typical observed and expected rotation curves of spiral galaxies. Without dark matter, the velocities should decrease with distance from the galaxy center (green curves). Instead, the dark matter appears to conspire to keep the velocities constant with increasing radius (yellow curve). *Credit: M. Cappellari and the Sloan Digital Sky Survey*

.

The observed velocity curve consists of three main components: the stellar disk (V_*), gaseous disk (V_g), and a spherical dark halo (V_h).

$$V_{rot} = \sqrt{V_g^2 + V_*^2 + V_h^2} \tag{1.4}$$

V_* is usually calculated assuming that stars reside in a disk and using the observed surface brightness profile, scaled by a given value of the stellar mass-to-light ratio (M/L). Similarly, V_g is calculated assuming a thin disk and using the observed atomic hydrogen (HI) surface density profile, scaled by a factor of 1.4 to take into

account the contribution of helium. The dark matter halo is usually described by a theoretical or an empirical density distribution profile. Theoretically, the study of dark matter halos in a hierarchical clustering context is based on a cold matter numerical simulation model known as the Navarro, Frenk, and White model (NFW) (Navarro et al., 1997), where the density distribution of dark matter is given by

$$\rho(r) = \frac{\rho_i}{\frac{r}{r_s}\left(1+\frac{r}{r_s}\right)^2} \tag{1.5}$$

where $\rho_i \sim 3H_0^2/(8\pi G)$ is the critical density for closure of the universe, r_s is the halo scale radius, and H_0 is the Hubble constant. The simulations have consistently predicted the mass density profile that increases towards the center of individual galaxies, being described by $\rho \sim r^{\alpha}$, where α = -1 (Navarro et al. (2010); Ishiyama et al. (2013); Power et al. (2003)), leading to a cusp-like central density. This model works well on large scale structures, but seems to fail on the scales of galaxies (Navarro et al., 1997).

Observations, on the contrary, have shown that most dwarf galaxies and low-surface brightness (LSB) galaxies have a constant dark matter density core, described by the pseudo-isothermal (ISO) dark matter model (Begeman et al., 1991). Here, the density profile of DM is given by

$$\rho(r) = \frac{\rho_o}{\left[1+\left(\frac{r}{r_c}\right)^2\right]} \tag{1.6}$$

where ρ_o is the central density and r_c is the core radius of the halo. The density profile in this case stay more or less flat within the core radius, giving rise to a sizable density core described by $\rho \sim r^{\alpha}$, where $\alpha \sim 0$ (Moore (1994); Blais-Ouellette et al. (1999); de Blok et al. (1996, 2001); Weldrake et al. (2003); Spekkens et al. (2005); Oh et al. (2008, 2011, 2015)). This clear discrepancy between the simulated and observed dark matter distribution in galaxies has become to be known as the *cusp/core* problem.

Different tracers are used to investigate the dark matter distribution of galaxies e.g Hα, CO, and HI. In this thesis, we use HI to trace the total distribution of matter in gas-rich dwarfs. HI is the most extended observable gaseous component, therefore HI rotation curves probe far into the dark halo potentials, making it possible to constrain well the halo parameters and total mass distribution. The rotation curve study of the dwarf galaxy DDO 154 showed that it is dark matter dominated at all radii, including regions well within the optical disk (Carignan & Freeman, 1988). A similar result was reported in subsequent studies based on a few well studied dwarf galaxies (Carignan & Beaulieu (1989); Casertano & van Gorkom (1991);

Broeils (1992); Persic et al. (1996); Côté et al. (2000); Elson et al. (2010); Oh et al. (2015)). These studies have led to the general accepted picture that gas-rich dwarfs are dominated by dark matter at all radii. There are, however, a few exceptional cases such as ESO-325-G11 (Côté et al., 1997). The inner region of this dIrr galaxy is dominated by the stellar component while dark matter dominates in the outer parts.

Although the observational data seem to provide good evidence for the presence of cores in low surface brightness galaxies, possibilities of systematic effects might be present in the data that could give a false impression of cores (de Blok, 2010). Many studies have focused on these effects and asked whether the detected cores could still be consistent with cuspy halo models. The systematic effects include among others pointing problems, non circular motions and beam smearing. Pointing problems can affect the dynamical center. If there are large physical offsets in determining the center, the measured slopes will also be biased downwards. The other effect involves the noncircular motions. The fundamental assumption in the observational analysis is that the gas moves on circular orbits. If for some reason the orbits are elliptical, or if the gas motions are disturbed, this will also lead to an underestimate of the slope. Finally, low resolution data suffer from beam smearing causing the gradients in the velocity fields to become flatter, therefore underestimating the inner rotation velocities.

1.3 This Ph.D. thesis

The work presented in this thesis is essential as it serves as a forerunner for SKA early science: detecting low column density gas in nearby galaxies and understanding the connection between star formation, HI dynamics, and accretion. The main objective of this dissertation is to search for undetected HI disks with the KAT-7 telescope in a sample of gas rich dwarf galaxies selected from the literature. In addition to the KAT-7, we have used a 7 element array of 9 m telescopes from the Dominion Radio Astrophysical Observatory (DRAO). The DRAO telescope, like the KAT-7 telescope, is built with compact baselines suitable for detecting extended HI disks in nearby galaxies. The results obtained from this work will allow us to verify the true HI extent and total flux of the galaxies, important parameters needed in understanding the dynamics of galaxies. The HI distribution, kinematics, and star formation thresholds are also investigated and the results are interpreted in the overall context of the evolution of galaxies. Below is a short overview of the literature concerning the observed dwarf galaxies that is relevant to the work presented here:

- **NGC 6822:** located at a distance of 480 ± 20 kpc (Feast et al., 2012), NGC 6822 (DDO 209) is one of the closest gas rich dwarfs in the Local Group. Due to its distance, the galaxy tends to appear very extended on the sky. The HI properties of this galaxy have been well studied with ATCA (e.g., de Blok & Walter (2000); Weldrake et al. (2003)). With its HI diameter of 1 degree (de Blok & Walter, 2000), NGC 6822 is a perfect target for KAT-7 and falls exactly in its "niche": detecting large scale structures not visible to other synthesis arrays such as the VLA and ATCA. It is also a perfect test case for mosaicking extended structures that are close to filling the primary beam of KAT-7. Its inclination, gas richness, and proximity also make it an ideal candidate for studying its rotation curve and dark matter content.

- **Sextans A:** Sextans A (DDO 75) is a gas rich dwarf galaxy located at a distance of 1.3 Mpc (de Vaucouleurs et al., 1991a). Although the HI of Sextans A has been well studied (Huchtmeier et al. (1981); Skillman et al. (1988); Wilcots & Hunter (2002); Hunter et al. (2011)), its true HI extent remains uncertain. Huchtmeier et al. (1981) first reported an HI extent of $54'$. Follow up studies reported an HI diameter of $9.4'$ from the VLA observations (Skillman et al., 1988), $18'$ from the VLA mosaic observations (Wilcots & Hunter, 2002), and $22.1'$ from the GBT observations. In order to verify the true HI extent of Sextans A, we carried out high sensitivity intermediate spatial resolution HI observations with KAT-7. The KAT-7 is best suited for this study because its unique capabilities are able to detect, if present, the large HI extent reported by Huchtmeier et al. (1981). In addition to this, unlike the GBT and Effelsberg observations, KAT-7 is able to resolve Sextans A, which allows us to explore the kinematics of the extended HI disk.

- **Sextans B:** Sextans B (DD0 70) is a dwarf irregular galaxy at a distance of 1.3 Mpc (de Vaucouleurs et al., 1991a). The HI distribution of Sextans B was first reported by Huchtmeier et al. (1981). The HI kinematics have been studied by Worth & Wilcots (2009) and Oh et al. (2015) using data from the VLA. Apart from searching for the presence of an extended HI disk of Sextans B, it is interesting to explore detailed HI properties of Sextans A and B simultaneously as they are considered to be twin galaxies.

- **IC 10:** IC 10 (UGC 192) is the only known BCD galaxy in the Local Group. It is located at a distance of 0.7 Mpc (Hunter et al., 2012). The HI of IC 10 is well studied (Huchtmeier (1979); Shostak & Skillman (1989); Wilcots & Miller (1998); Nidever et al. (2013); Ashley et al. (2014)). It is still unclear what mechanisms are responsible for the complex chaotic HI disk of IC 10. One possible clue could be a new faint HI emission feature near IC 10 reported for the first time in the GBT observations (Nidever et al., 2013). However, this feature is

not observed in the Effelsberg 21 cm survey (EBHIS) data. While the Effelsberg data is some 3 times less sensitive than the targeted GBT observations we compare it to, it is a similar class telescope to the GBT. Thus, its failure to detect it begs the question whether the observed feature is "real" or is an artifact of GBT data. To verify the existence of this feature, we have carried out high sensitivity HI observations of IC 10 with DRAO. If this feature is real it will provide the first such evidence for explaining the very disturbed and highly extended HI disk and disk of IC 10 (through possible interaction, including tidal stripping and merging).

1.3.1 Thesis outline

The structure of this Ph.D. thesis is as follows: Chapter 2 presents the HI study of the Local Group dwarf irregular galaxy NGC 6822 with the KAT-7 telescope. We have derived the HI distribution, kinematics, and star formation thresholds. We compare the KAT-7 results with results obtained from the ATCA observations. In Chapter 3, we present HI observations of the Local Group dwarf irregular galaxies Sextans A and B with the KAT-7 array. The results from this chapter include the HI distribution, kinematics, and star formation thresholds of Sextans A and B. The KAT-7 results are compared with the results obtained from the LITTLE THINGS Survey with the VLA. In Chapter 4 we present HI observations of the Blue Compact Dwarf (BCD) galaxy IC 10 with the DRAO synthesis telescope. Finally, in Chapter 5, we present the conclusion and future work.

Ashley T., Elmegreen B. G., Johnson M., Nidever D. L., Simpson C. E., Pokhrel N. R., 2014, AJ, 148, 130

Bagetakos I., Brinks E., Walter F., de Blok W. J. G., Rich J. W., Usero A., Kennicutt Jr. R. C., 2009, in The Evolving ISM in the Milky Way and Nearby Galaxies. p. 17

Barnes D. G., et al., 2001, MNRAS, 322, 486

Begeman K. G., Broeils A. H., Sanders R. H., 1991, MNRAS, 249, 523

Begum A., Chengalur J. N., Karachentsev I. D., Sharina M. E., Kaisin S. S., 2008, MNRAS, 386, 1667

Blais-Ouellette S., Carignan C., Amram P., Côté S., 1999, AJ, 118, 2123

Blitz L., Rosolowsky E., 2004, ApJ, 612, L29

Bosma A., 1978, PhD thesis, PhD Thesis, Groningen Univ., (1978)

Broeils A. H., 1992, PhD thesis, PhD thesis, Univ. Groningen, (1992)

Cairós L. M., Caon N., Vílchez J. M., González-Pérez J. N., Muñoz-Tuñón C., 2001, ApJS, 136, 393

Cairós L. M., Caon N., García-Lorenzo B., Vílchez J. M., Muñoz-Tuñón C., 2002, ApJ, 577, 164

Carignan C., Beaulieu S., 1989, ApJ, 347, 760

Carignan C., Freeman K. C., 1988, ApJ, 332, L33

Carignan C., Purton C., 1998, ApJ, 506, 125

Carignan C., Frank B. S., Hess K. M., Lucero D. M., Randriamampandry T. H., Goedhart S., Passmoor S. S., 2013, AJ, 146, 48

Carraro G., Chiosi C., Girardi L., Lia C., 2001, MNRAS, 327, 69

Casertano S., van Gorkom J. H., 1991, AJ, 101, 1231

Côté S., Freeman K., 1995, in Richter O.-G., Borne K., eds, Astronomical Society of the Pacific Conference Series Vol. 70, Groups of Galaxies. p. 75

Côté S., Freeman K. C., Carignan C., 1997, in Persic M., Salucci P., eds, Astronomical Society of the Pacific Conference Series Vol. 117, Dark and Visible Matter in Galaxies and Cosmological Implications. p. 52 (arXiv:astro-ph/9704031)

Côté S., Carignan C., Freeman K. C., 2000, AJ, 120, 3027

Dekel A., Silk J., 1986, ApJ, 303, 39

Dunn J. M., 2010, MNRAS, 408, 392

Elson E. C., de Blok W. J. G., Kraan-Korteweg R. C., 2010, MNRAS, 404, 2061

Epstein E. E., 1964, AJ, 69, 490

Feast M. W., Whitelock P. A., Menzies J. W., Matsunaga N., 2012, MNRAS, 421, 2998

Ferguson H. C., Binggeli B., 1994, A&A Rev., 6, 67

Ferrarese L., et al., 2006, ApJS, 164, 334

Foley A. R., et al., 2016, MNRAS, 460, 1664

Freeman K. C., 1970, ApJ, 160, 811

Gallagher III J. S., Hunter D. A., 1987, AJ, 94, 43

Gallagher III J. S., Wyse R. F. G., 1994, PASP, 106, 1225

Gentile G., Salucci P., Klein U., Granato G. L., 2007, MNRAS, 375, 199

Giovanelli R., et al., 2005, AJ, 130, 2598

Graham A. W., Guzmán R., 2003, AJ, 125, 2936

Grebel E. K., 1999, in Whitelock P., Cannon R., eds, IAU Symposium Vol. 192, The Stellar Content of Local Group Galaxies. p. 17 (arXiv:astro-ph/9812443)

Grebel E. K., Gallagher III J. S., Harbeck D., 2003, AJ, 125, 1926

Haynes M. P., et al., 2011, AJ, 142, 170

Heald G., et al., 2011, A&A, 526, A118

Heiles C., 1979, PASP, 91, 611

Huchtmeier W. K., 1979, A&A, 75, 170

Huchtmeier W. K., Seiradakis J. H., Materne J., 1981, A&A, 102, 134

Hunter D. A., Gallagher III J. S., 1985, AJ, 90, 1789

Hunter D. A., Plummer J. D., 1996, ApJ, 462, 732

Hunter D. A., Elmegreen B. G., Baker A. L., 1998a, ApJ, 493, 595

Hunter D. A., Wilcots E. M., van Woerden H., Gallagher J. S., Kohle S., 1998b, ApJ, 495, L47

Hunter D. A., Wilcots E. M., van Woerden H., Gallagher J. S., Kohle S., 1998c, The Astrophysical Journal Letters, 495, L47

Hunter D. A., Zahedy F., Bowsher E. C., Wilcots E. M., Kepley A. A., Gaal V., 2011, AJ, 142, 173

Hunter D. A., et al., 2012, AJ, 144, 134

Ishiyama T., et al., 2013, ApJ, 767, 146

Izotov Y. I., Thuan T. X., 1999, ApJ, 511, 639

James P. A., 1994, MNRAS, 269, 176

Jerjen H., Binggeli B., 1997, in Arnaboldi M., Da Costa G. S., Saha P., eds, Astronomical Society of the Pacific Conference Series Vol. 116, The Nature of Elliptical Galaxies; 2nd Stromlo Symposium. p. 239 (arXiv:astro-ph/9701221)

Karachentsev I. D., Karachentseva V. E., Huchtmeier W. K., Makarov D. I., 2004, AJ, 127, 2031

Kawata D., Arimoto N., Cen R., Gibson B. K., 2006, ApJ, 641, 785

Kennicutt Jr. R. C., 1989, ApJ, 344, 685

Kerr F. J., de Vaucouleurs G., 1955, Australian Journal of Physics, 8, 508

Koribalski B. S., et al., 2018, MNRAS, 478, 1611

Kormendy J., 1985, ApJ, 295, 73

Kormendy J., 1987, in de Zeeuw P. T., ed., IAU Symposium Vol. 127, Structure and Dynamics of Elliptical Galaxies. pp 17–34

Kormendy J., 2009, in Jogee S., Marinova I., Hao L., Blanc G. A., eds, ApJ 419,87

Kormendy J., Bender R., 2012, ApJ 198, 2

Kormendy J., Freeman K. C., 2016, AJ 817, 84

Kreckel K., Peebles P. J. E., van Gorkom J. H., van de Weygaert R., van der Hulst J. M., 2011, AJ, 141, 204

Loose H.-H., Thuan T. X., 1986, in Kunth D., Thuan T. X., Tran Thanh Van J., Lequeux J., Audouze J., eds, Star-forming Dwarf Galaxies and Related Objects. pp 73–88

Lucero D. M., Carignan C., Elson E. C., Randriamampandry T. H., Jarrett T. H., Oosterloo T. A., Heald G. H., 2015, MNRAS, 450, 3935

Mac Low M.-M., Ferrara A., 1999, ApJ, 513, 142

Martin C. L., Kennicutt Jr. R. C., 2001, ApJ, 555, 301

Mateo M. L., 1998, ARA&A, 36, 435

McConnachie A. W., 2012, AJ, 144, 4

Meurer G. R., Carignan C., Beaulieu S. F., Freeman K. C., 1996, AJ, 111, 1551

Meurer G. R., Obreschkow D., Wong O. I., Zheng Z., Audcent-Ross F. M., Hanish D. J., 2018, MNRAS, 476, 1624

Meyer M. J., et al., 2004, MNRAS, 350, 1195

Moore B., 1994, Nature, 370, 629

Mori M., Yoshii Y., Tsujimoto T., Nomoto K., 1997, ApJ, 478, L21

Mori M., Ferrara A., Madau P., 2002, ApJ, 571, 40

Navarro J. F., Frenk C. S., White S. D. M., 1995, MNRAS, 275, 56

Navarro J. F., Frenk C. S., White S. D. M., 1997, ApJ, 490, 493

Navarro J. F., et al., 2010, MNRAS, 402, 21

Nidever D. L., et al., 2013, ApJ, 779, L15

Oh S.-H., de Blok W. J. G., Walter F., Brinks E., Kennicutt Jr. R. C., 2008, AJ, 136, 2761

Oh S.-H., de Blok W. J. G., Brinks E., Walter F., Kennicutt Jr. R. C., 2011, AJ, 141, 193

Oh S.-H., et al., 2015, AJ, 149, 180

Ott J., et al., 2012, AJ, 144, 123

Persic M., Salucci P., Stel F., 1996, MNRAS, 281, 27

Pisano D. J., 2014, AJ, 147, 48

Power C., Navarro J. F., Jenkins A., Frenk C. S., White S. D. M., Springel V., Stadel J., Quinn T., 2003, MNRAS, 338, 14

Puche D., 1992, in American Astronomical Society Meeting Abstracts. p. 1201

Richer M. G., et al., 2001, A&A, 370, 34

Roberts M. S., 1966, ApJ, 144, 639

Rubin V. C., Burbidge E. M., Burbidge G. R., Prendergast K. H., 1964, ApJ, 140, 80

Sandage A., Binggeli B., 1984, AJ, 89, 919

Schmidt P., Józsa G. I. G., Gentile G., Oh S.-H., Schuberth Y., Ben Bekhti N., Winkel B., Klein U., 2014, A&A, 561, A28

Shostak G. S., Skillman E. D., 1989, A&A, 214, 33

Skillman E., 2014, Is the First Epoch of Star Formation in Satellite Galaxies Universal? - Part II, HST Proposal

Skillman E. D., Bothun G. D., 1986, A&A, 165, 45

Skillman E. D., Bothun G. D., Murray M. A., Warmels R. H., 1987, A&A, 185, 61

Skillman E. D., Terlevich R., Teuben P. J., van Woerden H., 1988, A&A, 198, 33

Spekkens K., Giovanelli R., Haynes M. P., 2005, AJ, 129, 2119

Stanimirovic S., 2002, in Stanimirovic S., Altschuler D., Goldsmith P., Salter C., eds, Astronomical Society of the Pacific Conference Series Vol. 278, Single-Dish Radio Astronomy: Techniques and Applications. pp 375–396 (arXiv:astro-ph/0205329)

Sung E.-C., Chun M.-S., Freeman K. C., Chaboyer B., 2002, in Da Costa G. S., Sadler E. M., Jerjen H., eds, Astronomical Society of the Pacific Conference Series Vol. 273, The Dynamics, Structure History of Galaxies: A Workshop in Honour of Professor Ken Freeman. p. 341

Swaters R. A., Balcells M., 2002, A&A, 390, 863

Tamburro D., Rix H.-W., Leroy A. K., Mac Low M.-M., Walter F., Kennicutt R. C., Brinks E., de Blok W. J. G., 2009, AJ, 137, 4424

Thuan T. X., Martin G. E., 1981, ApJ, 247, 823

Toomre A., 1964, ApJ, 139, 1217

Tully R. B., Bottinelli L., Fisher J. R., Gougenheim L., Sancisi R., van Woerden H., 1978, A&A, 63, 37

Volders L. M. J. S., Högbom J. A., 1961, Bull. Astron. Inst. Netherlands, 15, 307

Walter F., Brinks E., de Blok W. J. G., Bigiel F., Kennicutt Jr. R. C., Thornley M. D., Leroy A., 2008, AJ, 136, 2563

Warren B. E., Jerjen H., Koribalski B. S., 2004, AJ 128, 1152

Warren S. R., et al., 2011, ApJ, 738, 10

Weldrake D. T. F., de Blok W. J. G., Walter F., 2003, MNRAS, 340, 12

Wilcots E. M., Hunter D. A., 2002, AJ, 123, 1476

Wilcots E. M., Miller B. W., 1998a, AJ, 116, 2363

Wilcots E. M., Miller B. W., 1998b, AJ 116, 2363

Worth R., Wilcots E. M., 2009, in American Astronomical Society Meeting Abstracts #213. p. 251

Young L. M., Lo K. Y., 1997, ApJ, 490, 710

Zwicky F., 1933, Helvetica Physica Acta, 6, 110

de Blok W. J. G., 2010, Advances in Astronomy, 2010, 789293

de Blok W. J. G., Walter F., 2000, ApJ, 537, L95

de Blok W. J. G., Walter F., 2006, AJ, 131, 363

de Blok W. J. G., McGaugh S. S., van der Hulst J. M., 1996, MNRAS, 283, 18

de Blok W. J. G., McGaugh S. S., Bosma A., Rubin V. C., 2001, ApJ, 552, L23

de Vaucouleurs G., de Vaucouleurs A., Corwin Jr. H. G., Buta R. J., Paturel G., Fouqué P., 1991, Third Reference Catalogue of Bright Galaxies. Volume I: Explanations and references

van Dyk S. D., Puche D., Wong T., 1998, AJ, 116, 2341

van Zee L., Haynes M. P., Salzer J. J., Broeils A. H., 1996, AJ, 112, 129

van den Bergh S., 2000, PASP, 112, 529

van der Hulst J. M., Skillman E. D., Smith T. R., Bothun G. D., McGaugh S. S., de Blok W. J. G., 1993, AJ, 106, 548

van der Hulst J. M., van Albada T. S., Sancisi R., 2001, in Hibbard J. E., Rupen M., van Gorkom J. H., eds, Astronomical Society of the Pacific Conference Series Vol. 240, Gas and Galaxy Evolution. p. 451

CHAPTER 2

HI KINEMATICS, MASS DISTRIBUTION, AND STAR FORMATION THRESHOLD IN NGC 6822, USING THE SKA PATHFINDER KAT-7

We present high sensitivity HI observations of NGC 6822, obtained with the Karoo Array Telescope (KAT-7). We study the kinematics, the mass distribution, and the star formation thresholds. The KAT-7 short baselines and low system temperature make it sensitive to large-scale, low surface brightness emission. The observations detected ~ 23% more flux than previous Australian Telescope Compact Array (ATCA) observations. We fit a tilted ring model to the HI velocity field to derive the rotation curve (RC). The KAT-7 observations allow the measurement of the rotation curve of NGC 6822 out to 5.8 kpc, ~ 1 kpc further than existing measurements. NGC 6822 is seen to be dark matter dominated at all radii. The observationally motivated pseudo-isothermal dark matter (DM) halo model reproduces well the observed RC while the Navarro Frank-White DM model gives a poor fit to the data. We find the best fit mass to light ratio (M/L) of 0.12 ± 0.01 which is consistent with the literature. The assumption of Modified Newtonian Dynamics (MOND) gives a poor fit to our data. We derive the star formation threshold in NGC 6822 using the HI and Hα data. The critical gas densities were calculated for gravitational instabilities using the Toomre-Q criterion and the cloud-growth criterion. We found that in regions of star formation, the cloud-growth criterion explains star formation better than the Toomre-Q criterion. This shows that the local shear rate could be a key player in cloud formation for irregular galaxies such as NGC 6822.

2.1 Introduction

Dwarf irregular (dIrr) galaxies constitute a considerable fraction of all galaxies and are prevalent among the star-forming systems. Their simplicity, free from spiral density waves, makes them excellent laboratories in which we can study the stellar and gas content. The most extensively studied of these dIrr galaxies are in the Local Group, as their proximity red provides us detailed information of their HI disks. DIrr galaxies often show HI envelopes that extend significantly outwards beyond the stellar disks [e.g., Huchtmeier et al., 1981; Wilcots & Miller, 1998; Gentile et al., 2007; Kreckel et al., 2011; Schmidt et al., 2014]. These extended structures provide crucial information on the formation and evolution of the galaxies, and allow the gas dynamics of these systems to be traced at large distances from the centers [e.g., Carignan & Beaulieu, 1989; Carignan & Purton, 1998], therefore probing their dark matter halos over a wide radial range.

The evolution of galaxies is strongly influenced by how quickly gas is consumed by stars. Despite being gas-rich, the dIrr galaxies show very little star formation as compared to spiral galaxies. This has been one of the early puzzles about these galaxies. The reason for this is not well-understood but it could indicate inefficient star formation or that the gas density is below the threshold value. The existence of surface density thresholds for star formation is explained in terms of the Toomre Q criterion for gravitational instability which describes the gravitational instabilities in a gaseous, rotating disk (Quirk, 1972). Kennicutt (1989) and Martin & Kennicutt (2001) explained the gravitational instabilities using the azimuthally averaged CO/HI and Hα profiles, thereby providing a global picture of the threshold. Bigiel et al. (2008) used a sample of spiral and dwarf galaxies to investigate how star formation laws differ between molecular gas (H_2) centers of spiral galaxies, their HI dominated outskirts and the HI rich late-type dwarf galaxies. They found a good correlation between star formation rate density and the molecular hydrogen surface density. These results suggest that molecular gas forms stars at a constant efficiency in spirals. They found that the relationship between HI and star formation rate in spiral galaxies varies dramatically as a function of radius while the star formation efficiency in dwarf galaxies showed a similar trend to that found in the outer parts of spiral galaxies. They concluded that rotational shear, which is typically absent in dwarf galaxies cannot drive star formation efficiencies. In certain galaxies, star forming regions have been found in regions with gas densities below the threshold value. Hα imaging of three nearby galaxies (Ferguson et al., 1998) revealed the presence of HII regions out to, and beyond the optical radii, R_{25}. More recently, studies showing the bright stellar complexes in the extreme outer disk of M83, extending to about 4 times the radius at which the majority of HII regions are detected suggests that Hα may not be a complete tracer of ongoing star formation in disk galaxies

(Thilker et al., 2005).

Several studies of irregular galaxies tracing the extent and dynamics of the HI gas are mostly available from observations performed with arrays having higher resolution and which lack short baselines. [e.g., Skillman & Bothun, 1986; Côté et al., 2000; de Blok & Walter, 2000; Kreckel et al., 2011; Hunter et al., 2012]. This means that we could be missing out on the low surface brightness extended HI in these galaxies, therefore underestimating their HI extent. To address this problem, we would ideally want to use a single dish telescope as this does not resolve out any emission, however, these dishes do not have the required spatial resolution. Our best alternative is to use an interferometer with short baselines optimized for detecting low column density regions.

NGC 6822 is one of the most intriguing dwarf galaxies in the Local Group. It is located at a distance of 480 ± 20 kpc (Feast et al., 2012), making it one of the closest dIrr in the Local Group after the Magellanic Cloud (SMC & LMC). It does not appear to be associated with either the Milky Way or M31, and it has no other neighboring companion. NGC 6822 is faint, with an absolute magnitude of M_B = -15.2 (Mateo, 1998). The basic parameters of NGC 6822 are given in Table 2.1. The HI disc of this galaxy was first studied by Volders & Högbom (1961), using observations performed with the single dish Dwingeloo telescope. Their results show a disk-like system, with large amounts of HI ($1.5 \times 10^8 M_\odot$) rotating in an orderly pattern about the center field. The first interferometry study was done by Gottesman & Weliachew (1977) who used observations from the Owens Valley Radio Observatory interferometer to study the neutral hydrogen associated with the optical core of the galaxy. Their results already showed highly structured ISM. Brandenburg & Skillman (1998) used the VLA to study the HI distribution and kinematics in NGC 6822. Their HI images revealed a complex and clumpy interstellar medium with shell structures found over a large range of size scales. de Blok & Walter (2000) used the low and high resolution observations from the Parkes single dish and the Australian Telescope Compact Array (ATCA) to derive the HI kinematics and dynamics in NGC 6822. Their results show that NGC 6822 is not a quiescent non-interacting dwarf galaxy, but that it is undergoing an interaction with a possible companion. The RC obtained from the high resolution data showed that NGC 6822 is dark matter dominated (Weldrake et al., 2003).

The proximity, isolation and lack of spiral arm structures of NGC 6822 makes it an excellent candidate to investigate star formation triggers other than spiral density waves. de Blok & Walter (2006) used the high resolution, wide field, deep HI, Hα and optical data to derive the star formation thresholds in NGC 6822. Their studies revealed that the interpretation of the star formation threshold depends on

Table 2.1: Basic properties of NGC 6822.

Parameter		Ref
Morphological Type	IB(s)m	(a)
Right ascension (J2000)	19:44:57.9	(a)
Declination (J2000)	-14:48:11.0	(a)
Distance (kpc)	480± 20	(g)
Isophotal major diameter, D_{25} (kpc)	2.7	(c)
Central surface brightness, $B(0)_c$ (mag/arcsec^2)	19.8	(d)
Scale length, α^{-1}(arcmin)	4.7	(d)
Metallicity($Z_\odot$)	0.3	(e)
Total optical luminosity(L_V)($L_\odot$)	~ 9.4×10^7	(b)
$V_{heliocentric}$ (km s^{-1})	-55	(f)
PA_opt(◦)	10± 5	(b)
Inclination_opt(◦)	67± 3	(b)
Total HI mass ($M_\odot$)	1.34×10^8	(f)
Dynamical mass ($M_\odot$)	3.2×10^9	(f)

Notes. Ref (a) de Vaucouleurs (1991); (b) Mateo (1998); (c) de Blok & Walter (2000); (d) Weldrake et al. (2003); (e) Skillman et al. (1989); (f) de Blok & Walter (2006); (g) Feast et al. (2012)

the velocity dispersion used. They showed that when the velocity dispersion of 6 km s^{-1} is used, the value which is consistent with previous works and the value derived from the moment analysis, the disk is stable against star formation everywhere. In this case, the star formation is attributed to the local density enhancements which would be averaged out in the radial profile, giving the impression of a stable disk. Their results show that using the velocity dispersion of the cool component (~4 km s^{-1}) fits the distribution of the current star formation in NGC 6822. In this case, they suggested that star formation is self regulatory.

We present HI observations of NGC 6822 taken with the Karoo Array Telescope (KAT-7). With the HI diameter of > 1 degree (de Blok & Walter, 2000), NGC 6822 is a perfect target to be observed with the KAT-7 and falls in its "niche": detecting low column density large scale structures not visible to other synthesis arrays such as the VLA and ATCA. The purpose of these observations is to study the distribution and kinematics of the neutral gas and the dynamics of the galaxy. Furthermore, we aim to understand the nature of dark matter associated with this galaxy at much larger radii and derive the star formation thresholds. The remainder of this paper is as follows. KAT-7 HI observations and data reduction are summarized in Section 2.2, while the HI results appear in Section 2.3. Section 2.4 details the derivation of the rotation curve that is used for the mass model analysis of Section 2.5. In Section 2.6, we explore instability models for the onset of star formation in NGC 6822 and in Section 2.7 we summarize our work.

2.2 KAT-7 observations and data reduction

A mosaic of three pointings was observed for NGC 6822 in the 21cm line with the seven dish KAT-7 array, a MeerKAT engineering test bed (Carignan et al., 2013). The array is compact with baselines ranging from 26 to 186 m. The compact base-

lines and the low receiver temperature ($T_{sys} \simeq 26$K) (Foley et al., 2016) of KAT-7 allow us to detect low surface brightness extended emission (Lucero et al., 2015; Hess et al., 2017). The observations were done between August and December 2014. The observations were done in 20, 5-8 hr segments for the total integration time of $\sim$ 151 hrs, including calibration. 17 sessions were observed using a full 7 antenna array while 3 sessions were observed with 5 or 6 antennas depending on the availability of antennas present. The observation parameters are listed in Table 2.2. The c16n13M4K correlator mode set up was used, that is we measured two linear polarizations in 4096 channels over a bandwidth of 12.5 MHz allowing for the spectral resolution of 0.64 km s^{-1}, centered at 1420.7 MHz.

The calibration steps followed the standard techniques of the CASA software package version 4.3.0 (McMullin et al., 2007). PKS 1934-638 and PKS 1938-155 were used as the bandpass/flux and phase calibrators respectively. We observed the bandpass/flux calibrator at the beginning and end of each observation run while the phase calibrator was observe in between each target scans. Data were loaded into CASA and inspected for antenna failures and Radio Frequency Interference (RFI) using the CASA task VIEWER. An automated flagging was used to discard data resulting from shadowing and low elevation $\leqslant$ 20 deg. 10 % of the channels on both sides of the band were flagged out to get rid of the bandpass roll off. We flagged out the entire antenna 7 on 4 observing runs due to severely bad data caused by a warm cryo. Flagging out antenna 7 from these observations meant that we lost out on most of the long baseline observations. This resulted in 13 observing runs having data with all the 7 antennas present during observations and not 17 as initially stated before flagging. The data was averaged by 4 channels giving the velocity resolution of 2.56 km s^{-1}. We then proceeded with the absolute flux calibration as well as the bandpass and gain calibration. The quality of the calibration solutions were first checked by inspecting the phase and amplitude calibration tables, and applying the solutions to the primary and secondary calibrators respectively. The corrected visibilities were examined in terms of amplitude and phase as a function of time and frequency as well as amplitude and phase as a function of uv distance for both calibrators. The examined calibration solutions were then applied to the target source for each observing run.

The calibrated target visibilities for the three mosaic pointings were separated from the calibrator sources and different observing runs were then combined together using the CASA task CONCAT. To ensure the angular resolution of our observation was not compromised due to the missing long baseline antennas on some of the observing runs, we decided to create two separate files. The first file was created by combining 13 observing files, each having all the 7 antennas present during observation and after flagging while the second file was created by combining all the 20

observing sessions. The task CVEL was then used to produce data files with proper velocity coordinates by correcting for doppler shifts. Detailed use of CVEL on KAT-7 data has been described in Carignan et al. (2013). Heliocentric velocities from -800 to -200 and 200 to 600 km s^{-1} were chosen as representative of the continuum and the task UVCONTSUB was used to subtract the continuum from the spectral data. This was carefully done by taking note of the Galactic HI contamination.

2.2.1 Imaging

Imaging was done using the task CLEAN by selecting the mosaic and multi-scale clean option. Multi-scale clean allows us to retain the extended low level emission by modeling the sky brightness as the summation of components of emission having different size scales. A dirty channel map was produced for each data set produced from the CONCAT task to compare the resolution and sensitivity. Inspecting the two maps showed that we do not lose resolution by combining observations runs with missing long baseline antennas, however there was no significant change in the signal to noise between the images produced by the two data sets. Considering the data volume and processing time, we decided to work with the data set produced by combining observations from runs with all 7 antennas present during observations and after flagging.

A mask was first created by using the interactive clean option and selecting regions of galaxy emission manually. The rms was then established by measuring the average noise in four line free channels. The final cube was imaged in a non interactive mode using the mask created and cleaning down to a 1.5σ level. A 1.5σ level were selected after investigating different flux cutoffs. Thresholds less than a 1.5σ level showed artifacts of over cleaning while thresholds greater than a 1.5σ level were not sufficient as we were unable to retain all the galaxy flux. Three final cubes were produced by applying the natural (na), uniform (un), and the neutral (robust=0) weighting to the data. We decided to work with the robust=0 cube after comparing the sensitivity and the resolutions obtained from the three weighting options. With our angular resolution (synthesized beam) of $\sim 3.5'$, the cubes were imaged using the pixel size of $30''$ by $30''$ to ensure a well resolved central lobe ($\sim$ 7 pixels per beam).

We noticed the presence of horizontal stripes in the image plane of all our cubes. These artifacts have been attributed to the presence of radio frequency interference (RFI) generated internally around $|u| \leqslant 25\ \lambda$ (Carignan et al., 2016; Hess et al., 2015). We created three cubes to test the cutoff limits for the artifacts in the cube. The first cube was produced after flagging out visibilities with $|u| \leqslant 10\lambda$, the second cube was produced after flagging out visibilities with $|u| \leqslant 15\lambda$ and lastly the third

cube was produced after flagging out visibilities with $|u| \leqslant 25\lambda$. The artifacts were seen to disappear in all the three cubes. This allowed us to select the cube created by flagging data ($|u| \leqslant 10\lambda$), the advantage being that a smaller percentage of data was flagged in this case enabling us to preserve the much needed short spacing data. We uncovered further artifacts in form of lines parallel to the major axis of NGC 6822. These artifacts were removed by getting rid of the affected baseline between antennas 4 and 5 for all observations. After getting rid of these artifacts, the noise level in the cube reduced by a factor of ~ 2 allowing us to reach the expected theoretical noise in line free channels.

Given the radial velocity of NGC 6822, the HI data cube is heavily affected by foreground Galactic emission in the range -18 km s^{-1} to 24 km s^{-1}. The Galactic emission between the velocity range 8 km s^{-1} to 24 km s^{-1} was easily removed because it did not contaminate the NGC 6822 emission. However, Galactic emission between -18 km s^{-1} to 7 km s^{-1} is much closer to the galaxy's emission and was blanked using the following criteria: in all channels affected by Galactic emission, we isolated emission 3 times the rms noise in line free channels (3σ, where σ = 3.7 mJy/beam). Plotting the HI profiles at each pixel position revealed that the Galactic HI was mainly visible in 3 consecutive channels (i.e the Galactic HI has a narrow velocity width as compared to the NGC 6822's emission). Using this information, we were able to consider emission detected in more than 3 consecutive channels as real emission from NGC 6822. Any emission spanning across $\leqslant$ 3 channels was blanked. In a few positions, the Galactic HI was seen across 5 consecutive channels. In these cases, we considered emission detected in more than 5 consecutive channels as real emission from NGC 6822. The above process was repeated for the entire velocity range to check how much galaxy flux could be lost when Galactic emission was considered to span across 3 channels. A flux loss of ~ 0.3% was calculated. This shows that the above process does not interfere with NGC 6822's emission, but is able to subtract well the Galactic HI from the galaxy.

The final cube was created by removing noise pixels in each channel. The original cube was first smoothed to twice the original resolution. All the pixels below the 3σ of the smoothed image were blanked out. The resulting cube still had some imperfections in regions with very bright emission. These were blanked by hand. The final masked cube was later used to derive the HI global profile, the intensity HI maps, the HI velocity maps and the HI dispersion maps. The HI maps where derived using a task XGAUFIT in AIPS. This task produces maps by fitting Gaussians to the data cube.

by using first order Gaussian fitting

Table 2.2: Parameters of the KAT-7 Observations.

Parameter	Value
Start of observations	August 2014
End of observations	December 2014
Total integration per pointing	~ 35 hrs
FWHM of primary beam	1.27°
Total bandwidth	12.5 MHz
Final channel width (4 × 0.64 km s^{-1})	2.56 km s^{-1}
Final number of channels(4096/4)	1024
Map gridding	30″ by 30″
Map size	256 by 256
Flux/bandpass calibrator	1934-638
Phase calibrator	1938-155
Robust = 0 weighting function	
FWHM of synthesized beam	209″× 193″
RMS noise	3.7 mJy/beam
Column density limit	
(3σ over 16 km s^{-1})	1.0×10^{19} cm^{-2}

2.3 HI distribution

The global HI emission profile of NGC 6822 is shown in Figure 2.1. The profile was derived from the primary beam corrected masked channel maps. We find HI emission between -118 to 7 km s^{-1}. This is similar to the range of velocities detected by de Blok & Walter (2000). A mid-point velocity of -55 ± 2 km s^{-1} is found. This is identical to the value found by de Blok & Walter (2006a). The profile widths at 20% and 50% levels are 105 ± 0.6 km s^{-1} and 90 ± 2 km s^{-1}. We integrated the flux over the global profile and measured the total integrated flux of 2440 ± 20 Jy km s^{-1}. Adopting a distance to NGC 6822 of 0.48 Mpc (Feast et al., 2012), we find the total HI mass of M_{HI} = (1.3 ± 0.1) ×10^8 $M_\odot$. This is 23 % more than the ATCA measurements (de Blok & Walter, 2006a) (M_{HI} = 1.0 × 10^8$M_\odot$) and very close to the Parkes single dish measurement of (de Blok & Walter, 2006a) (M_{HI} = 1.2 ×10^8 $M_\odot$), all were corrected to the distance of 0.48 Mpc (Feast et al., 2012). The HI masses were measured over the same area.

Figure 2.2 shows the HI column density map superposed on the Digital Sky Survey (DSS) image. We integrated the HI column densities from -118 to 7 km s^{-1} in the KAT-7 primary beam corrected cube. The lowest contour in our column density map is 1×10^{19} cm^{-2}. This is consistent with the 3σ noise limit calculated over 16 km s^{-1}. Our derived column density limit is significantly better than the 3σ sensitivity of 4×10^{20} cm^{-2} calculated over 16 km s^{-1} of de Blok & Walter (2000). The HI emission is seen to be much larger than the optical body, which is typical of irregular galaxies. An HI diameter of ~ 1.2° is measured along the major axis at the lowest contour. This is in agreement with the Parkes single dish measurement (de Blok & Walter, 2000).

The HI column density grey scale map of Figure 2.3 shows structures present in

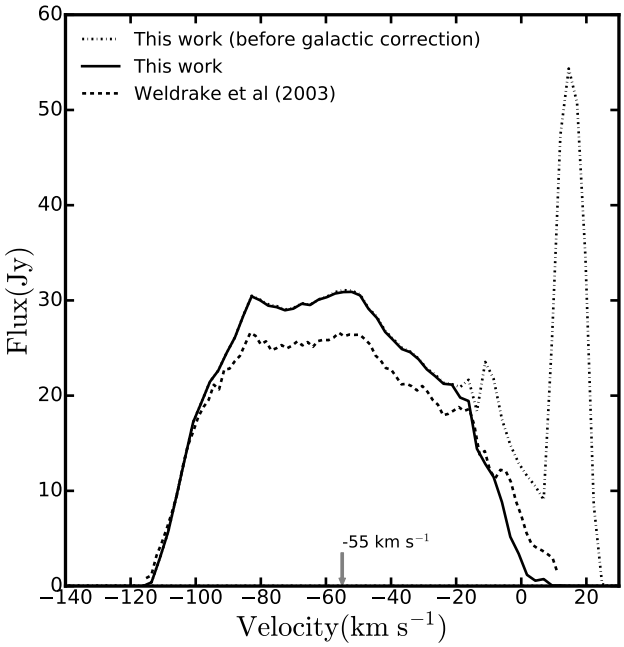

Figure 2.1: HI emission for NGC 6822 with the dash line showing the profile not corrected for Galactic emission. The black solid line shows the KAT-7 profile after the Galactic emission has been subtracted while the grey solid line shows the ATCA profile corrected for Galactic HI. The systemic velocity of the profile is shown at -55 km s^{-1}.

the HI disk. The HI hole as well as the arm in the South East previously reported by de Blok & Walter (2000) are clearly visible in the KAT-7 observations. The velocity field map of NGC 6822, shown at the top of Figure 2.4, is seen to have symmetric and undisturbed velocities similar to most low mass, late-type galaxies. This will be used to derive the kinematical properties of the galaxy using the tilted ring model explained in Section 2.4. At the bottom of Figure 2.4, we can see that the velocity dispersion varies from 10 km s^{-1} in the center to $\sim$ 4 km s^{-1} at the edge of the disk. The maps where derived using a task XGAUFIT in AIPS. This task produces maps by fitting Gaussians to the data cube.

Figure 2.5 shows the azimuthally averaged radial HI density profile of NGC 6822. This is compared to the radial profile derived from the previous ATCA observation, smoothed to the KAT-7 resolution (Weldrake et al., 2003).The profile was derived using the GIPSY task ELLINT by applying the tilted ring kinematical parameters described in Section 2.4. The values for the derived HI surface densities are given in Table 2.3

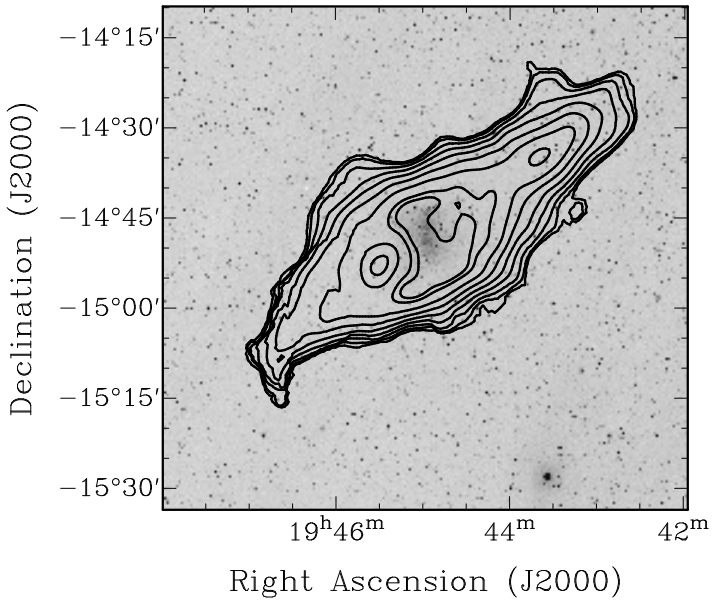

Figure 2.2: KAT-7 total column density collapsed map of NGC 6822 overlaid on an optical DSS image. The column density contours are 0.01, 0.02, 0.04, 0.08, 0.16, 0.32, 0.64, 1.28, and 1.60 $\times 10^{21}$ cm^{-2}. The lowest contour is at a 3σ level.

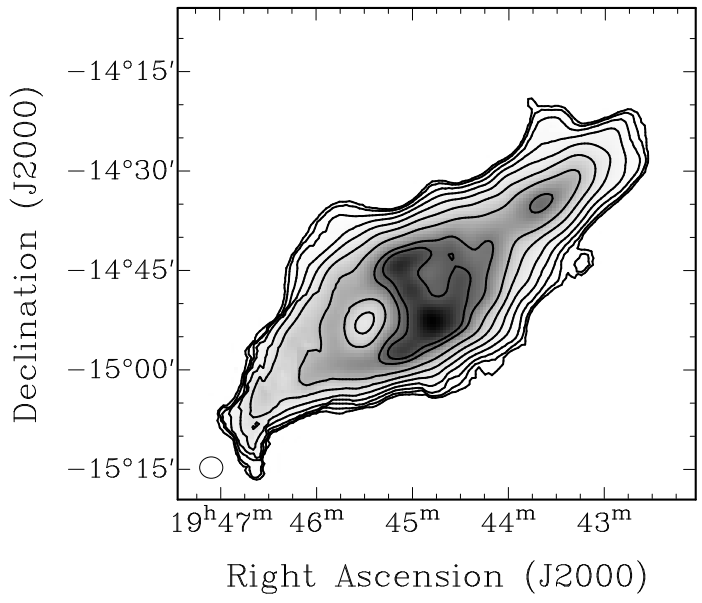

Figure 2.3: Integrated HI column density map. The greyscale levels run from 1×10^{19} cm^{-2}(white) to 2.52 $\times 10^{21}$ cm^{-2} (black). The column density contours are 0.01, 0.02, 0.04, 0.08, 0.16, 0.32, 0.64, 1.28, and 1.60 $\times 10^{21}$ cm^{-2}. The beam is shown in the bottom left corner. An HI hole is clearly seen SE of the bright central parts.

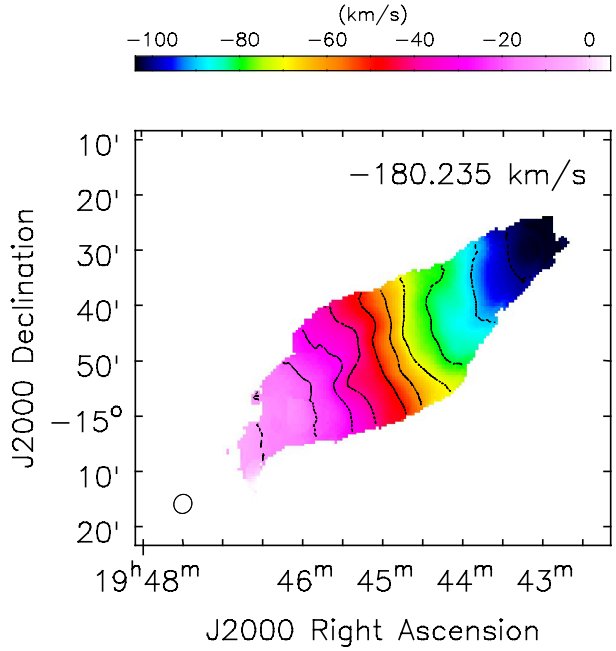

(a) Observed velocity field map

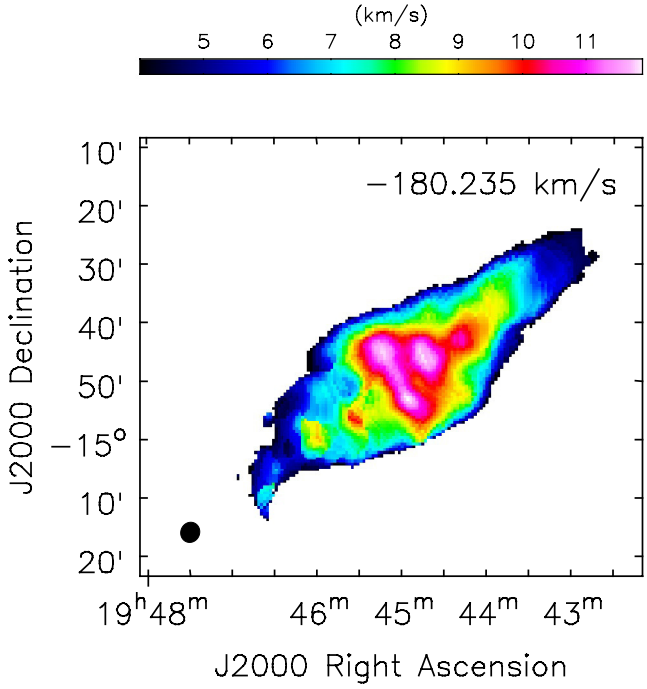

(b) Velocity dispersion map

Figure 2.4: First (top) and second (bottom) moment maps of NGC 6822 from the KAT-7 data cube. The top shows the observed velocity field. The contours are -100, -90, -80, -70, -60, -50, -40, -30, -20, and -10 km s^{-1}. The bottom shows the observed velocity dispersion map.

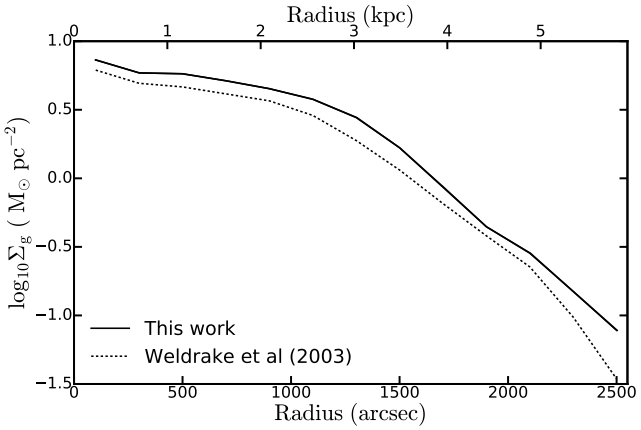

Figure 2.5: Comparison of the ATCA (Weldrake et al., 2003) and the KAT-7 radial profiles. The profiles have been corrected for helium and other elements by multiplying the surface densities by 1.4.

2.4 HI kinematics

2.4.1 Tilted ring model

A tilted ring model (Rogstad et al., 1974) is based on the assumption that the velocities we observe are mainly circular rotational velocities and that the disk galaxy can be described by a set of concentric rings. Each ring has a set of defining kinematical parameters; central co-ordinates (x_c, y_c), a systemic velocity V_{sys}, an inclination i, a position angle (P.A), and the rotation velocity, V_{rot}. The line of sight velocity at any (x,y) position in a ring with radius R is given by

$$V(x,y) = V_{sys} + V_{rot}\sin(i)\cos(\theta), \tag{2.1}$$

where θ is the position angle with respect to the receding major axis measured in the plane of the galaxy, θ is related to the actual P.A. in the plane of the sky by

$$\cos(\theta) = \frac{-(x-x_0)\sin(P.A.) + (y-y_0)\cos(P.A.)}{R}. \tag{2.2}$$

$$\sin(\theta) = \frac{-(x-x_0)\cos(P.A.) + (y-y_0)\cos(P.A.)}{R\cos(i)}. \tag{2.3}$$

2.4.2 Deriving the rotation curve

We derived the rotation curve of NGC 6822 by applying the tilted ring model to the velocity field using the GIPSY (van der Hulst et al., 1992) task ROTCUR (Begeman, 1989). We determined parameters for each ring independently by using a ring width and spacing between rings corresponding to the beam width of ~ 200 arcsec. Our final ring radius was 2500 arcsec because beyond this radius the S/N dropped drastically. The parameters that were fitted are: the dynamical center (x_c, y_c), the systemic velocity V_{sys}, the position angle PA, the inclination i, and the rotation velocity V_{rot}. We set V_{exp}, the expansion velocity, to zero. At first, we ran the tilted

ring model with all the parameters free out to the edge of the optical disk (R_{25} ~ 1.1 kpc (de Vaucouleurs, 1991)). The V_{sys} and the rotation center are expected to be the same for all rings, at least within the optical disk. From this, the average values of the V_{sys} and the (x_c, y_c) were fixed. The fixed systemic velocity and the dynamical center were used to run the tilted ring model out the edge of the HI disk. We iterated by fixing either the position angle or the inclination or both to derive the best fit model. As the minor axis provides little information regarding the rotation curve, an exclusion angle of 15° was used to give more weight to the points around the major axis. The data were also weighted by applying a $|cos(\theta)|$ weighting, where θ is the azimuthal angle in the plane of the galaxy from the major axis. Once we produced the best fit rotation curve for both sides, we also derived the curves for the approaching and receding sides to see possible departure from axisymmetry. The errors on V_{rot} were derived using Equation 2.4 (Carignan et al., 2013).

$$\Delta V = \sqrt{\sigma^2(V) + \left(\frac{|V_{app} - V_{rec}|}{2}\right)^2}, \tag{2.4}$$

where σ_V is the intrinsic dispersion inside the rings and V_{app} and V_{rec} are respectively the approaching and receding side velocities.

Equation 2.4 will give larger errors than what is often stated in the literature where people only use the intrinsic dispersion in the rings as their errors (Carignan et al., 2013). However, since at the mass model stage, we will fit this rotation curve with axisymmetric components, we think the differences between both sides of the galaxy are more representative of the true uncertainties in those models.

The velocity dispersions in NGC 6822 are large enough to contribute to the gravitational support of the galaxy. In order to obtain more reliable rotation velocities for the galaxy, we correct for the pressure gradient in the gas using the asymmetric drift correction. Following the method described in Côté et al. (2000), we correct for the asymmetric drift as follows:

$$V_c^2 = V_{rot}^2 - 2\sigma\frac{\delta\sigma}{\delta \ln R} - \sigma^2\frac{\delta \ln \Sigma}{\delta \ln R}, \tag{2.5}$$

where V_c is the corrected velocity, V_0 is the observed one, σ is the velocity dispersion and Σ is the gas density. Table 2.3 shows the parameters used to correct for the asymmetric drift together with the corrected velocities.

2.4.3 KAT-7 rotation curve and position velocity diagram

The resulting rotation curves (approaching, receding, both sides) of NGC 6822 derived from the velocity field are shown in Figure 2.6. We adopted the model with

constant inclination and varying position angle due to the following reasons: 1) it is difficult to constrain the varying inclination in the inner region of the galaxy due to the presence of the bar major axis which appears to be perpendicular to the major axis of the disk as shown in Figure 2.2, and 2) deriving surface densities using varying inclinations derived from the tilted ring parameters show that the inner regions of the galaxy have low HI column densities as compared to the outer regions of the galaxy which is not consistent with the data as shown in Figure 2.3. We derive the dynamical center of the galaxy at α, δ (J2000) = 19h44m58.0s, -14d48m11.9s, and its systemic heliocentric velocity, $V_{\rm sys}$ = -55 $\pm$ 3 km s^{-1}. This is similar to the global profile value. The dynamical center agrees within 1 arcsec, with the optical center α, δ (J2000) = 19h44m57.9s and DEC -14d48m11.0s (de Vaucouleurs, 1991). We derive the mean P.A. = 118° and i = 66°. Between 500 ~ 900 arcsec, the difference between the approaching and receding sides become more prominent for i and PA but, curiously, the smallest for $V_{\rm rot}$. This correspond to the edge of the inner disk. For the velocities at R > 2000 arcsec, the difference between the approaching and receding side can be attributed to the residual Galactic HI contamination. In this case, the receding side which is affected by the Galactic HI is seen to have higher rotation velocity values as compared to the approaching side.

Our derived kinematics of NGC 6822 are in agreement with the literature. Weldrake et al. (2003) derived the $V_{\rm sys}$ = -54.4 km s^{-1}, mean P.A. = 118°, and the mean i = 63° of NGC 6822 from their tilted ring results. The KAT-7 RC agree very well with the ATCA data, see Figure 2.7 a while allowing us to extend the rotation data ~ 1 kpc further out. The consistency between the derived kinematical parameters from both observations show that the larger extent of the KAT-7 RC comes from the increased sensitivity which allows us to detect the low column density gas in the outer radii.

The best way to check that our derived rotation curve best represents the kinematics of the disk is to overlay the rotation curve on a position-velocity (PV) diagram obtained along the major axis, as shown in Figure 2.8. The rotation curve shows a good representation of the dynamics of the galaxy. The RC appears to decline in the outer regions due to the change in PA.

We have also compared the observed velocity field with the model velocity field constructed from the tilted ring fits for both, approaching and receding sides. These are shown in Figure 2.9. The residual maps derived from the model velocity maps for each side show similar residual pattern with no large residuals seen. Most of the residuals are < $\pm$ 10 km s^{-1}. An increase of the residuals at the HI hole position is clearly seen.

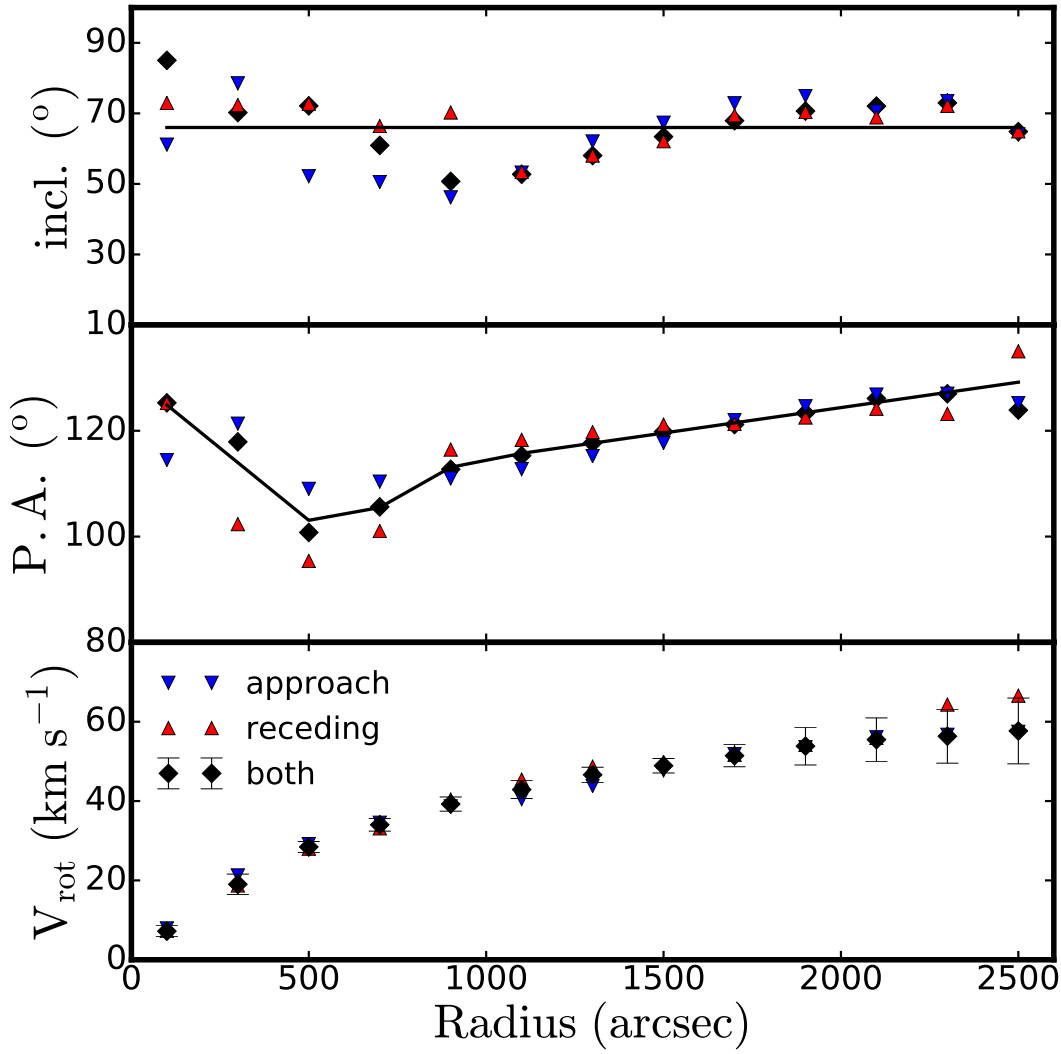

Figure 2.6: Results of the tilted ring fits for NGC 6822. For the middle and top panels, the blue and red triangles and the black diamonds show the behavior of the PA and inclination as free parameters while the black solid lines show the behavior of the PA and inclination fixed to the model used to derive the final rotation curve. In this case the PA is varying while the inclination is fixed to the mean value. The final adopted parameters are shown by the continuous lines in the top two panels. For the bottom panel, the blue triangles represent the curve for the approaching side while the red triangles represents the curve for the receding side.

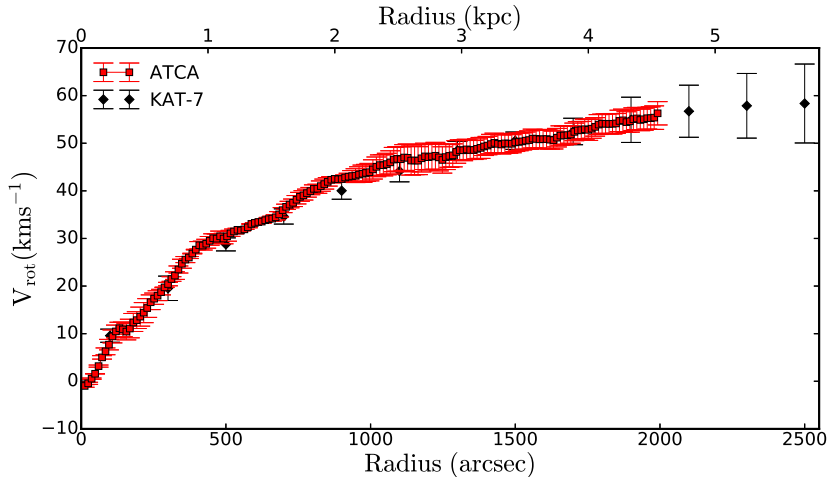

Figure 2.7: Comparison between the KAT-7 (black diamonds) and the ATCA (red squares) rotation curves.

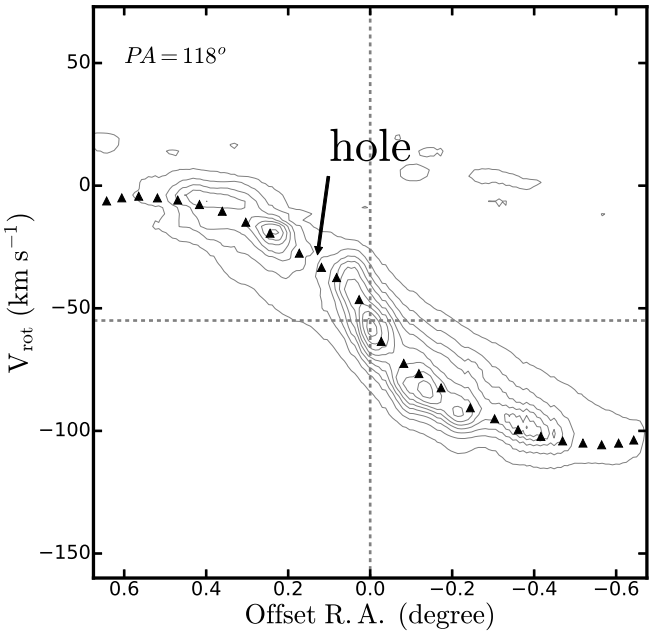

Figure 2.8: Position velocity diagram of NGC 6822 with the projected rotation curve over plotted. The dotted grey lines represent the centre of the galaxy and the systemic velocity. Superimposed is the rotation curve derived from the tilted ring model, corrected for the inclination of a slice along the galaxy major axis.

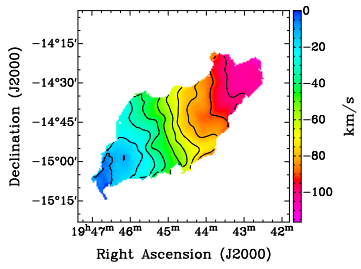

(a) Observed velocity field

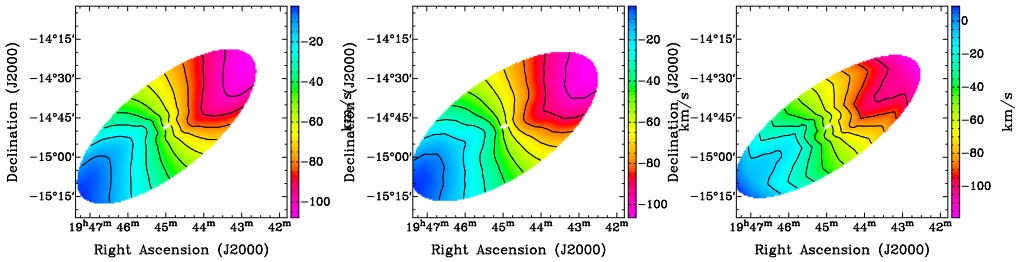

(b) Model map (both) (c) Model map (approaching) (d) Model map (receding)

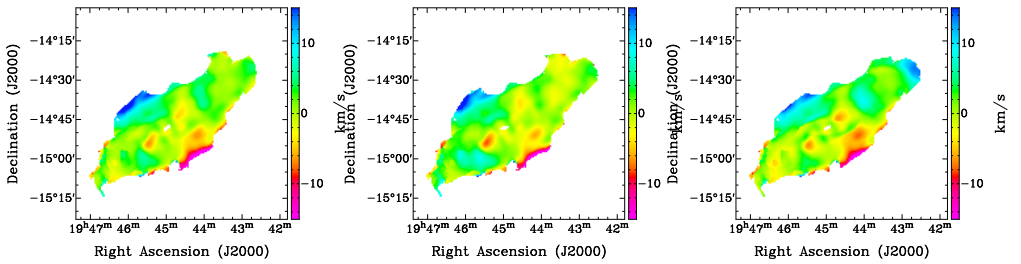

(e) Residual (both) (f) Residual (approaching) (g) Residual (receding)

Figure 2.9: Comparison of the observed velocity field top panel (a) and the circularly symmetric model velocity fields (middle panel) derived from the tilted ring fits for both (b), approaching (c), and receding (d) sides. The contours for the velocity fields and model velocity fields run from -100 to 10 km s^{-1} in steps of 10 km s^{-1}. The bottom panel shows the residual velocity fields (observed-model) for both (e), approaching (f), and receding (g) sides.

Table 2.3: Radial variation of the HI surface densities Σ_g, the gas velocity dispersion σ and the rotation velocity for the KAT-7 Data of NGC 6822 from moment analysis.

Radius arcsec	Σ_g $M_\odot pc^{-2}$	σ km s^{-1}	V_0 km s^{-1}	Δ V km s^{-1}	σ/V %	V_c km s^{-1}
100	2.5	10.7	7.2	1.6	140	9.6
300	4.4	10.4	19.0	2.3	54	19.5
500	6.6	9.8	28.4	1.9	34	28.8
700	7.8	8.8	34.0	2.1	25	34.6
900	5.6	8.4	39.2	1.6	21	40.1
1100	2.3	7.9	42.9	2.4	18	44.1
1300	1.7	7.2	46.6	2.3	15	48.5
1500	1.3	5.6	48.9	2.1	11	50.5
1700	0.9	5.2	51.4	2.5	10	52.5
1900	0.6	4.7	53.8	2.9	9	54.9
2100	0.3	3.6	55.5	3.8	7	56.7
2300	0.2	2.7	56.3	4.6	5	57.8
2500	0.1	1.0	57.7	6.8	2	58.3

Notes. Column (1) gives the radius, column (2) the surface densities, column (3) the velocity dispersion, column(4) the observed rotation velocities, column (5) the errors of those velocities, column (6) the ratio between the velocity dispersion and the rotation velocity, and column (7) the corrected velocities used for the mass models.

2.5 Mass models and dark matter content

The rotation curve reflects the dynamics of the disk due to the total mass of the galaxy, luminous and dark matter. Dwarf irregulars, like most low-mass surface density galaxies are believed to be dominated by dark matter at all radii due to the small contribution of luminous matter (stars and gas) to the total dynamics (Carignan & Beaulieu, 1989). The extended HI rotation curves of dwarf irregulars allow us to probe dark matter potentials to much larger radii, making them ideal objects for studying dark matter properties in galaxies. To this end, we decompose the observed rotation curve of NGC 6822 into the luminous and dark matter mass components and verify if dark matter indeed dominates the total dynamics of systems such as NGC 6822.

2.5.1 Dark matter models

2.5.1.1 Isothermal halo model

This model is the representation of a core like halo model (Begeman et al., 1991). This model describes the distribution of dark matter. It has the following form:

$$\rho_{\rm ISO}(r) = \frac{\rho_0}{1+(r/r_c)^2}, \tag{2.6}$$

where ρ_0 and r_C are the central density and core radius of the halo, respectively. This gives rise to the mass distribution with a sizable constant density core ($\rho \sim r^0$)

at centers of galaxies. The rotation velocity induced by the mass distribution is given as

$$V_{\rm ISO}(r) = \sqrt{4\pi G \rho_0 r_c^2 \left[1 - \frac{r}{r_c}\arctan\left(\frac{r}{r_c}\right)\right]} \tag{2.7}$$

2.5.1.2 The Navarro, Frenk, and White DM model (NFW)

The NFW profile, also known as the universal profile (Navarro et al., 1997) is the commonly adopted DM halo profile in the context of the ΛCDM cosmology. It was derived from the N-body simulations. The density profile is given by

$$\rho_{\rm NFW}(R) = \frac{\rho_i}{(r/r_s)[(1+r/r_s)]^2}, \tag{2.8}$$

where r_s is the characteristic radius of the halo and ρ_i is related to the density of the universe at the time of collapse of the DM halo. This gives a cusp feature having a power law mass density distribution $\rho \sim r^{-1}$ towards the centers of the galaxies. The corresponding rotation velocities are given by

$$V_{\rm NFW} = V_{200}\sqrt{\frac{\ln(1+cx - cx/(1+cx)}{x[\ln(1+c) - c/(1+c)]}}, \tag{2.9}$$

where x is defined as r/r_{200}. c is the concentration parameter defined as r_{200}/r_S, V_{200} is the rotation velocity at the radius r_{200} where the density contrast with respect to the critical density of the universe exceeds 200, roughly the viral radius.

2.5.1.3 Gas and stellar components

The HI gas surface density profile was computed from the observed HI column density map. We use the GIPSY task ELLINT and apply the tilted ring parameters given in Section 2.4. The gas surface density profile of the galaxy was scaled by 1.4 to take into account Helium and other metals. The HI surface density profile is presented in Figure 2.5. We convert the gas surface density to the corresponding gas rotation velocities by using the GIPSY task ROTMOD, assuming an infinitely thin disk. We use the Wide Field Infrared Survey Explorer (WISE) surface brightness profiles at 3.4 micron to account for the stellar contribution. At 3.4 microns, WISE probes the emission from the old stellar disk population and is also less affected by dust. The luminosity profile is converted into stellar mass density by adopting the method described by Oh et al. (2008). First the surface brightness profile in mag/arcsec^2 is converted to luminosity density in units of $L_\odot$/pc^2 and then converted to mass density using the following formulae:

$$\Sigma[M_\odot pc^{-2}] = (M/L)_{*3.4} \times 10^{-0.4(\mu_{3.4} - C^{3.4})}, \tag{2.10}$$

where $(M/L)_{*3.4}$ is the stellar mass to light ratio in the 3.4 micron, $\mu_{3.4}$ is the surface brightness in mag/arcsec^2 and $C^{3.4}$ is the constant value that is used to convert

mag/arcsec^2 to $L_{\odot} pc^{-2}$. C$^{3.4}$is given by $M_{\odot}^{3.4}$ + 21.56, where $M_{\odot}^{3.4}$ = 3.24 is the absolute magnitude of the sun in the 3.4 micron band. The derived profile was then converted to stellar rotation velocities using the GIPSY task ROTMOD.

2.5.2 Fitting NFW and ISO models for NGC 6822

The GIPSY task ROTMAS was used to construct the mass models for NGC 6822. We fitted the ISO and NFW models to the rotation curve derived from the tilted ring model, taking into account the mass of the luminous matter (stars and gas). In all the fittings, the gas surface densities were fixed. Inverse squared weighting of the rotation curves with uncertainties was used during the fitting procedure.

The mass to light ratio M/L is one of the largest source of uncertainty in deriving the mass model. The value of M/L cannot be derived from the rotation curve alone. We scale the upper and lower limits of the mass to light ratio using 2 different assumptions. 1) we fix the M/L of the stellar component to the predetermined value of M/L $\approx$ 0.2 at mid-infrared band from the literature (Lelli et al., 2016), and 2) we derive a set of fits where M/L is left as a free parameter. In this case we let the fitting program choose its best value.

2.5.3 Results from the ISO and NFW DM halo fits

The fitted parameters for the mass models are summarized in Table 2.4 and Figure 2.10 for both the ISO and the NFW halo models. We find that the ISO halo model provides a better fit than the NFW model in all cases. The NFW model fails to fit the rotation curve irrespective of the assumption of M/L used. Both NFW models gave unphysical fitted parameters M/L= 0 (free) or too small value of c (model). On the other hand, the ISO halo model provides reasonable halo parameters. The best fit to the rotation curve: i.e. we let M/L be a free parameter in the fit produces the smallest value of the reduced χ^2. We tried to constrain the maximum value of M/L$_*$ by scaling the stellar rotation curve to contribute maximally to the observed rotation curve. In this case, sensible results are obtained when the M/L value is lowered to the predetermined value of 0.2. This shows that NGC 6822 is not a maximum disc galaxy. Our derived M/L values of NGC 6822 are consistent with the literature. Weldrake et al. (2003) derived the best fit M/L ratio of 0.10 $\pm$ 0.13 and 0.35 $\pm$ 0.04 for NGC 6822. The small derived M/L ratio confirms that the stellar component of NGC 6822 has very little impact on the total mass of the system. It is clear from Figure 2.10 that dark matter is the most massive component contributing to the total rotation curve. This makes NGC 6822 dark matter dominated even in the rising part of the rotation curve (for R > 1 kpc).

The distribution of dark matter in NGC 6822 is typical of most dwarf irregular

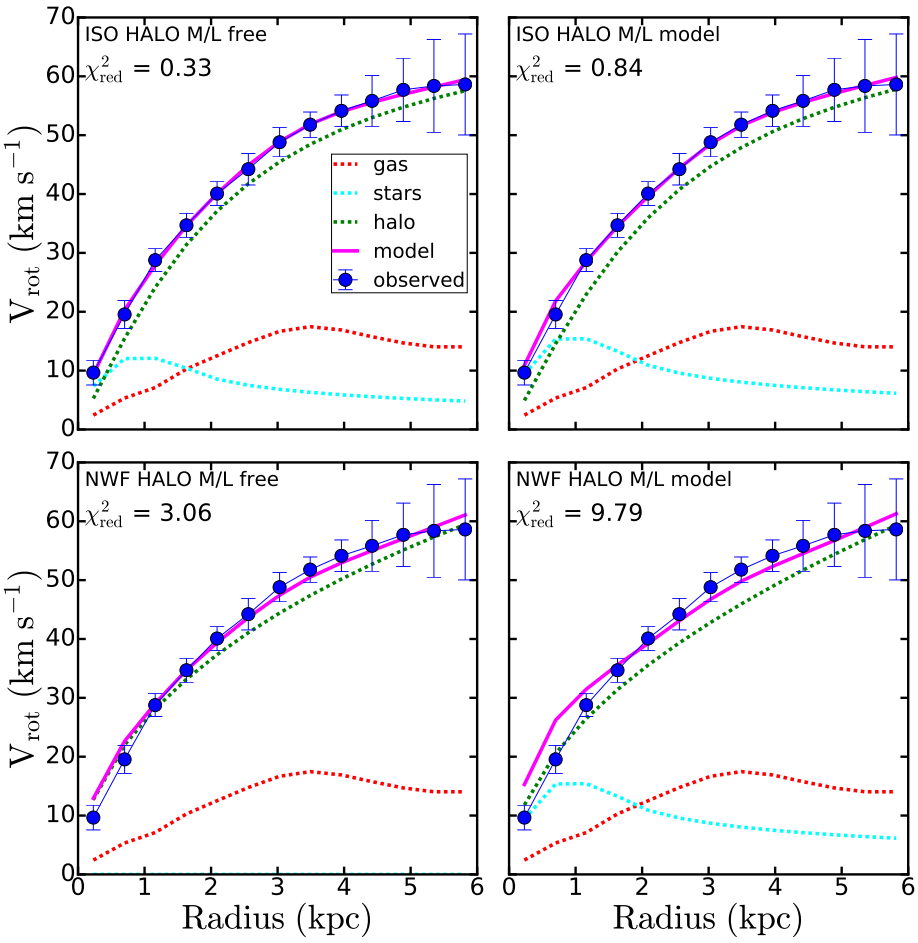

Figure 2.10: ISO and NFW mass modeling results of NGC 6822. The decomposition of NGC 6822 rotation curve using two assumption of Υ_*. The blue circles indicate the observed rotation curve, the magenta lines show the fitted rotation curve, the green dotted lines indicate the dark matter rotation velocities, and the red dot-dashed and blue dashed lines show the rotation velocities of the gas and of the stellar components respectively.

galaxies when compared with the literature (e.g., de Blok et al., 2008; Oh et al., 2011) show that most dwarf irregular galaxies in their sample are better described by a core-like model dominated by a central constant-density core with small M/L ratios.

2.5.4 MOND models for NGC 6822

A alternative to dark matter is the modified Newtonian dynamics (MOND)(Milgrom, 1983, 1988). MOND is a phenomenological modification of Newton's law of gravitation which produces the dynamics of galaxies, without the need for additional dark matter. Only the stellar and gas contributions are needed to explain the rotation

Table 2.4: Results for the mass models of NGC 6822.

	ISO Halo			
Assumption	Υ_*	R_c	ρ_0	χ^2_{red}
(1)	(2)	(3)	(4)	(5)
M/L free	0.12	1.87 ± 0.07	29.22 ±1.38	0.33
M/L model	0.20	2.06 ± 0.09	25.59± 1.40	0.84
	NFW Halo			
Assumption	Υ_*	c	R_{200}	χ^2_{red}
(6)	(7)	(8)	(9)	(10)
M/L free	0.00	3.34 ± 1.14	165.39 ±54.39	3.06
M/L model	0.20	0.01±	1120.71±	9.79

Notes. Columns 1 and 6, the stellar Υ_* assumption. Column 2 and 7, Υ_* . Column 3, fitted core radius of the ISO halo model(10^{-3} $M_\odot pc^{-3}$). Column 4, fitted core density of the pseudo-isothermal halo model (10^{-3} $M_\odot$ pc^{-3}). Column 9, the radius in kpc where the density contrast exceeds 200. Column 8, concentration parameter c of the NFW halo model. Columns 5 and 10, reduced χ^2 value. The dotted line (...) are due to unphysical large values of uncertainties.

curve.

2.5.4.1 MOND models using the *Standard* Interpolation Function

The standard interpolating function (Milgrom, 1983) is given as

$$\nu(x) = \frac{x}{\sqrt{(1+x^2)}}. \tag{2.11}$$

For x $\ll$ 1 the system is in deep MOND regime with $g = (g_N a_0)^{1/2}$ and for x $\gg$ 1 the gravity is Newtonian. The MOND rotation curves is given by

$$V^2_{\rm rot} = \frac{V^2_{\rm sum}}{\sqrt{2}} \sqrt{1 + \sqrt{1 + 2(2ra_0/V^2_{\rm sum})^2}}. \tag{2.12}$$

where

$$V^2_{\rm sum} = V^2_b + V^2_d + V^2_g, \tag{2.13}$$

where V_b, V_d, and V_g are the contributions from the bulge, the disk, and the gas to the rotation curve. In the case of the Irregular galaxy NGC 6822, there is no bulge to consider.

2.5.4.2 MOND models using the *Simple* Interpolation Function

The simple interpolation function (Famaey & Binney, 2005) is given by

$$\nu_x = \frac{x}{1+x}. \tag{2.14}$$

Using the same procedure as in the previous section, we obtain the rotation velocities:

$$V^2_{\rm rot} = \sqrt{V^2_b + V^2_d + V^2_g} * \sqrt{a_0 * r + V^2_b + V^2_d + V^2_g}. \tag{2.15}$$

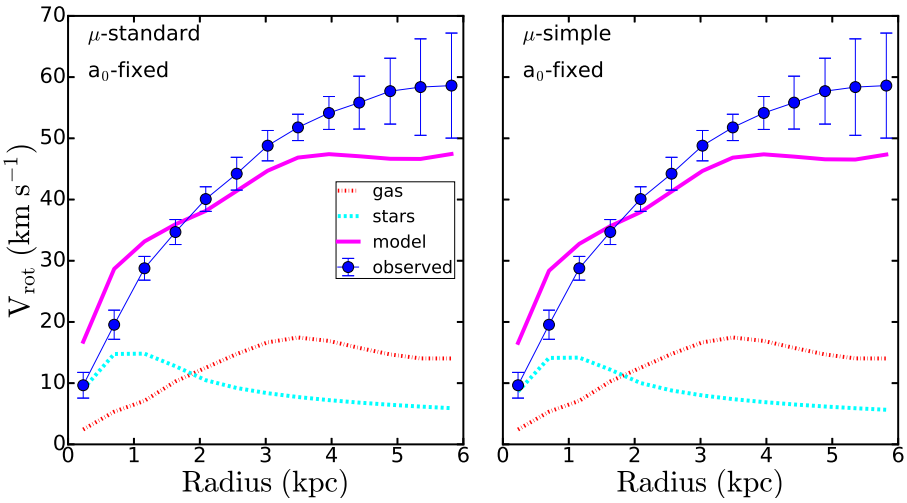

Figure 2.11: MOND mass models with a_0 fixed for the standard (left) and the simple (right) interpolation functions for NGC 6822 using the derived rotation curve. The red dot-dashed curve is for the HI disk, the dashed light blue curve is for the stellar disk, and the continuous purple curve is the MOND contribution.

Table 2.5: Results for the MOND models of NGC 6822 for the KAT-7 Data. The value of a_0 is fixed as 1.21×10^{-8} cms^{-2} for both models.

μ	Parameter	Result
Standard	(M/L)	0.18 ± 0.10
	χ^2_{red}	59.50
Simple	(M/L)	0.17 ± 0.09
	χ^2_{red}	59.29

Famaey & Binney (2005) found that the simple interpolating function gives more plausible M/Ls compared to the standard function.

2.5.5 MOND fits and results of NGC 6822

The MOND fitting procedure has one free parameter. We fit the rotation curve with a_0 fixed to the universal constant of 1.21×10^{-8} cms^{-2} while letting M/L free for the standard and the simple interpolation functions. Results for MOND fits are summarized in Table 2.5 and Figure 2.11. We see that using the universal constant a_0 the MOND fit fails to reproduce the distribution of matter in NGC 6822.

2.6 Star formation threshold

A threshold in the gas surface density has been inferred from the relationship between the optical edges of galaxies and their HI column densities. The concept of the star formation threshold is usually explained in terms of the Toomre-Q parameter (Toomre, 1964). The parameter is defined as

$$Q(r) = \frac{c_s k}{\pi G \Sigma_g}, \tag{2.16}$$

where c_s is the sound speed in the gas, G is the gravitational constant, Σ_g is the gas surface density and k is the epicyclic frequency, defined as:

$$k^2 = 2\left(\frac{V_{\rm rot}^2}{r^2} + \frac{V_{\rm rot}}{R}\frac{dV_{\rm rot}}{dr}\right), \tag{2.17}$$

where $V_{\rm rot}$ is the rotation velocity in km s^{-1}, and R is the radius in parsecs. Kennicutt (1989) found that a modified Toomre (1984) Q criterion, a simple thin disk gravitational stability condition, could satisfactorily describe the star formation threshold gas surface densities in active star forming galaxies. For a thin isothermal gas disk, instability is expected if the surface density exceeds a critical value:

$$\Sigma_c = \alpha_Q \frac{\sigma k}{\pi G}, \tag{2.18}$$

where σ is the gas velocity dispersion and α_Q is a dimensionless constant close to unity which is included to account for a more realistic disk. The α constant is fitted to the threshold values of the radially varying quantity

$$\alpha_Q = \Sigma_g / \Sigma_c. \tag{2.19}$$

Kennicutt (1989) adopted a constant velocity dispersion of 6 km s^{-1} and derived the α value of 0.63. If Σ_g exceeds Σ_c then the disk will be unstable to axisymmetric disturbances and large scale star formation can occur. The minimum density at which gas becomes unstable is a function of k and σ of the gas, and so the threshold density for cloud formation, which leads to star formation, can vary with radius in the galaxy. Hunter et al. (1998) used the Toomre criterion and measured a mean value of $\alpha_Q \approx 0.3$ in irregular galaxies, a factor of two lower than that found by Kennicutt (1989) for spiral galaxies. This implies that the gas in irregular galaxies is more stable than the gas in spiral galaxies. Although part of this difference is due to the different velocity dispersion used, they explain that for dwarf irregulars with close to solid body rotation curves, the local shear rate, rather than the Coriolis force best describes the destruction rate of giant clouds. This implies that for irregular galaxies such as NGC 6822, the threshold stability criterion would have to be modified to take into account the local shear rate. This threshold based on the local shear rate

(Hunter et al., 1998), is described by Oort's constant A,

$$A = -\frac{1}{2} r \frac{d\Omega}{dr} = \frac{1}{2}\left(\frac{V_{\rm rot}}{r} - \frac{dV_{\rm rot}}{dr}\right), \tag{2.20}$$

where Ω is the angular speed. Then the shear critical threshold has the form

$$\Sigma_A = \frac{\alpha_A A \sigma}{\pi G}, \tag{2.21}$$

and $\alpha_A \sim 2.5$

We examine the star formation threshold throughout NGC 6822 as a function of radius to determine if a subcritical gas density is preventing the galaxy from large scale star formation. We use a velocity dispersion of σ = 7 km s^{-1} which represents the median value derived from the azimuthally averaged HI velocity dispersion radial profile. We have assumed α_Q = 1. The HI surface density, Σ_g is multiplied by a factor of 1.4 to account for helium and other elements. We have used the Hα images to determine the distribution of star formation in this galaxy and looked for the outer limits of star formation. Hα emission is an excellent tracer of the formation of the most massive stars and is readily accessible. We use a clean calibrated Hα map from de Blok & Walter (2006a) and derive the Hα surface density using our tilted ring parameters described in Section 2.4. Figure 2.12 shows contours of HI superposed on the Hα map. We see that the Hα is found within an observed HI column density $\geqslant 10^{21}$ cm^{-2}.

From these data we have estimated the critical densities using the Toomre criteria and the cloud growth criteria based on shear which can be seen in Figure 2.13. At all radii, the critical densities, Σ_c fails to predict star formation while the shear critical densities, Σ_A predicts the star formation fairly well in the inner regions of the galaxy R $\lesssim$ 3 kpc. Figure 2.14 shows the ratio of the observed gas surface density to the critical surface densities Σ_c and Σ_A (α) in NGC 6822. Also plotted for comparison are the Hα surface densities which indicate star formation rate. The star formation traced by the Hα is seen to be higher in regions where the α_A values are high showing a similar radial trend between the star formation and α_A.

Kennicutt (1989) determined an average value for the parameter α by finding the mean value of Σ_g/Σ_c at the radial limit of the observed HII regions. For NGC 6822, the limit of HII regions, as seen from the Hα profile is located at a radius of $\sim$ 2.8 kpc. The mean value of α_Q at that radius is $\sim$ 0.25. This is a factor 2.5 less than the value derived by Kennicutt (1989). However, this value is consistent with the derived α_Q values of most irregular galaxies. Hunter et al. (1998) derived a mean α_Q value of 0.26 for Sextans A, 0.30 for DDO 155, and 0.36 for DDO 168. Similar values were derived for other dwarf irregulars in their study sample. This result shows that for

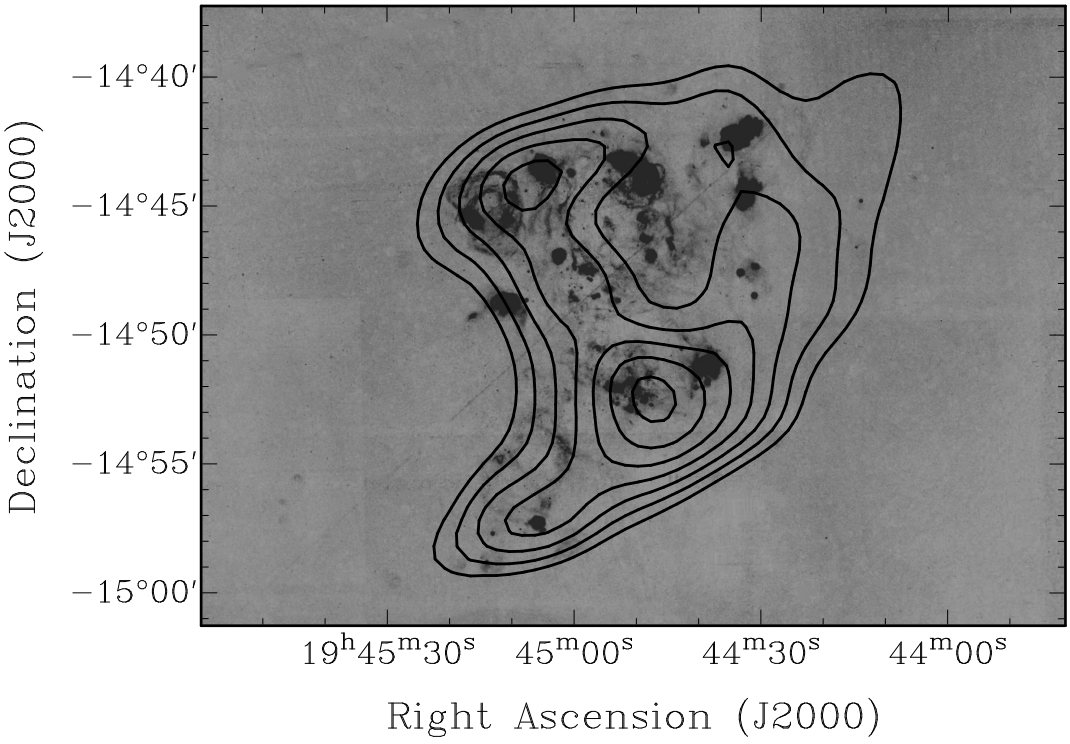

Figure 2.12: HI column density contours superposed on our Hα image. The column density contours are 1.0, 1.2, 1.4, 1.6, 1.8, 2.0, 2.2, and 2.4 $\times 10^{21}$ cm^{-2}. The lowest contour covering the Hα region is 1.0×10^{-21} cm^{-2}.

the Toomre-Q criterion, star formation in NGC 6822 is consistent with most dwarf irregulars.

The α_A values derived from the shear critical density show quite a different picture in the inner regions of the galaxy. The α_A values range from 0.6 to 1 within the radial limit of the HII regions. The peak value around 0.7 kpc is not considered physical due to the bump in the position angle used to derive the rotation velocities (see Figure 2.6) and gas surface density. We derive a mean α_A value of 0.8, which is close to 1. This shows that the cloud growth criterion based on shear is better suited than the Toomre-Q criterion to explain the star formation observed in NGC 6822. Similar results have been found by Hunter et al. (1998) for a sample of dwarf irregulars.

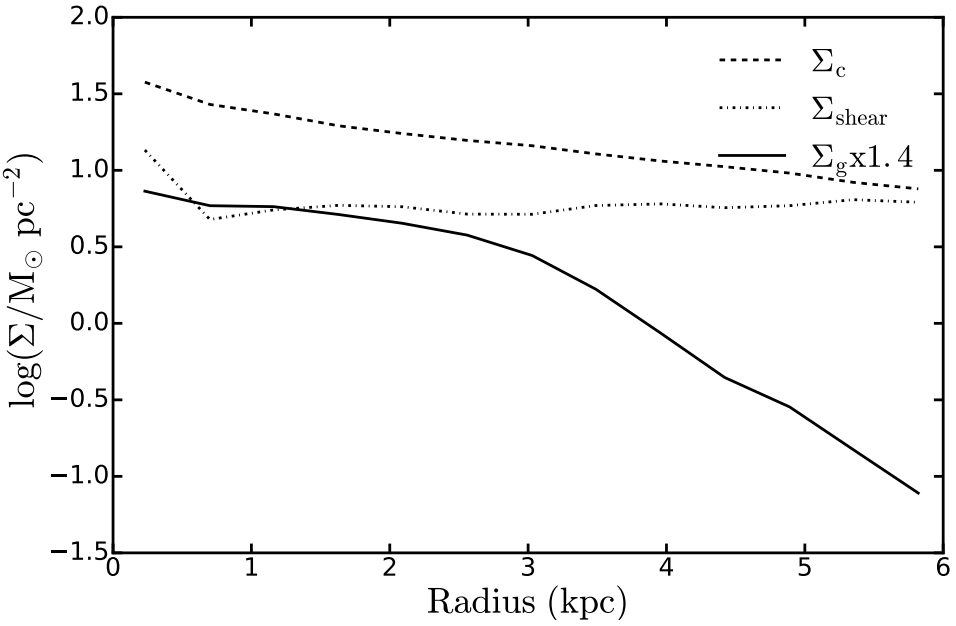

Figure 2.13: Comparsion of the radial distribution of the star formation threshold surface densities to the HI surface density. The full black line shows the gas surface density multiplied by a factor of 1.4 to correct for helium. The dashed line shows the critical density derived using the Kennicutt (1989) version. The dash-dotted line shows the shear critical density derived using the Hunter et al. (1998) version.

2.7 Summary

This study presents observations of the Local Group dwarf galaxy NGC 6822, performed with the KAT-7 radio interferometer in South Africa. The KAT-7 configuration ($\sim 3.5'$ spatial resolution and $T_{sys} \sim 26$ K) and the total observation time of $\sim$ 105 hrs on NGC 6822 allow us to detect the extended gas, reaching low column densities of $1{\times}10^{19}$ atoms cm^{-2}, which is an order of magnitude lower than the measured value for the ATCA observations. With the velocity resolution of 2.56 km s^{-1} for our observations, we find that:

1. A total HI mass of $1.3 \times 10^8 M_\odot$ is measured for NGC 6822 using the adopted distance of 0.48 Mpc. This HI mass, which is 23% larger than the value calculated using the ATCA observations, is surely a better estimate of the total HI mass of NGC 6822 as detected by the single dish Parkes observations. From the KAT-7 global profile, it is clear that the extra HI is extended over the entire galaxy. We have derived the mid-point velocity of -55 $\pm$ 2 km s^{-1}, which corresponds to the systemic velocity found by ROTCUR.

2. The rotation curve of NGC 6822 was derived from the velocity field map. We derive the V_{sys} = -55 km s^{-1}, mean P.A. = 118°, and mean i = 66°, with very lit-

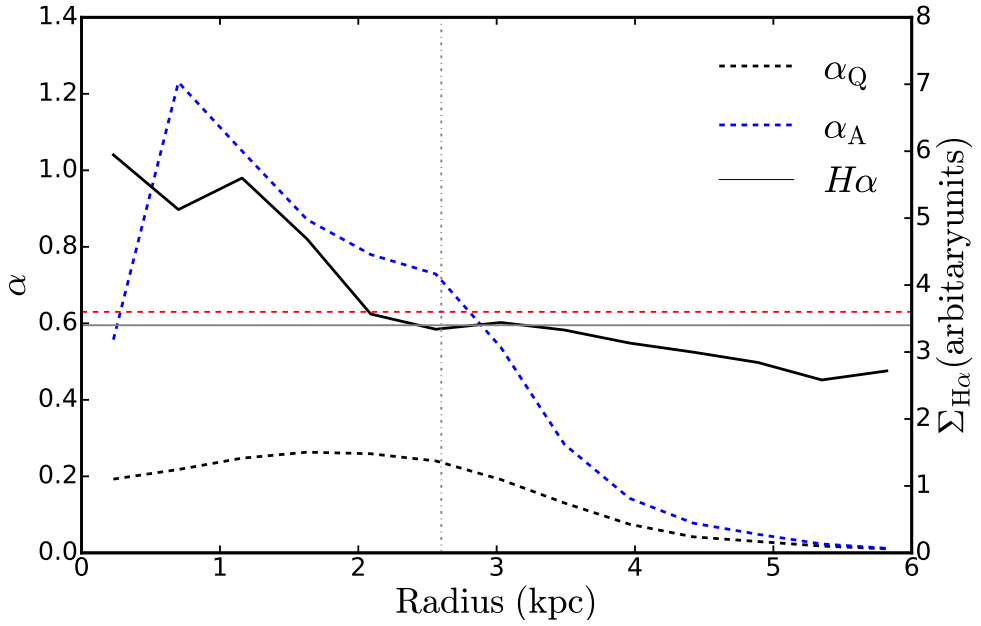

Figure 2.14: Radial variation in the ratio of the observed gas surface density to the critical densities derived from the Toomre-Q and cloud-growth criterion. The dashed black line shows α_Q while the dashed blue line shows α_A. Plotted for comparison in a black solid line are the Hα surface densities. The dashed red line shows the median value α = 0.63 from Kennicutt (1989) above which the gas density is high enough for large scale star formation. The grey solid line represents the Hα background noise. The grey dashed-dotted vertical line shows the extent of H_α.

tle difference between the approaching and receding sides. The KAT-7 RCs agree very well with the ATCA data. Although our derived kinematical parameters are in agreement with the values derived from the ATCA observations (V_{sys} = -54.4 km s^{-1}, mean P.A. ~ 118°, and mean i ~ 63°), the KAT-7 RC extends to ~ 1 kpc further out than the ATCA rotation curve.

3. The observationally motivated DM ISO model reproduces very well the observed RC while the NFW model gives a much poorer fit, especially in the inner parts. This confirms previous results that NGC 6822 has a cored and not a cuspy DM halo. Our derived best fit M/L, 0.12 ± 0.01, is consistent with the literature value of 0.10 ± 0.13. The small M/L ratio of NGC 6822 shows that the stellar distribution has no significant contribution to the total mass of the galaxy.

4. Using a fixed universal constant $a_0 = 1.21 \times 10^{-8}$ cm s^{-1}, the MOND model fits fail to reproduce the distribution of matter both in the inner and outer region of NGC 6822.

5. The cloud growth criterion produces a better explanation of star formation in

NGC 6822 than the Toomre-Q criterion. This shows that local shear rate could be a key player in cloud formation for irregular galaxies such as NGC 6822.

Begeman K. G., 1989, A&A, 223, 47

Begeman K. G., Broeils A. H., Sanders R. H., 1991, MNRAS, 249, 523

Bigiel F., Leroy A., Walter F., Brinks E., de Blok W. J. G., Madore B., Thornley M. D., 2008, AJ, 136, 2846

Brandenburg H. J., Skillman E. D., 1998, in American Astronomical Society Meeting Abstracts. p. 1354

Carignan C., Beaulieu S., 1989, ApJ, 347, 760

Carignan C., Purton C., 1998, ApJ, 506, 125

Carignan C., Frank B. S., Hess K. M., Lucero D. M., Randriamampandry T. H., Goedhart S., Passmoor S. S., 2013, AJ, 146, 48

Carignan C., Libert Y., Lucero D. M., Randriamampandry T. H., Jarrett T. H., Oosterloo T. A., Tollerud E. J., 2016, A&A, 587, L3

Côté S., Carignan C., Freeman K. C., 2000, AJ, 120, 3027

Famaey B., Binney J., 2005, MNRAS, 363, 603

Feast M. W., Whitelock P. A., Menzies J. W., Matsunaga N., 2012, MNRAS, 421, 2998

Ferguson A. M. N., Wyse R. F. G., Gallagher J. S., Hunter D. A., 1998, ApJ, 506, L19

Foley A. R., et al., 2016, MNRAS, 460, 1664

Gentile G., Salucci P., Klein U., Granato G. L., 2007, MNRAS, 375, 199

Gottesman S. T., Weliachew L., 1977, A&A, 61, 523

Hess K. M., Jarrett T. H., Carignan C., Passmoor S. S., Goedhart S., 2015, MNRAS, 452, 1617

Hess K. M., Cluver M. E., Yahya S., Leisman L., Serra P., Lucero D. M., Passmoor S. S., Carignan C., 2017, MNRAS, 464, 957

Huchtmeier W. K., Seiradakis J. H., Materne J., 1981, A&A, 102, 134

Hunter D. A., Elmegreen B. G., Baker A. L., 1998, ApJ, 493, 595

Hunter D. A., et al., 2012, AJ, 144, 134

Kennicutt Jr. R. C., 1989, ApJ, 344, 685

Kreckel K., Peebles P. J. E., van Gorkom J. H., van de Weygaert R., van der Hulst J. M., 2011, AJ, 141, 204

Lelli F., McGaugh S. S., Schombert J. M., 2016, AJ, 152, 157

Lucero D. M., Carignan C., Elson E. C., Randriamampandry T. H., Jarrett T. H., Oosterloo T. A., Heald G. H., 2015, MNRAS, 450, 3935

Martin C. L., Kennicutt Jr. R. C., 2001, ApJ, 555, 301

Mateo M. L., 1998, ARA&A, 36, 435

McMullin J. P., Waters B., Schiebel D., Young W., Golap K., 2007, in Shaw R. A., Hill F., Bell D. J., eds, Astronomical Society of the Pacific Conference Series Vol. 376, Astronomical Data Analysis Software and Systems XVI. p. 127

Milgrom M., 1983, ApJ, 270, 384

Milgrom M., 1988, ApJ, 333, 689

Navarro J. F., Frenk C. S., White S. D. M., 1997, ApJ, 490, 493

Oh S.-H., de Blok W. J. G., Walter F., Brinks E., Kennicutt Jr. R. C., 2008, AJ, 136, 2761

Oh S.-H., de Blok W. J. G., Brinks E., Walter F., Kennicutt Jr. R. C., 2011, AJ, 141, 193

Quirk W. J., 1972, ApJ, 176, L9

Rogstad D. H., Lockhart I. A., Wright M. C. H., 1974, ApJ, 193, 309

Schmidt P., Józsa G. I. G., Gentile G., Oh S.-H., Schuberth Y., Ben Bekhti N., Winkel B., Klein U., 2014, A&A, 561, A28

Skillman E. D., Bothun G. D., 1986, A&A, 165, 45

Skillman E. D., Terlevich R., Melnick J., 1989, MNRAS, 240, 563

Thilker D. A., et al., 2005, ApJ, 619, L79

Toomre A., 1964, ApJ, 139, 1217

Volders L. M. J. S., Högbom J. A., 1961, Bull. Astron. Inst. Netherlands, 15, 307

Weldrake D. T. F., de Blok W. J. G., Walter F., 2003, MNRAS, 340, 12

Wilcots E. M., Miller B. W., 1998, AJ, 116, 2363

de Blok W. J. G., Walter F., 2000, ApJ, 537, L95

de Blok W. J. G., Walter F., 2006a, AJ, 131, 343

de Blok W. J. G., Walter F., 2006b, AJ, 131, 363

de Blok W. J. G., Walter F., Brinks E., Trachternach C., Oh S.-H., Kennicutt Jr. R. C., 2008, AJ, 136, 2648

de Vaucouleurs G., 1991, Science, 254, 1667

van der Hulst J. M., Terlouw J. P., Begeman K. G., Zwitser W., Roelfsema P. R., 1992, in Worrall D. M., Biemesderfer C., Barnes J., eds, Astronomical Society of the Pacific Conference Series Vol. 25, Astronomical Data Analysis Software and Systems I. p. 131

CHAPTER 3

HI OBSERVATIONS OF SEXTANS A AND B WITH THE SKA PATHFINDER KAT-7

HI observations of the Local Group dwarf irregular galaxies Sextans A and B, obtained with the Karoo Array Telescope (KAT-7) are presented. The KAT-7 wide field of view and excellent surface brightness sensitivity allows us to verify the HI extent of the galaxies down to column density sensitivity of $\sim 10^{18}$ cm^{-2}. We derive HI extents of $30'$ and $20'$ and total HI fluxes of 181 $\pm$ 2.0 Jy km s^{-1} and 105 $\pm$ 1.4 Jy km s^{-1} for Sextans A and B respectively. This result shows clearly the overestimate of the HI extent and total HI flux of $54'$ and 264 Jy km s^{-1} reported for Sextans A using the Effelsberg observations. Tilted ring models allow us to derive the rotation curves (RCs) of Sextans A and B out to $9.8'$ ($\sim$ 3.5 kpc) and $10.8'$ ($\sim$ 4 kpc) respectively. The RCs of the two galaxies are seen to decline in the outer parts. The dark matter distribution in Sextans A is better described by the pseudo-isothermal halo model when a M/L ratio of 0.2 is used. For Sextans B, the mass model fits are not as good but again an isothermal sphere with an M/L of 0.2 represents best the data. Using the MOdified Newtonian Dynamics (MOND), better fits are obtained when the constant a_0 is allowed to vary. The critical densities for gravitational instabilities are calculated using the Toomre-Q and cloud-growth based on shear criterion. We find that in regions of star formation, the cloud growth criterion based on shear explains better the star formation in both Sextans A and B.

3.1 Introduction

The neutral hydrogen (HI) component of the interstellar medium (ISM) is an ideal tracer of the kinematics of disk galaxies. The ISM in nearby dwarf galaxies are the closest analog to conditions which prevailed in the early universe due to their low

metallicity and high gas content. Numerous previous observations of dIrrs showed extremely large HI disks several times larger than their optical cores (e.g., Huchtmeier et al., 1981; Meurer et al., 1996; Wilcots & Miller, 1998; Gentile et al., 2007; Kreckel et al., 2011; Hunter et al., 2011; Schmidt et al., 2014; Namumba et al., 2017). Such extended HI disks allow us to probe very far out into the dark halo potential and derive the large-scale kinematics of these galaxies (e.g., Carignan & Purton, 1998).

Most interferometric studies of HI gas in dwarf galaxies lack the required sensitivity to detect large scale extended HI emission (e.g. Skillman & Bothun (1986); Côté et al. (2000); de Blok & Walter (2000); Kreckel et al. (2011); Hunter et al. (2012)). We would ideally probe the extended HI gas using single dish telescopes as these instruments do not filter out any emission (Pisano, 2014). However, single dish telescopes do not have the required spatial resolution to derive the kinematics of the gas. Our best alternative is to use an interferometer with short baselines that has better spatial resolution and is sensitive to large scale structures.

As we prepare for the Square Kilometer Array (SKA) in the near future, SKA pathfinders are being built for engineering tests and early science. Among the telescopes being built for the SKA early science is Meer Karoo Array Telescope (MeerKAT. One of the main aims of MeerKAT is to detect low column density gas in nearby galaxies using high resolution and achieving column density sensitivity of $\leqslant 10^{18}$ cm^{-2}. As MeerKAT is still being built, the KAT-7, initially built as an engineering test-bed for MeerKAT has been able to produce new exciting early SKA science. The KAT-7 compact configuration of its seven 12m dishes, combined with the low $T_{sys} \sim 26$ K have been able to detect, when present, low column density gas in many nearby galaxies that could not be detected by other synthesis arrays such as the Very Large Array (VLA) or Australian Telescope Compact Array (ATCA).

KAT-7 observations of the Magellanic-type spiral NGC 3109 (Carignan et al., 2013) detected 40% more HI mass than what was detected with the VLA observations. This allowed the measurement of the RC of NGC 3109 out to 32′, doubling the angular extent of existing measurements. Lucero et al. (2015) detected 33% more flux for NGC 253 than what was previously detected with the VLA, giving new results on the kinematics of the low column density gas in NGC 253. KAT-7 polarized radio continuum and spectral line observations of M83 revealed massive HI gas distribution that appears to be tightly coupled with interaction of the galaxy and the enviroment (Heald et al., 2016). These observations detected more flux than the VLA observations and allowed the rotation curve to be measured out to 50 kpc. The recently published KAT-7 observations of the nearby dwarf irregular galaxy NGC 6822 (Namumba et al., 2017) revealed 23% more HI mass than the previous ATCA

observations.

The discrepancy between the single dish (Effelsberg and Green Bank Telescope (GBT)) data on the true HI extent of Sextans A (Huchtmeier et al., 1981; Hunter et al., 2011) and the interferometric data from the Very Large Array (VLA) (Skillman et al., 1988; Wilcots & Hunter, 2002) has motivated us to map Sextans A and B in HI using the KAT-7. KAT-7 is ideally suited for this project due to its short baselines and low receiver temperature which makes it sensitive to large scale, low surface brightness emission.

The structure of the paper is as follows. Brief descriptions of Sextans A and B are given in Section 3.2, followed by the observations and data reduction in Section 3.3. In Section 3.4, we present the results on the HI distribution. The rotation curve results derived from the tilted ring fit are presented in Section 3.5, and the dark matter mass models of the galaxies are explained in Section 3.6. In Section 3.7, we explore instability models for the onset of star formation in Sextans A and B and in Section 3.8 we summarize our work.

3.2 Sextans A and Sextans B

Sextans A (DDO 75, UGC 205) is a dIrr galaxy at a distance of 1.3 Mpc (de Vaucouleurs et al., 1991a), which places it in the Local Group of galaxies, lying between Sextans B and NGC 3109. Sextans A is classified as an IBm galaxy (de Vaucouleurs et al., 1991a), having an absolute magnitude of $M_V \sim$ -14 (Kniazev et al., 2005). The stellar distribution in Sextans A has been observed to have a square shape (Hunter & Plummer, 1996). Its optical angular diameter is $D_0 = 4'.8$ (de Vaucouleurs et al., 1991a).

Huchtmeier et al. (1981) first mapped the HI distribution around Sextans A using the Effelsberg 100m single dish telescope. Their results yielded a large HI extent of $54'$, which is 5.8 times the galaxy optically-defined Holmberg diameter, and a total HI mass of 1.6×10^8 $M_\odot$. The first interferometric observations of Sextans A were done by Skillman et al. (1988) using the VLA. They were able to detect only about 50% of the total HI flux reported by Huchtmeier et al. (1981) and measured an HI extent of $9.4'$. Skillman et al. (1988) suggested that the 50% missing gas could exists in large scale low column density gas unable to be detected by the VLA due to the lack of short baselines and limited field of view. Wilcots & Hunter (2002) mapped Sextans A using a VLA mosaic that allowed them to sample a much larger field of view than Skillman et al. (1988). They were able to recover only 62% of the flux reported by Huchtmeier et al. (1981) with an HI extent of $18'$. Comparing their VLA HI maps from the peaks in the profiles at each position with data from the HI Parkes

All-Sky Survey (HIPASS) observations confirmed the fact that there was a good deal of HI gas missing from the VLA mosaic due to the short spacings problem.

To verify the existence of the gas at the outer edges of Sextans A and explore how far it extends, Hunter et al. (2011) observed Sextans A with the Green Bank 100m single dish telescope (GBT). Their observations detected 25% more flux compared to Wilcots & Hunter (2002), but only 78% of the flux detected by (Huchtmeier et al., 1981). They measured an HI extent of $22.1'$. They outlined significant differences between the GBT and the Effelsberg observations that may contribute to the difference in the observed HI extent. One difference was that the signal to noise of the GBT observations was higher, and the extended features in the Huchtmeier et al. (1981) occured at low signal to noise. The other difference was that the GBT has a clear point spread function out to several degrees from the main beam while the Effelsberg telescope has significant sidelobes. This lead them to believe that the Effelsberg map had Galactic emission entering from the sidelobes, which resulted in an overestimate of both the extent and the total flux.

Sextans B (DD0 70, UGC 5373) is classified as an IBm galaxy at a distance of 1.3 Mpc (de Vaucouleurs et al., 1991a). It is a faint galaxy with an absolute magnitude of $M_V \sim$ -14 (Kniazev et al., 2005). As far as global properties are concerned, Sextans B is considered to be a twin of Sextans A, except for the profile width, due to different inclinations. Huchtmeier et al. (1981) first mapped the HI of Sextans B using the Effelsberg single dish telescope. They were able to derive an HI extent of $13'$, which is 1.7 times the Holmberg diameter, and a total HI mass of $1.3\times10^8 M_\odot$. VLA study of the neutral hydrogen in Sextans B (Worth & Wilcots, 2009) showed that the HI kinematics of this galaxy are similar to those of other dwarfs. They found that the rotation curve of Sextans B was flat out to a radius of $250''$, which is about 1.6 kpc. Several distinct HI holes have also been identified in Sextans B. Oh et al. (2015) derived the rotation curve of Sextans B out to a radius of $\sim$ 3 kpc using the VLA Local Irregulars That Trace Luminosity Extremes, The HI Nearby Galaxy Survey (LITTLE THINGS) (Hunter et al., 2012). The basic parameters of Sextans A and B are given in Table 3.1.

3.3 KAT-7 observations and data reduction

The observations were obtained with the compact, seven-dish KAT-7 telescope (Foley et al., 2016), located close to the South African SKA core site in the Northern Cape Karoo desert region. The parameters of the KAT-7 observations are given in Table 3.2.

The data were collected between 2014 December and 2015 July. Sextans A was

Table 3.1: Basic properties of Sextans A and B.

Parameter	Sextans A	Sextans B
Morphology	IBm[a]	IBm[a]
Right ascension (J2000)	10:11:01.3[a]	09:59:59.9[a]
Declination (J2000)	-04:42:48.0[a]	05:19:57[a]
Distance (Mpc)	1.3[a]	1.3[a]
M_B (Mag)	-13.9[d]	-13.9[d]
$V_{heliocentric}$ (km s^{-1})	324[a]	301[a]
Optical PA(∘)	41.0[e]	88.0[e]
Optical inclination_opt(∘)	33.5[e]	57.8[e]
Total HI mass ($M_\odot$)	$(7.3 \pm 0.07) \times 10^7$	$(4.2 \pm 0.06) \times 10^7$

Notes. Ref (a) de Vaucouleurs et al. (1991a); (b) Dolphin et al. (2003); (c) Karachentsev et al. (2002); (d) Kniazev et al. (2005); (e) Hunter et al. (2012)

observed over 19 observing sessions for a total of 60 hours on source while Sextans B was observed for 17 sessions for a total of 51 hours on source. The HI observations were carried out using the c16n25M4K spectral line mode. This correlator mode gives a total bandwidth of 12.5 MHz and 4096 channels of 0.64 km s^{-1} width. The central frequencies of our observations were 1418.9 MHz for Sextans A and 1419.0 MHz for Sextans B. All the data were hanning smoothed to 1.28 km s^{-1} before calibration. The observations were done using a 5, 6 or 7 antenna configuration depending on the availability of the antennas.

All the data were reduced using the standard calibration tasks in the Common Astronomy Software Application CASA 3.4.0 package (McMullin et al., 2007). Calibration was performed separately for each observing session. Flagging of bad data due to radio frequency interferences (RFI) and antenna malfunctions were done using the CASA task FLAGDATA. The corrections for the flux/bandpass shape were determined using the calibrator 0407+658. The time-varying phases and antenna gains were calibrated based on observations of the phase calibrator 0942-080. The calibration solutions were applied to the targets and the target sources were then split from the calibration sources using the task SPLIT. The individual calibrated data sets were then combined together using the CASA task CONCAT. The combined data were continuum subtracted by using a first order polynomial in the task UVCONTSUB. Doppler corrections were performed on the data to ensure that proper velocity coordinates were used (Carignan et al., 2013). At this point, visibilities satisfying the condition $|u| \leqslant 10\lambda$ were removed from the data set to avoid the low level RFI that are correlated when the fringe rate is equal to zero (Lucero et al., 2015; Hess et al., 2017).

The data were Fourier transformed using the CASA task CLEAN. Firstly, dirty cubes were imaged and the rms noise in line free channels was measured. For both Sextans A and B, the noise level in line free channels was found to be ~ 1.5 times the theoretical noise, see Table 3.2. Using a flux threshold of 1 times the typical r.m.s of the flux in a line free channel, the data were cleaned in a non-interactive mode using

a clearly defined mask. For each galaxy, two cubes were produced by applying the natural (na) and robust 0 weighting to the uv data. Taking into account the spatial resolution of KAT-7, we have decided to use the robust 0 cubes for our analysis.

3.3.1 Deriving HI maps

For each galaxy, the data cube was smoothed to 2 times the original spatial resolution. Noise pixels were removed from the smoothed cubes by excluding pixels $\leqslant 2\sigma$, where σ is the noise in line free channels. The remaining noise pixels were removed by creating masks around the galaxy emission in each channel. The final mask from the smoothed cube was then applied to the full resolutions cubes. The integrated HI maps were created by adding together all clipped channels with emission using a primary beam corrected cubes. The maps were converted to column density by using the following formula:

$$N_{\rm HI}\ (cm^{-2}) = \frac{1.835 \times 10^{18} \times 6.07 \times 10^{5} \times \int S_v dv}{\theta_{major} \times \theta_{minor}} \tag{3.1}$$

where dv is the velocity resolution in km s^{-1}, S$_v$ is the flux in Jy/beam , θ_{major} is the major axis and θ_{minor} is the minor axis of the beam in arcsecs. The values of these parameters are given in Table 3.2.

To construct the velocity field maps, two methods were considered. The most popular one being the intensity weighted mean (IWM). However, this method is known to produce uncertainties in deriving velocities when the S/N is low (de Blok et al., 2008) as in our case for Sextans A. An alternative, in this case, was to construct the velocity field maps by fitting Gaussians to each profile. This method has already been implemented successfully by various authors (see e.g. Carignan et al., 1990) and has proven to give a better result compared to the IWM.

We fitted a single Gaussian to each HI cube line profile to generate the velocity field maps. This was done using the GIPSY task XGAUFIT. We used the data sets without primary beam correction in order to retain the original properties of the data when performing profile fitting. To ensure high quality velocity field maps, three filters were used: 1) only profiles with fitted fluxes maxima higher than 3σ were retained, 2) profiles with a fitted line width less than the velocity resolution of the data were excluded, and 3) fitted profiles had to be within the velocity range of the data. The dispersion maps were produced using the AIPS task MOMNT. The final velocity and dispersion maps were masked using the amplitude map from XGAUFIT. The final velocity field and dispersion maps are shown Figure 3.8(a,b) and 3.12(a,b) for Sextans A and B respectively.

Table 3.2: Parameters of the KAT-7 observations.

Parameter	Sextans A & B
Start of observations	December 2014
End of observations	June 2015
Total integration	60 & 51 hours
FWHM of primary beam	1.27°
Total bandwidth	12.5 MHz
Final channel width (2 × 0.64 km s^{-1})	1.28 km s^{-1}
Final number of channels (4096/2)	2048
Map gridding	30″ by 30″
Map size	256 by 256
Flux/bandpass calibrator	0407+658
Phase calibrator	0941-080
Robust = 0 weighting function	
FWHM of synthesized beam	228″× 201″ & 261″× 191″
RMS noise	4.5 & 5.0 mJy/beam
Column density limit	
(3σ over 16 km s^{-1})	5.8×10^{18} cm^{-2} & 5.4×10^{18}cm^{-2}

3.4 HI distribution

3.4.1 Sextans A

The global HI profile of Sextans A is given in Figure 3.1. Plotted for comparison is the HI global profile from the VLA LITTLE THINGS data (Hunter et al., 2012). The mid-point velocity at the 50% level is 324 ± 2 km s^{-1}, identical to the previous measurements Huchtmeier et al. (1981); Wilcots & Hunter (2002); Barnes & de Blok (2004); Hunter et al. (2011). The 50% line width is ΔV = 45 ± 2 km s^{-1}. This is close to the value of ΔV = 46 km s^{-1} derived by Barnes & de Blok (2004) but smaller than the value of ΔV = 55 km s^{-1} derived by Wilcots & Hunter (2002). An integrated flux of 181 ± 2 Jy km s^{-1} was measured, yielding a total HI mass of (7.3 ± 0.07) ×10^7 M$_\odot$ at the adopted distance of 1.3 Mpc. This is similar to the Parkes single dish results of Barnes & de Blok (2004) and in agreement within the error to their HI mass of 6.7 ± 0.5 ×10^7 M$_\odot$. The GBT single dish observations (Hunter et al., 2011) reported an HI mass of 8.2×10^7 M$_\odot$, which is 11% more compared to our derived HI mass. The GBT observations report ∼ 10% uncertainty on the flux due to calibration. Taking this into account brings the KAT-7 derived mass in agreement with the GBT calculated mass. This implies that KAT-7 does not miss any galaxy flux. The KAT-7 derived HI mass is 5% more than the mass of 6.9 ×10^{7}M$_\odot$ detected by the VLA mosaic observations (Wilcots & Hunter, 2002) and in excellent agreement with the HI mass of 7.1 ×10^7 M$_\odot$ (Hunter et al., 2012).

Figure 3.2 shows the integrated column density map of Sextans A superposed on the DSS image. The HI distribution is well resolved by the KAT-7 beam. The 3σ column density limit in Figure 3.2 is 5.8×10^{18} cm^{-2}. This is higher than the 3σ limit of 2 ×10^{18} cm^{-2} of Hunter et al. (2011) and lower than the 7.5×10^{18} cm^{-2} of Wilcots & Hunter (2002). At the 3σ column density level, we measure an HI diameter of 30′. Comparing with the literature, we measure an HI diameter of 23′ at 10^{19} cm^{-2}

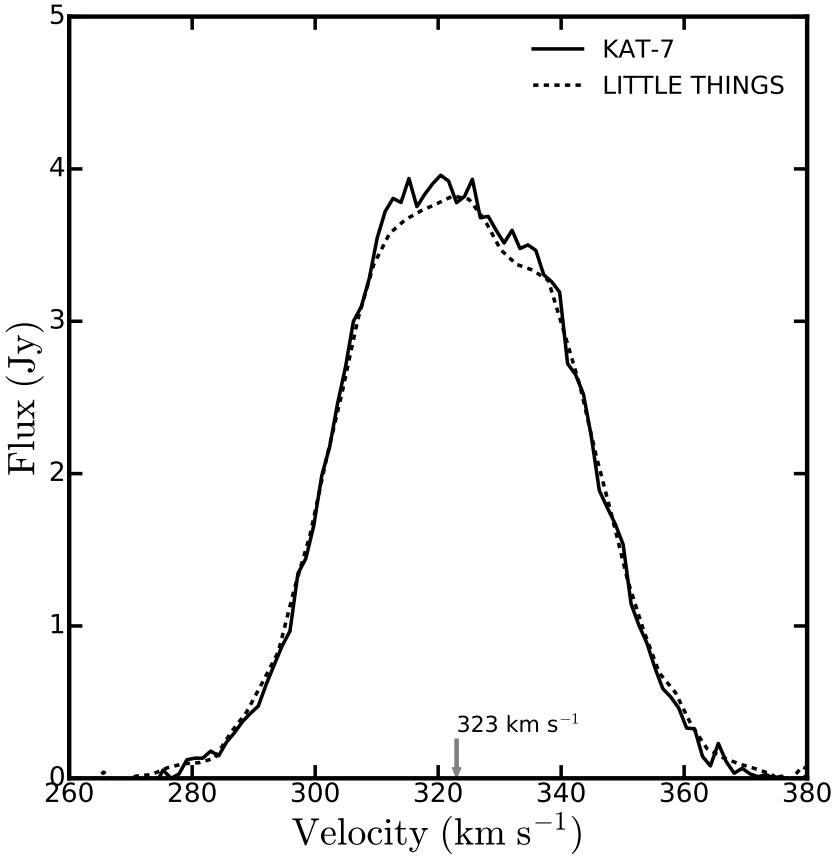

Figure 3.1: Global HI line profile of Sextans A from the KAT-7 primary beam corrected data cube, (black solid line) in comparison to the VLA LITTLE THINGS HI (Hunter et al., 2012) global profile, (black dash-dotted line). The mid-point velocity of 323 km s^{-1} is indicated.

similar to an HI diameter of 22′ of Hunter et al. (2011).

Figure 3.3 shows the azimuthally averaged KAT-7 radial HI density profile of Sextans A. Plotted for comparison is the HI radial profile from the VLA observations of Hunter et al. (2012). Both profiles were derived using the GIPSY task ELLINT by applying the tilted ring kinematics parameters described in Section 3.5. It can be seen that the large beam of KAT-7 has averaged out the depression and peak in the center.

3.4.2 Sextans B

The global HI spectrum of Sextans B is given in Figure 3.4. This is compared to the LITTLE THINGS derived global profile. The mid-point velocity at 50% level is 301

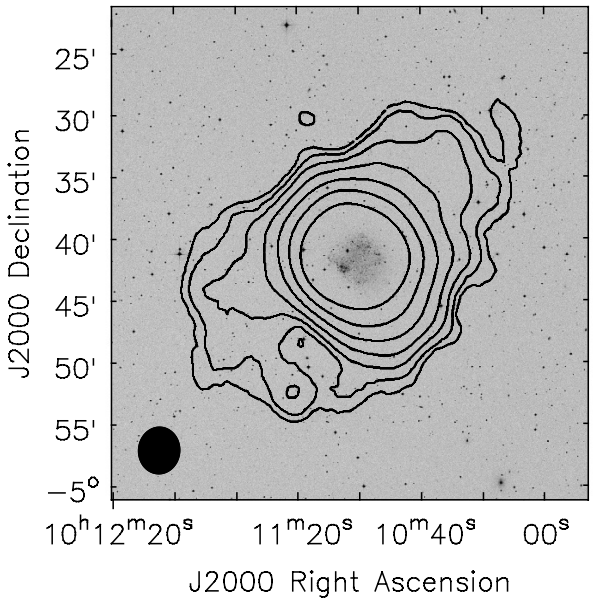

Figure 3.2: Integrated HI column density map of Sextans A superposed on a DSS image. The contours are 5.8, 11.6, 23.2, 46.4, 92.8, 185.0, and 370 × 10^{18} cm^{-2}. The synthesized beam is shown in the bottom left corner.

± 1.4 Jy km s^{-1}. The 50% line width is ΔV = 40.8 ± 1.84 km s^{-1}. An integrated flux of 105± 1.4 Jy km s^{-1} is measured, giving a total HI mass of 4.2 ×10^7 M$_\odot$. Using the same distance, the KAT-7 observations measure ~ 15% more HI mass than the VLA-ANGST (Ott et al., 2012) and is in agreement with the value of 3.9 ×10^7 M$_\odot$ derived from the VLA LITTLE THINGS (Hunter et al., 2012).

Figure 3.5 shows the HI column density map of Sextans B superposed on a DSS optical image. The HI distribution is well resolved by the KAT-7 beam. The lowest contour is 5.4 ×10^{18} cm^2, which corresponds to the 3σ limit calculated over 16 km s^{-1}. At the lowest contour, the HI diameter is 20′. The azimuthally averaged HI densities of Sextans B are shown in Figure 3.6. This is plotted together with the derived HI profile from the LITTLE THINGS data (Hunter et al., 2012). Again, the beam smearing in the KAT-7 data has reduced the peak seen at high resolution.

3.4.3 General remark on the HI distribution

It can be seen in Figure 3.1 and 3.4 that KAT-7 recovered a small fraction of flux missing from the VLA observations because of the lack of short spacings. However, the price to pay for having a lower spatial resolution is to wash out the high brightness features in the center, as can be seen in Figure 3.3 and 3.6. What is clear however is that the KAT-7 observations dismiss completely the large extents and fluxes

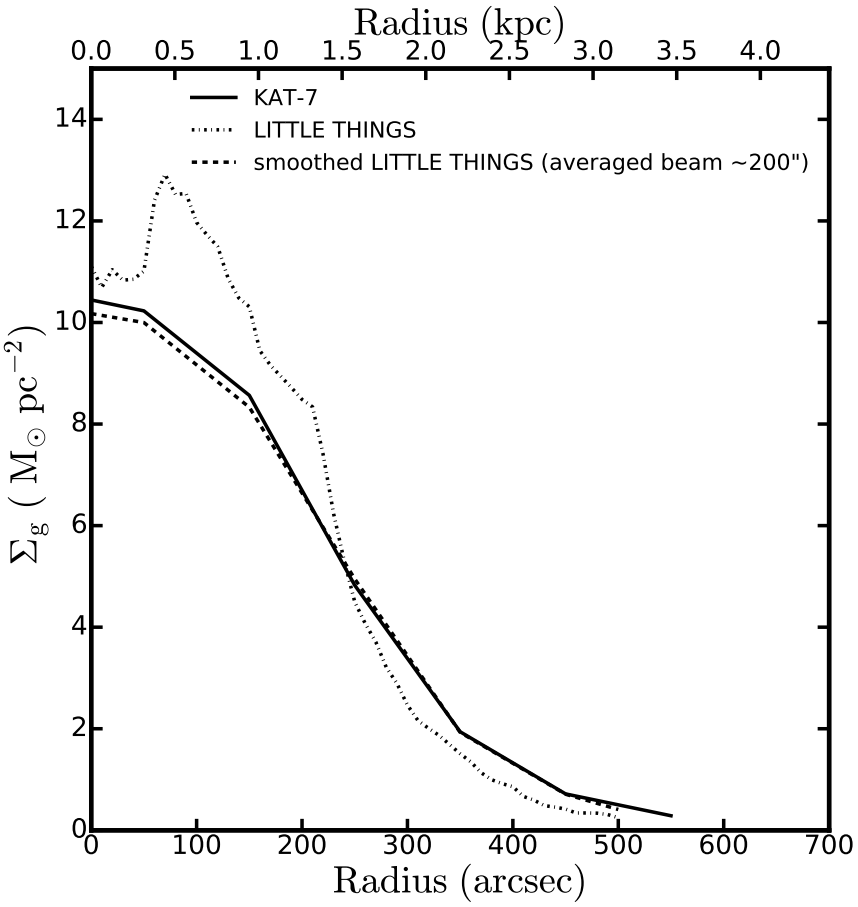

Figure 3.3: KAT-7 HI radial profile of Sextans A (black solid line) compared to the VLA LITTLE THINGS (Hunter et al., 2012). The dashed line shows the LITTLE THINGS radial profile smoothed to the KAT-7 spatial resolution while the dash-dotted lines shows LITTLE THINGS radial profile at VLA full spatial resolution. The surface densities are multiplied by a factor 1.4 to take into account helium and other elements.

derived for Sextans A from the Effelsberg observations. The KAT-7 total fluxes and HI extents are much closer to the ones derived using the GBT or the VLA (see Table 3.3).

3.5 HI kinematics

3.5.1 Tilted ring model

We fit a tilted-ring model to the velocity fields using ROTCUR in GIPSY (Begeman, 1989) to derive the parameters that best describe the observed velocity fields.

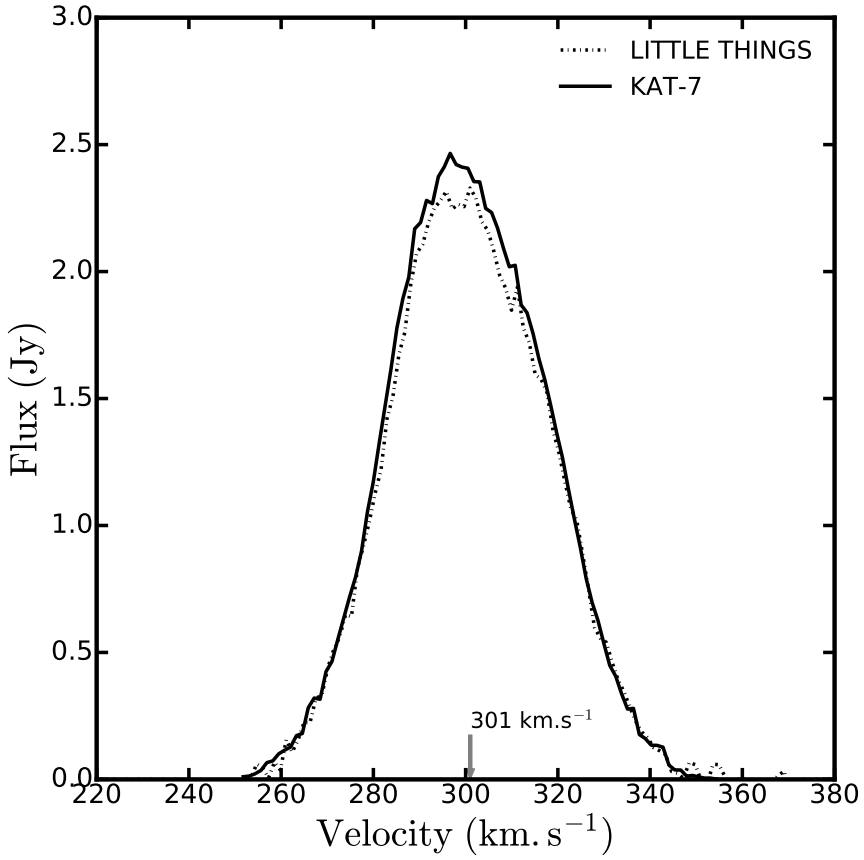

Figure 3.4: Global HI line profile of Sextans B from the KAT-7 primary beam corrected data cube (black solid line) compared to the VLA LITTLE THINGS HI (Hunter et al., 2012) global profile (black dash-dot line). The mid-point velocity of 301 km s^{-1} is indicated.

Table 3.3: Comparison of the HI fluxes and extents of Sextans A and B.

	Integrated flux (Jy km s^{-1})			
Galaxy	KAT-7[a]	Effelsberg[b]	GBT[c]	VLA[d]
Sextans A	181 ± 2.0	264	206± 20.6	178 ± 2.0
Sextans B	105 ± 1.4	116	....	98 ± 1.2
	HI extent ($'$) at 10^{19} atoms.cm^{-2}			
Sextans A	23.0	54.0	22.1	22.0
Sextans B	14.2	13.0	....	12.8

Notes. Ref (a) This work; (b) Huchtmeier et al. (1981); (c) Hunter et al. (2011); (d) Hunter et al. (2012)

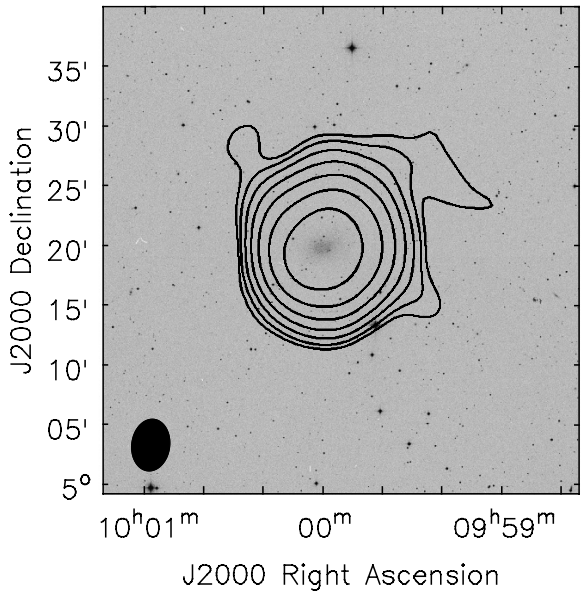

Figure 3.5: Integrated HI column density map of Sextans B superposed on a DSS image. The contours are 5.4, 10.8, 21.6, 43.2, 86.4, 172.8, and 345.6 × 10^{18} cm^{-2}. The synthesized beam is shown in the bottom left corner.

3.5.2 Deriving the rotation curve

Following Namumba et al. (2017) we derive the rotation curves of Sextans A and B using a spacing and width of 100″. The errors on V_{rot} were derived using Equation 3.2 (Carignan et al., 2013).

$$\Delta V = \sqrt{\sigma^2(V) + (\frac{|V_{app} - V_{rec}|}{2})^2} \tag{3.2}$$

We correct the rotational velocities for the asymmetric drift as the dynamical support by random motions of the gas disk is significant. Following the method described in Côté et al. (2000), we correct for the asymmetric drift as follows:

$$V_c^2 = V_{\rm rot}^2 - 2\sigma\frac{\delta\sigma}{\delta \ln R} - \sigma^2\frac{\delta \ln \Sigma}{\delta \ln R} \tag{3.3}$$

where V_c is the corrected velocity, $V_{\rm rot}$ is the observed one, σ is the velocity dispersion and Σ is the gas density. The asymmetric drift corrected velocities of Sextans A and B are shown in Table 3.4 and Table 3.5 respectively

3.5.3 Sextans A rotation curve results

Results of the tilted ring model fitted to the first order gaussian velocity field for Sextans A are presented in Figure 3.7 and 3.8. The first and second panel of Figure

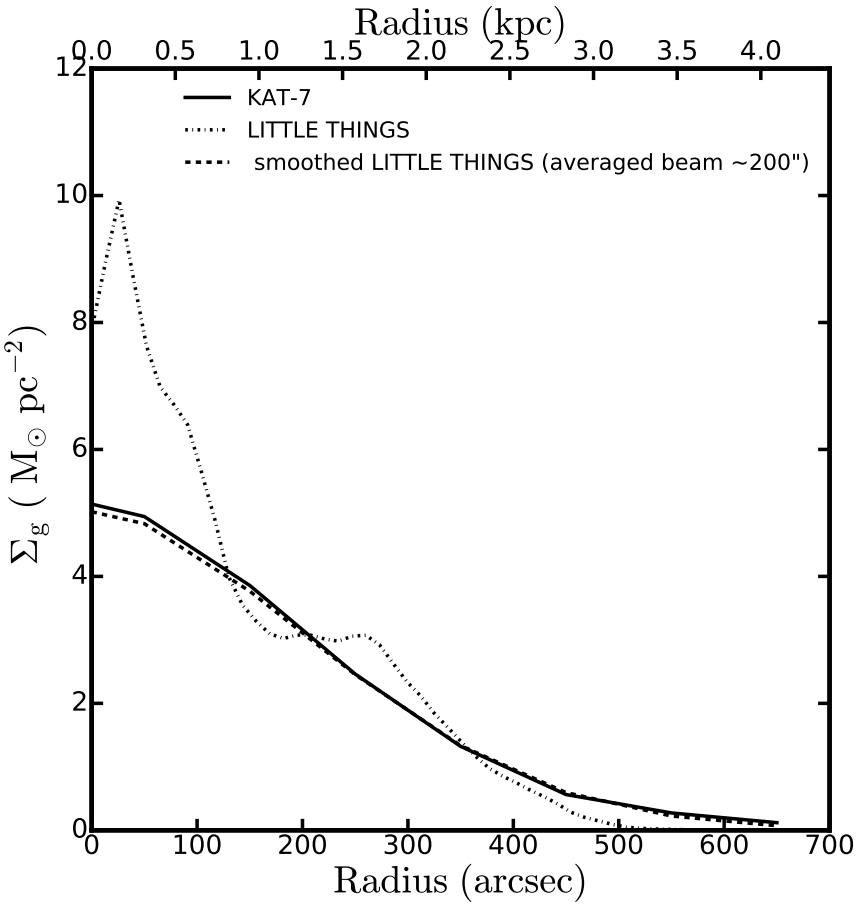

Figure 3.6: KAT-7 HI radial profile of Sextans B (black solid line) compared to the VLA LITTLE THINGS (Hunter et al., 2012). The dashed line shows the LITTLE THINGS radial profile smoothed to the KAT-7 spatial resolution while the dash-dotted lines shows LITTLE THINGS radial profile at VLA full spatial resolution. The surface densities are multiplied by a factor 1.4 to take into account helium and other elements.

3.7 shows the behavior of the inclination and position angle when the parameters are left free to vary while the green solid lines show the fitted parameters used to derive the final rotation curves for the approaching, receding, and both sides, shown in the third panel of Figure 3.7. We derive the rotation curve out to 550″, which is ~ 3.5 kpc. The rotation curve rises as $V_{rot}(r) \propto r$ out to ~ 250″. Beyond this radius, the rotation curve is seen to decline down to 550″. This feature in the RC is not peculiar to dwarf galaxies such as Sextans A. The analysis of the rotation curve of GR 8 (Carignan et al., 1990) showed that the RC of the galaxy was declining in the outer regions (see also e.g. the case of the late-type spiral NGC 7793: Dicaire et al. (2008)). A systemic velocity of V_{sys} = 324 ± 0.6 km s^{-1} is found, similar to the value obtained from the global profile. A mean i and $P.A.$ of 34° and 86° are measured respectively.

Table 3.4: Radial variation of the HI surface densities Σ_g, the gas velocity dispersions σ, the observed rotation velocities V_0, the errors of the observed velocities ΔV, and the asymmetric drift corrected rotation velocities V_c for the KAT-7 data of Sextans A.

Radius arcsec	Σ_g $M_\odot pc^{-2}$	σ km s^{-1}	V_{rot} km s^{-1}	Δ V km s^{-1}	V_c km s^{-1}
0.0	7.4	14.1	0.0	0.0	0.0
50	7.3	14.0	13.2	2.9	13.0
150	6.1	12.5	24.8	2.8	26.4
250	3.4	11.3	28.9	1.4	33.2
350	1.4	10.9	28.1	2.9	35.3
450	0.5	10.5	22.9	5.3	32.9
550	0.2	9.9	22.2	4.8	31.8

Notes. Column (1) gives the radius, column (2) the surface densities, column (3) the velocity dispersion, column(4) the observed rotation velocities, column (5) the errors of those velocities, and column (6) the corrected velocities used for the mass models.

Figure 3.8 compares the observed velocity field (a) to the derived model velocity field (c), while (d) shows the residual map (observed velocity field - model velocity field). (b) shows the velocity dispersion map. The velocity dispersions are not corrected for beam smearing. We see no systemic large scale residuals, with most of them less than 5 km s^{-1}. Only a few residuals $\sim$ 10 km s^{-1} are seen in the low S/N outer parts. Figure 3.9 shows the comparison between our KAT-7 rotation curve and the VLA LITTLE THINGS curve (full resolution and smoothed to KAT-7 spatial resolution)(Hunter et al., 2012). The rotation curves are in agreement within errors. Figure 3.10 shows the rotation curve overlaid on a position-velocity (PV) diagram obtained along the major axis. The rotation curve shows a good representation of the dynamics of the galaxy.

3.5.4 Sextans B rotation curve results

The results of the tilted ring model fitting for Sextans B are shown in Figure 3.11 and 3.12. A constant inclination and a varying P.A. were used to derive the final rotation curve. A constant inclination was chosen as the variation of the inclination with radius was small. We measure the rotation curve out to 650″, which corresponds to $\sim$ 4 kpc. The rotation curve is seen to be rising out to $\sim$ 550″, with the last point showing a decline. However, the decline may be due to the fact that we keep the inclination constant. A smaller inclination for the last 2 points would probably keep the RC flat. A declining RC of Sextans B has been reported by Oh et al. (2015). A mean systemic velocity, V_{sys} of 302 $\pm$ 0.9 km s^{-1} is found, similar to the value derived from the global profile. We find a mean i and $P.A.$ of 49° and 56.6° respectively, values consistent with the literature Oh et al. (2015).

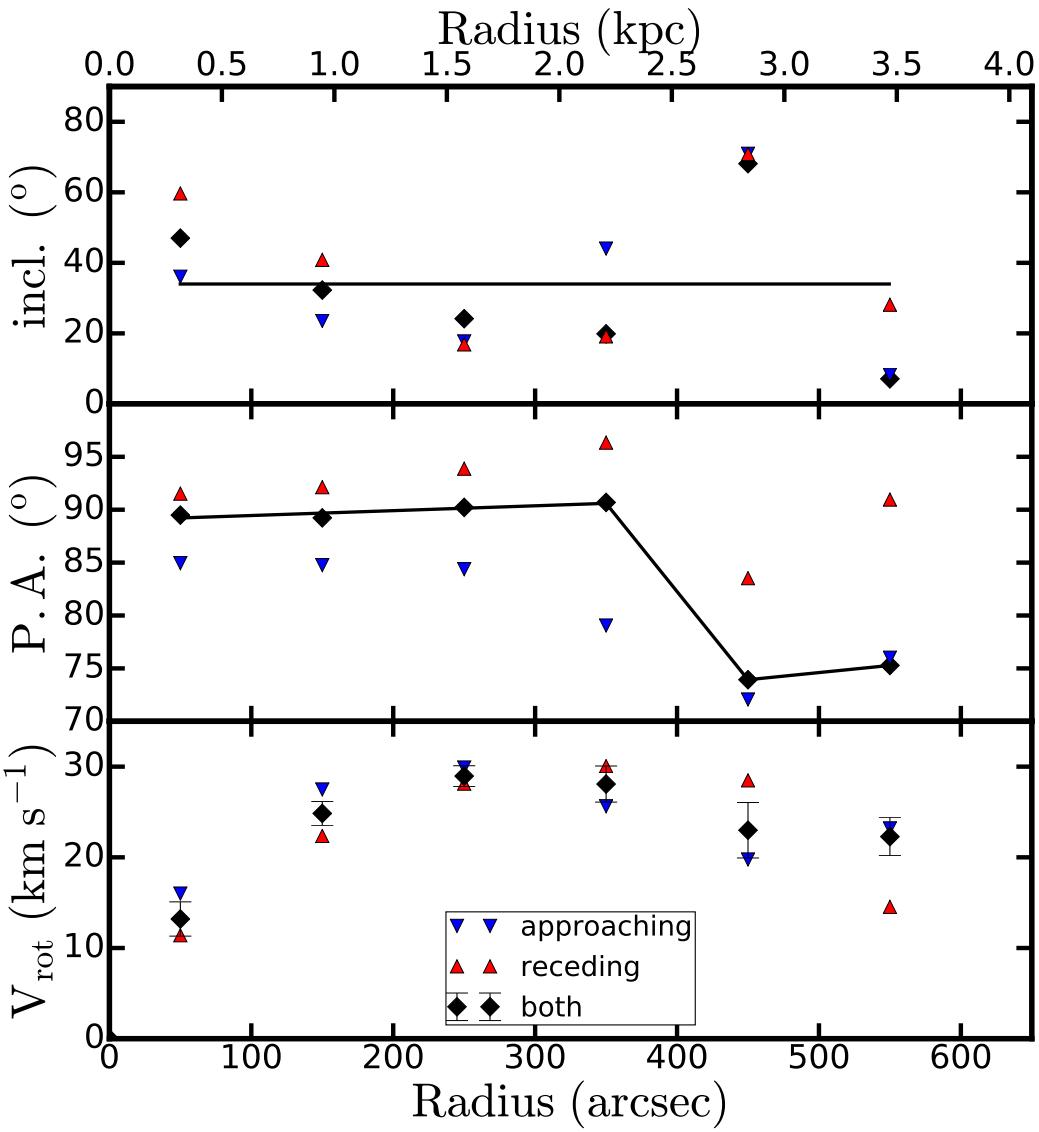

Figure 3.7: Results of the tilted ring fits for Sextans A. For the middle and top panels, the blue and red triangles and the black diamonds show the behavior of the PA and inclination as free parameters while the black solid lines show the behavior of the PA and inclination fixed to the model used to derive the final rotation curve. In this case the PA is varying while the inclination is fixed to the mean value. For the bottom panel, the blue triangles represent the curve for the approaching side while the red triangles represents the curve for the receding side.

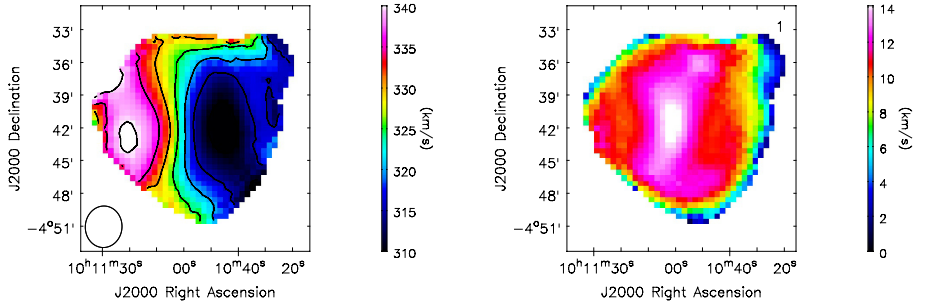

(a) Observed velocity field map

(b) Velocity dispersion map

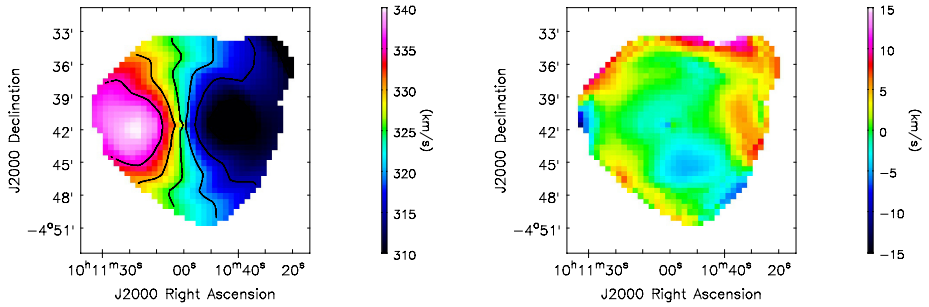

(c) Model velocity field map

(d) Residual velocity field map

Figure 3.8: Maps of Sextans A: Observed velocity field map (a), velocity dispersion map (b), model velocity field (c), and residual map (d). The observed and model velocity field contours run from 310 to 340 km s^{-1} in steps of 5 km s^{-1}.

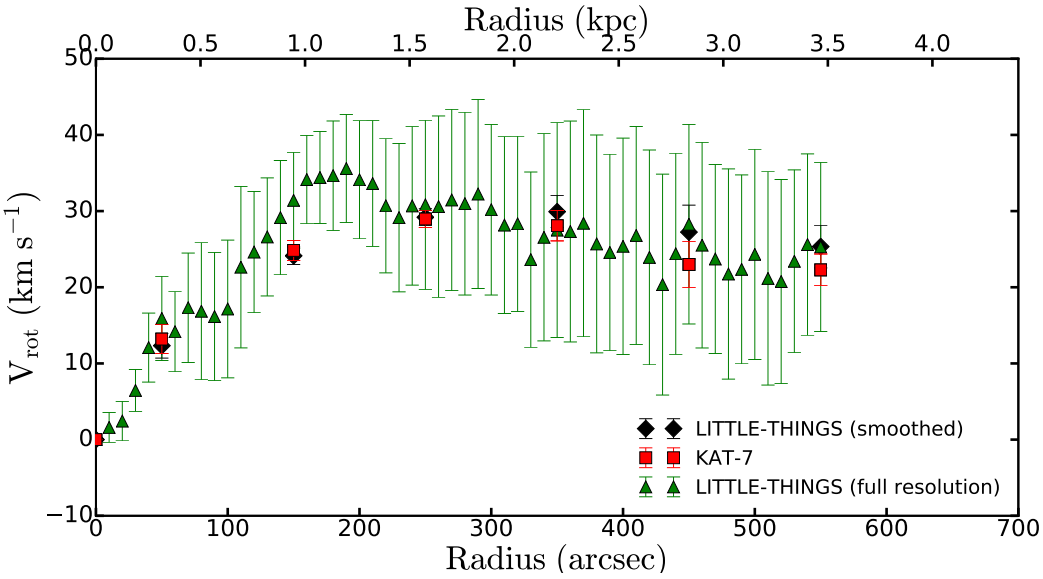

Figure 3.9: Comparison of the KAT-7 and VLA LITTLE THINGS rotation curves of Sextans A. The red square show the KAT-7 rotation curve, the black triangles show the LITTLE THINGS RC smoothed to the KAT-7 spatial resolution, and the green triangles show the full resolution LITTLE THINGS RC.

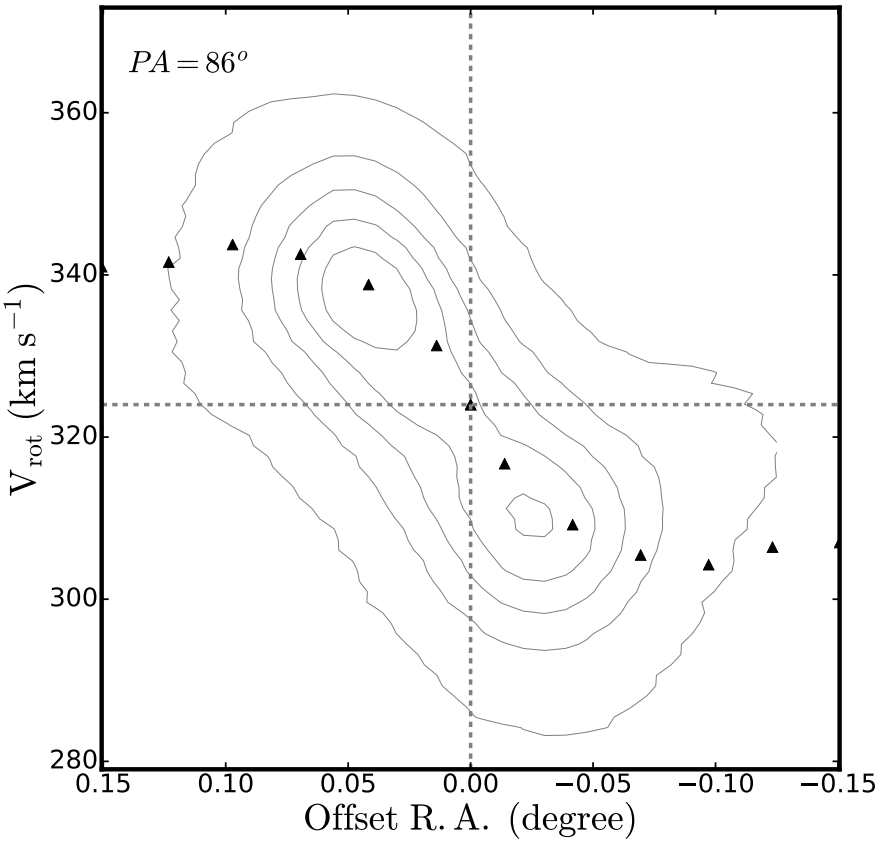

Figure 3.10: Position velocity diagram of Sextana A with the projected rotation curve over plotted. The dotted grey lines represent the centre of the galaxy and the systemic velocity. Superimposed is the rotation curve derived from the tilted ring model, corrected for the inclination of a slice along the galaxy major axis

In Figure 3.12, we compare the observed velocity field (a) to the derived model velocity field (c), while (d) shows the residual map (observed velocity field - model velocity field). (c) shows the velocity dispersion map. It can be seen that the model is a very good representation of the velocity field with most residuals smaller than 5 km s^{-1}. In Figure 3.13, the KAT-7 rotation curve of Sextans B is compared to the RC derived from the VLA LITTLE THINGS data (Hunter et al., 2012) (full resolution and smoothed to KAT-7 spatial resolution). The rotation curves do not show a good agreement as for Sextans A, especially in the inner parts, where the effect of beam smearing of the KAT-7 observations is more important than in Sextans A. Figure 3.14 shows the rotation curve overlaid on a position-velocity (PV) diagram obtained along the major axis. The rotation curve shows a good representation of the dynamics of the galaxy.

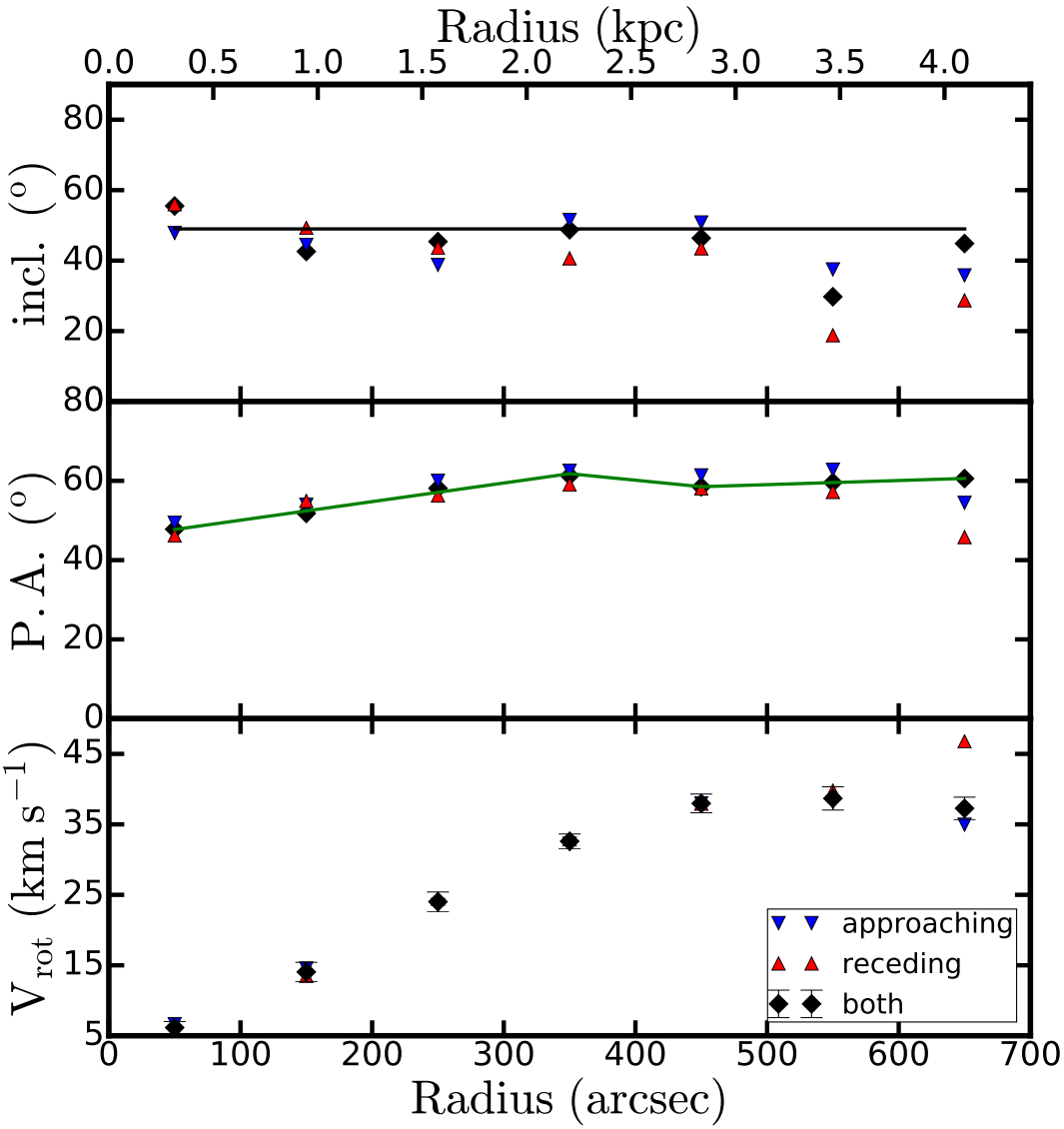

Figure 3.11: Results of the tilted ring fits for Sextans B. For the middle and top panels, the blue and red triangles and the black diamonds show the behavior of the PA and inclination as free parameters while the black solid lines show the behavior of the PA and inclination fixed to the model used to derive the final rotation curve. In this case the PA is varying while the inclination is fixed to the mean value. For the bottom panel, the blue triangles represent the curve for the approaching side while the red triangles represents the curve for the receding side.

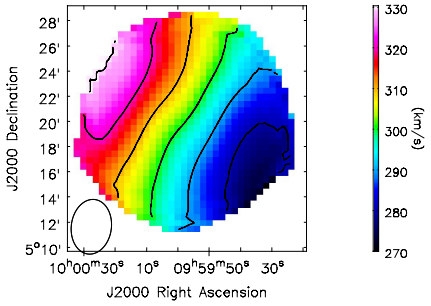

(a) Observed velocity field map

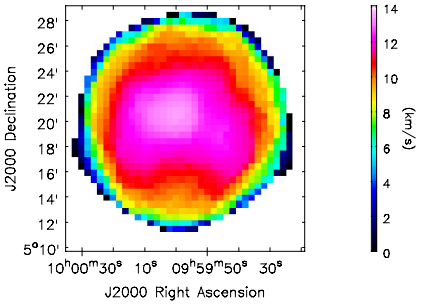

(b) Velocity dispersion map

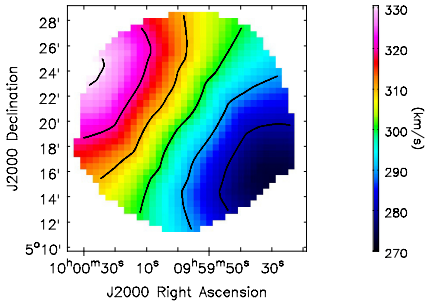

(c) Model velocity field map

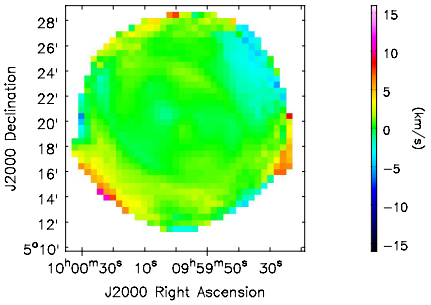

(d) Residual velocity field map

Figure 3.12: Maps of Sextans B: Observed velocity field map (a), velocity dispersion map (b), model velocity field (c), and residual map (d). The observed and model velocity field contours run from 280 to 340 km s^{-1} in steps of 10 km s^{-1}.

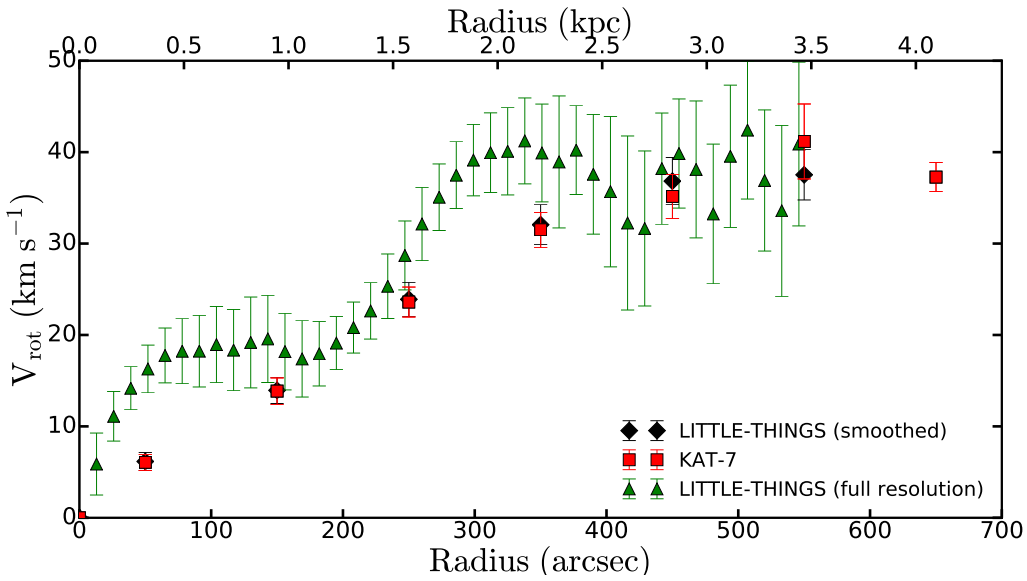

Figure 3.13: Comparison of the KAT-7 and VLA LITTLE THINGS rotation curves of Sextans B. The red square show the KAT-7 rotation curve, the black triangles show the LITTLE THINGS RC smoothed to the KAT-7 spatial resolution, and the green triangles show the full resolution LITTLE THINGS RC.

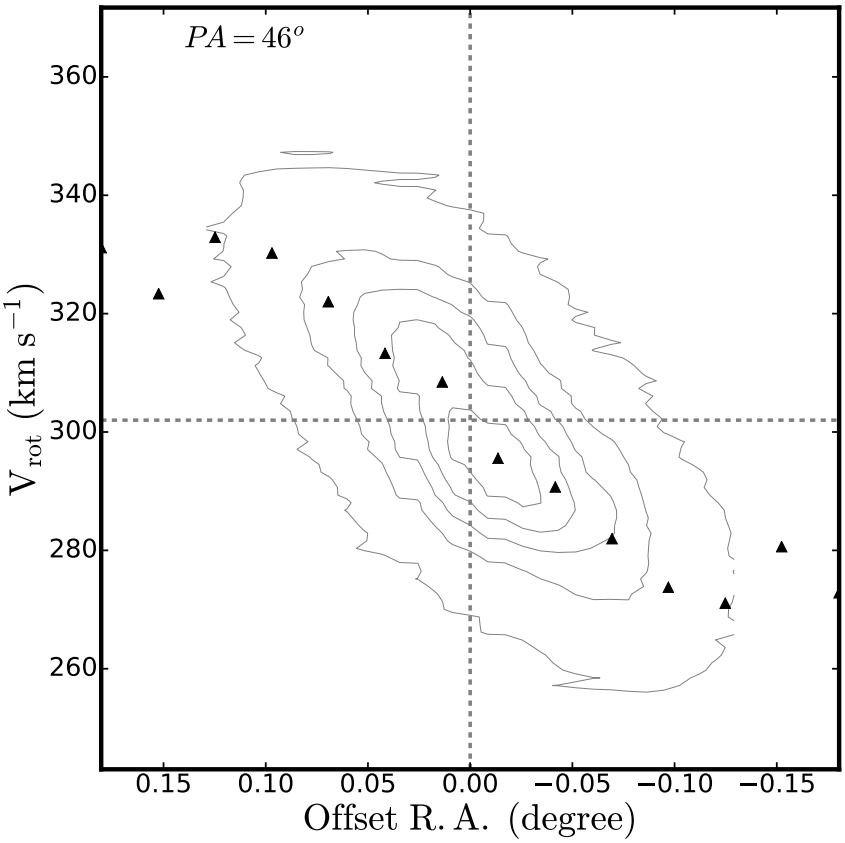

Figure 3.14: Position velocity diagram of Sextana B with the projected rotation curve over plotted. The dotted grey lines represent the centre of the galaxy and the systemic velocity. Superimposed is the rotation curve derived from the tilted ring model, corrected for the inclination of a slice along the galaxy major axis

3.6 Mass models and dark matter content

The rotation curve reflects the dynamics of the disk due to the total mass of the galaxy, luminous and dark matter. Dwarf irregulars, like most low-mass surface density galaxies, are believed to be dominated by dark matter at all radii due to the small contribution of luminous matter (stars and gas) to the total dynamics (Carignan & Beaulieu, 1989). The extended HI rotation curves of dwarf irregulars allow us to probe dark matter potentials to much larger radii, making them ideal objects for studying dark matter properties in galaxies. To this end, we decompose the observed rotation curve of Sextans A and B into the luminous and dark matter mass components and verify if dark matter indeed dominates the total dynamics of these systems. The pseudo-isothermal DM halo model (ISO) (Begeman et al., 1991) and the Navarro-Frenk-White DM halo model (NFW) (Navarro et al., 1997) have been used to derive the dark matter components of Sextans A and B. Detailed

Table 3.5: Radial variation of the HI surface densities Σ_g, the gas velocity dispersions σ, the observed rotation velocities V_0, the errors of the observed velocities ΔV, and the asymmetric drift corrected rotation velocities V_c for the KAT-7 data of Sextans B.

Radius arcsec	Σ_g $M_\odot pc^{-2}$	σ km s^{-1}	V_{rot} km s^{-1}	Δ V km s^{-1}	V_c km s^{-1}
0.0	3.7	13.3	0.0	0.0	0.0
50	3.5	13.2	6.1	0.9	6.2
150	2.7	12.7	14.1	1.5	16.6
250	1.8	12.1	24.0	1.5	28.1
350	0.9	11.1	32.6	1.0	37.6
450	0.4	9.7	37.9	1.3	43.4
550	0.2	8.8	38.6	1.8	44.4
650	0.1	6.9	37.3	6.0	41.3

Notes. Column (1) gives the radius, column (2) the surface densities, column (3) the velocity dispersion, column(4) the observed rotation velocities, column (5) the errors of those velocities, and column (6) the corrected velocities used for the mass models.

description of the mass models has been given in Namumba et al. (2017).

3.6.0.1 Gas and Stellar components

We derive the mass models for the stellar and gas components following the procedure described by Namumba et al. (2017). The Wide Field Infrared Survey Explorer (WISE) surface brightness profiles in the 3.4 μm band were used to account for the stellar contribution. The luminosity profiles are from Jarrett (private communication). At 3.4 μm, WISE probes the emission from the old stellar disk population and is also less affected by dust.

3.6.1 Fitting ISO and NFW models for Sextans A and B

The GIPSY task ROTMAS was used to construct the mass models of Sextans A and B. We fitted the ISO and NFW models to the rotation curves derived from the tilted ring models, taking into account the mass of the luminous matter (stars and gas). All the data points were weighted according to the errors using the inverse square weighting.

The values of the mass to light ratio, M/L were determined by scaling the contribution of the stellar rotation curve to the total rotation curve. This was done using two predetermined M/L values: 1), the M/L of 0.2 (Lelli et al., 2016). This value has been derived to be the lower end of the mass to light ratio for dwarf galaxies at mid-infrared band, and 2), the M/L derived using Equation 3.4 (Cluver et al., 2014).

This equation is used to calculate the M/L of star forming low mass galaxies.

$$\log_{10} = M_{stellar}/L_{W1} = -1.93(W_{3.4\mu m} - W_{4.6\mu m}) - 0.04 \quad (3.4)$$

where $W_{3.4\mu m}$ - $W_{4.6\mu m}$ is 0.04 ± 0.02 for Sextans A and 0.01 ± 0.02 for Sextans B. This gives the M/L of 0.9 and 0.8 for Sextans A and B respectively.

3.6.2 Mass model results for Sextans A

The fitted parameters for the mass model results of Sextans A are shown in Figure 3.15 and Table 3.6. Figure 3.15 shows that Sextans A is dark matter dominated at all radii. Regardless of the assumption made for the M/L ratio, the ISO model produces a better fit compared to the NFW at radius $\leqslant$ 1.3 kpc. Beyond that radius, the two models tend to give similar fits to the observed rotation curve. For the ISO halo models, we find the lowest χ^2 of 3.4 when the M/L value of 0.2 (Lelli et al., 2016) is used. It is not surprising that we get a better fit when we use a smaller M/L of 0.2. Literature shows that for most dwarf galaxies the stellar disk does not contribute significantly to the rotation curve (Weldrake et al., 2003; de Blok et al., 2008; Oh et al., 2011). The mass models yields DM halo parameters of $R_0 \sim 0.5$ kpc and $\rho_0 \sim 0.1$ $M_\odot$ pc^{-3}.

3.6.3 Mass model results for Sextans B

The dark matter models for Sextans B are shown in Figure 3.16 and Table 3.6. Both ISO and NFW models give larger χ^2 values than for the models of Sextans A but again ISO with an M/L of 0.2 (Lelli et al., 2016) gives the best fit to the data but with a small overestimate for r < 1.3 kpc. This suggests that M/L should be slightly smaller. Oh et al. (2015) derived a mass model for Sextans B using higher resolution observations. Their results show a better fit with smaller values of χ^2 compared to our mass model fits. However, this can be due to the fact that they only fit the rising part of their derived rotation curve, leaving out the outer radii were the rotation velocities are declining.

3.6.4 MOND Models

The Modified Newtonian Dynamics (MOND) was proposed by (Milgrom, 1988) as an alternative to DM. Milgrom postulated that at small accelerations the usual Newtonian dynamics break down and that the law of gravity needs to be modified. MOND claims to be able to explain the mass discrepancies in galaxies with only the contributions of the gas and stellar components without DM. Several authors have been able to explain the mass distributions of galaxies without DM using MOND (Begeman et al., 1991; Sanders, 1996; Bottema et al., 2002; Randriamampandry & Carignan, 2014).

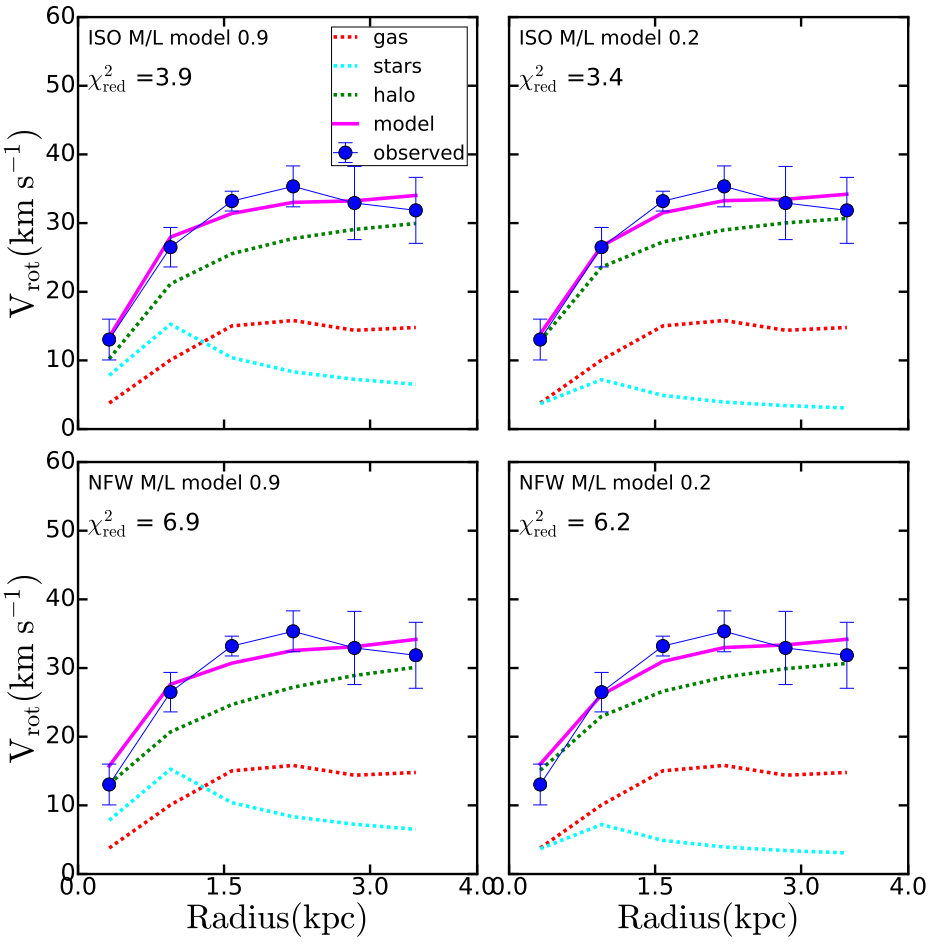

Figure 3.15: ISO and NFW mass modeling results of Sextans A. The decomposition of Sextans A rotation curve using two assumption of M/L. The blue circles indicate the observed rotation curve, the magenta lines show the fitted rotation curve, the green dotted lines indicate the dark matter rotation velocities, and the red dot-dashed and blue dashed lines show the rotation velocities of the gas and of the stellar components, respectively.

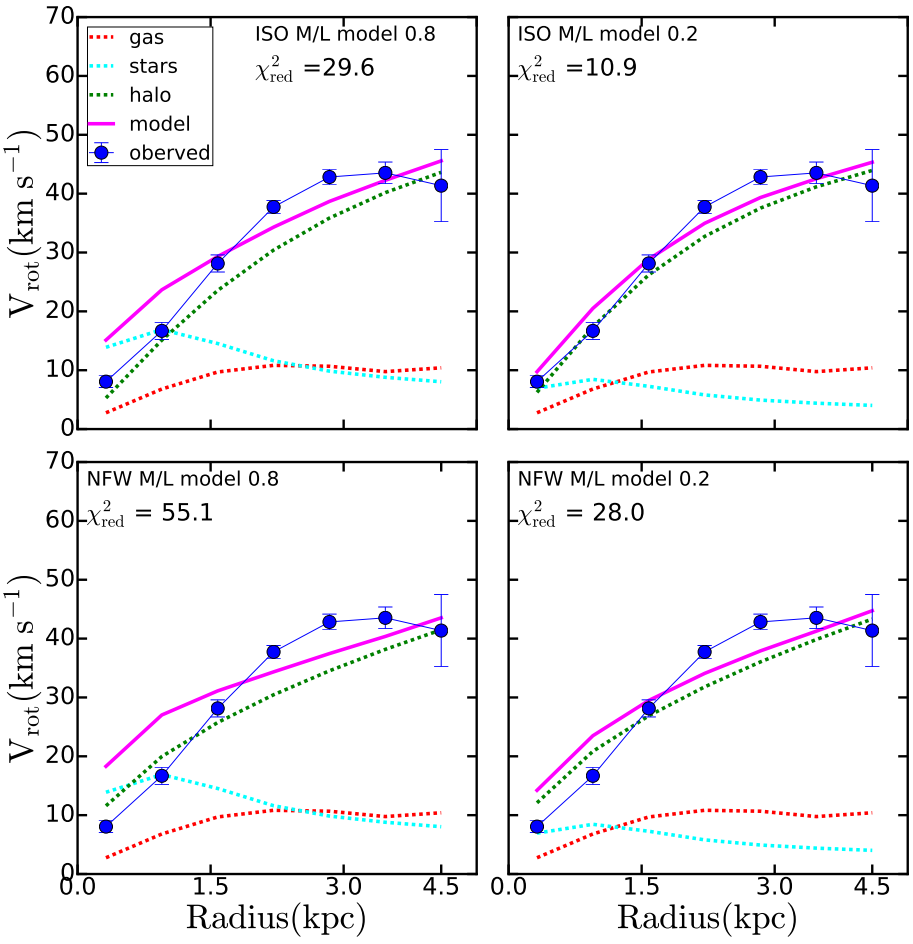

Figure 3.16: ISO and NFW mass modeling results of Sextans B. The decomposition of Sextans B rotation curve using two assumption of M/L. The blue circles indicate the observed rotation curve, the magenta lines show the fitted rotation curve, the green dotted lines indicate the dark matter rotation velocities, and the red dot-dashed and blue dashed lines show the rotation velocities of the gas and of the stellar components, respectively.

Table 3.6: Results for the Mass Models Sextans A and Sextans B.

		Sextans A		
		ISO Halo		
Assumption	M/L	R_0	ρ_0	χ^2_{red}
(1)	(2)	(3)	(4)	(5)
M/L model$_a$	0.90	0.46 ± 0.11	93.57± 35.18	3.90
M/L model$_b$	0.20	0.40 ± 0.08	125.39± 44.61	3.40
		NFW Halo		
Assumption	M/L	c	R_{200}	χ^2_{red}
(6)	(7)	(8)	(9)	(10)
M/L model$_a$	0.90	10.61 ± 3.49	35.57± 6.98	6.90
M/L model$_b$	0.20	12.62± 3.71	33.84±5.57	6.20
		Sextans B		
		ISO Halo		
Assumption	M/L	R_0	ρ_0	χ^2_{red}
(11)	(12)	(13)	(14)	(15)
M/L model$_a$	0.80	2.45 ± 1.58	15.21± 8.71	29.66
M/L model$_b$	0.20	1.86 ± 0.57	21.35± 6.96	10.93
		NFW Halo		
Assumption	M/L	c	R_{200}	χ^2_{red}
(16)	(17)	(18)	(19)	(20)
M/L model$_a$	0.80	-0.38 ±	1494.36±	55.16
M/L model$_b$	0.20	-0.35±	1518.18±....	28.04

Notes. Columns 1, 11 and 6, 16, the stellar M/L assumption. Column 2, 12 and 7,17, Υ_* . Column 3, 13, fitted scaling radius of the ISO halo model in kpc. Column 4, 14, fitted central density of the pseudo-isothermal halo model in 10^{-3} $M_\odot$ pc^{-3}. Column 9, 19 the radius in kpc where the density contrast exceeds 200. Column 8, 18 concentration parameter c of the NFW halo model. Columns 5, 15 and 10, 20, reduced χ^2 value. The dotted line (...) are due to unphysical large values of uncertainties. Model$_a$ represent a M/L ratio derived using equation 3.4 while model$_b$ presents a M/L ratio by Lelli et al. (2016)

The shape of the predicted MOND rotation curve depends on the interpolating function. The standard (Milgrom, 1983) and the simple (Famaey & Binney, 2005) interpolating functions are mostly used in the literature. Famaey & Binney (2005) claimed that the simple interpolation function gives more realistic M/L values. This is why we have adopted this interpolation function for our analysis.

3.6.5 MOND fits for Sextans A and B

The MOND fitting procedure has two free parameters. We fit the rotation curve with a_0 fixed to the universal constant of 1.2 $\times 10^{-8}$ cm.s^{-2} (Begeman et al., 1991) while letting M/L free for the simple interpolation function. On the other hand, we let the universal constant free while the M/L is fixed to a value as the ones used for the DM models. We note that although the universal constant a_0 is expected to be the same for all astrophysical objects, observational biases can cause scatter in a_0 which can lead to a significant departure of the universal constant from the standard value.

The MOND results for Sextans A and B are given in Figure 3.17 and 3.18. Table

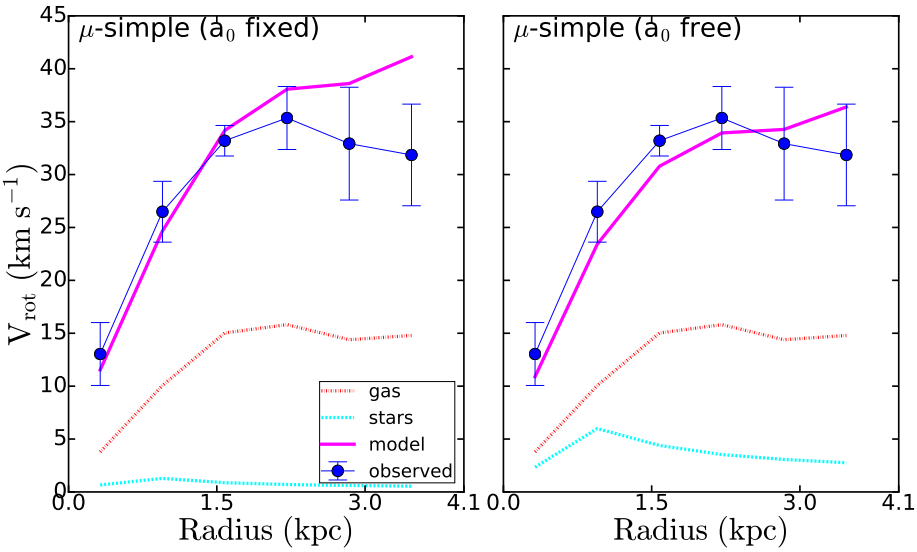

Figure 3.17: MOND mass models for Sextans A with a_0 fixed (left) and a_0 free (right) for the simple interpolation function. The red dashed curve is for the HI disk, the dash-dotted light blue curve is for the stellar disk, and the continuous purple curve is the MOND contribution.

3.7 shows the derived MOND parameters of the two galaxies. The discrepancies between the observed rotation curve and the RC predicted by MOND are visible in both Sextans A and B. The fits give high values of the reduced χ^2, with better fits derived when a_0 is allowed to vary. This poses a challenge as a_0 should be a universal constant. The best result is obtained for Sextans A with a_0 free. However, this model suggests a value of a_0 much smaller than the standard value.

3.6.6 Comparison with the literature

There are a lot of studies on the dark matter distribution in dwarf galaxies in the literature, but this section will focus on the comparison between this work and that of Oh et al. (2011), which looks at the dark matter distribution of the LITTLE THINGS galaxies. A dominant trend in the core-like distribution has been reported by Oh et al. (2011). This is in agreement with our mass model results in which the ISO model produces better fits as compared to the NFW model. The KAT-7 ISO model fits suggest a dark matter core radius of R_c = 0.46 to 2.45 kpc and density ρ_0 = 15 to 125 $M_\odot$ pc^{-3}. The values are in the range of Oh et al. (2011). Oh et al. (2011) found the values of R_c and ρ_0 to be in the range 0.10 to 9.82 kpc and 1.8 to 725 $M_\odot$ pc^{-3} respectively.

For both observations, we see cases were the NFW fit yields unrealistic halo parameters when trying to fit the observed RCs. From our KAT-7 data, we obtained c values < 0 for Sextans B while the LITTLE THINGS observations record c values

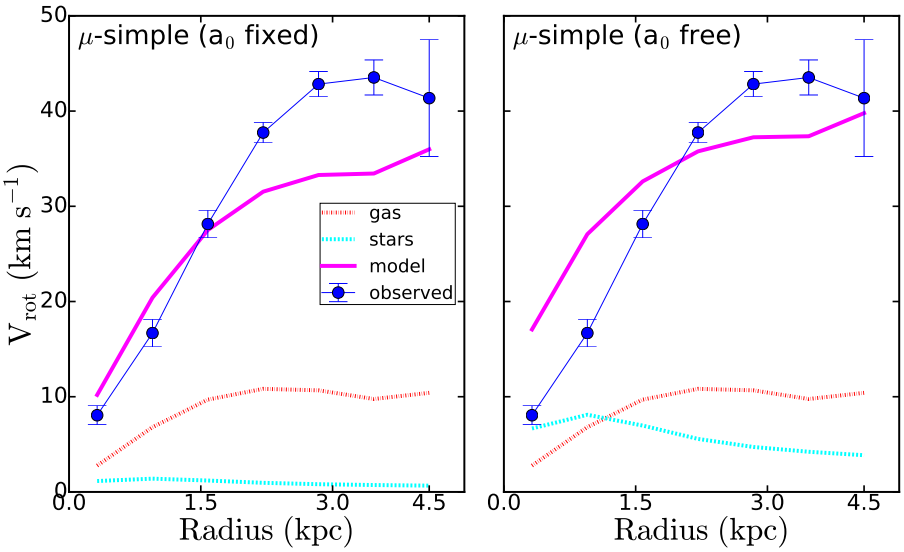

Figure 3.18: MOND mass models for Sextans B with a_0 fixed (left) and a_0 free (right) for the simple interpolation function. The red dashed curve is for the HI disk, the dash-dotted light blue curve is for the stellar disk, and the continuous purple curve is the MOND contribution.

< 0.1 for DD0 53 and NGC 2366. As emphasized by de Blok et al. (2008), c represents the collapse factor, and therefore c values < 1 make no sense in the CDM context. The estimated concentration parameter for Sextans A is ~ 11. The LITTLE THINGS observations record c values ranging from ~ 4 to 48. The concentration parameter for Sextans A is within the LITTLE THINGS range and also consistent with c values derived for most dwarf galaxies (de Blok et al., 2008). We obtain V_{200} of 26 km s^{-1} for Sextans A. This value is in the range of Oh et al. (2011). Oh et al. (2011) record V_{200} values ranging from 3.7 to 58 km s^{-1}.

One thing to note from our KAT-7 mass model fits is that although we do not get perfect fits to our observed RCs, the parameters we derived for Sextans A and B are in agreement and within the ranges found for other dwarf galaxies.

3.7 Star formation thresholds

The mechanisms that assist star formation activities in low surface brightness (LSB) galaxies remain a puzzling question. The low stellar densities in most gas rich LSB galaxies imply that the star formation process has been inefficient in converting the available gas into stars. Several studies (Hunter & Plummer, 1996; Hunter et al., 1998; de Blok & Walter, 2006) have been able to show that, although being gas rich, the gas densities in most LSB galaxies fall below the threshold needed to support star formation.

Table 3.7: Results for the MOND Models of Sextans A and B for the KAT-7 Data.

Sextans A		
a_0 (cm.s^{-2})	Parameter	Result
Fixed (1.2×10^{-8})	(M/L)	0.006
	$\chi^2_{\rm red}$	26.40
Free (6.9×10^{-9})	(M/L)	0.2
	$\chi^2_{\rm red}$	6.40
Sextans B		
a_0 (cm.s^{-2})	Parameter	Result
Fixed (1.2×10^{-8})	(M/L)	0.005
	$\chi^2_{\rm red}$	46.50
Free (1.5×10^{-8})	(M/L)	0.2
	$\chi^2_{\rm red}$	47.44

Kennicutt (1989) found that a modified Toomre-Q criterion model, could satisfactorily describe the star formation threshold gas densities in active star forming galaxies. In this model, the density above which the gas becomes unstable and form stars is a function of the kinematics of the galaxy. The threshold for star formation depends on the stability parameter α_Q, which is defined by (Martin & Kennicutt, 2001):

$$\alpha_Q = \frac{\Sigma_g}{\Sigma_c} \tag{3.5}$$

where Σ_g is the gas surface density corrected for helium and other metals, and Σ_c is the critical density for cloud formation. The critical density is described by (Martin & Kennicutt, 2001):

$$\Sigma_c = \alpha_Q \frac{\sigma k}{\pi G} \tag{3.6}$$

where σ is the gas velocity dispersion, α is a constant close to unity which is included to account for a more realistic disk, and $k(r)$ is the epicyclic frequency given by

$$k^2 = 2\left(\frac{V_{\rm rot}^2}{r^2} + \frac{V_{\rm rot}}{R}\frac{dV_{\rm rot}}{dr}\right) \tag{3.7}$$

where V_{rot} is the rotation velocity in km s^{-1}, and r is the radius in km. Kennicutt (1989) found α_Q = 0.63 at the edge of star forming disks and Martin & Kennicutt (2001) found α_Q = 0.69. If Σ_g, the surface density of the gas in the disk exceed Σ_c, then the disk will be unstable to axisymmetric disturbances and large scale star formation can occur.

An alternative to the Toomre-Q criteria is the cloud growth criteria based on shear. This criteria explains the star formation threshold based on the local shear rate (Hunter et al., 1998) and is described by the Oort's A constant:

$$A = -\frac{1}{2}r\frac{d\Omega}{dr} = \frac{1}{2}\left(\frac{V_{\rm rot}}{r} - \frac{dV_{\rm rot}}{dr}\right), \tag{3.8}$$

Then the threshold has the form

$$\Sigma_A = \frac{\alpha_A \sigma A}{\pi G} \tag{3.9}$$

Where α_A is taken to be 2.5 (Hunter et al., 1998), but the normalization for Σ_A is relatively uncertain. In this case, the threshold parameter α_A is defined by

$$\alpha_A = \frac{\Sigma_g}{\Sigma_A} \tag{3.10}$$

We have used the KAT-7 observations to examine the star formation threshold throughout Sextans A and B as a function of radius to determine if the subcritical gas density is preventing the galaxies from large scale star formation. To derive the critical densities, a constant gas velocity dispersion σ of 9 km s^{-1} is used. This is derived from the medium value of our azimuthally averaged HI velocity dispersion radial profile. We have assumed α_Q = 1 and establish the ratios of the gas densities to the critical densities as a function of radii using the Toomre-Q and cloud-growth based on shear criteria.

3.7.1 Star formation threshold results for Sextans A and B

Figure 3.19(a) and (b) compares the observed HI gas surface densities to the critical densities derived using the Toomre-Q (Kennicutt, 1989) and the cloud-growth based

on shear (Hunter et al., 1998) criterion for Sextans A and B respectively. The gas surface densities in Sextans A and B are low relative to the Toomre-Q critical densities Σ_c necessary for instabilities that lead to cloud formation and later star formation. We find that the critical densities Σ_A in Sextans A exceed the gas surface density at all radii. For Sextans B, Σ_A is lower than the gas surface density in regions $\leqslant$ 2.1 kpc.

Figure 3.20(a) and (b) shows the radial dependance of the ratios Σ_g/Σ_c and Σ_g/Σ_A for Sextans A and B respectively. We see that for both galaxies, the ratios derived from the Toomre-Q critical densities Σ_g/Σ_c fail to predict the observed star formation in Sextans A and B. At all radii, Σ_g/Σ_c is below the stability parameter α_Q = 0.63, the median value from Kennicutt (1989) above which the gas density is high enough for large scale star formation. We calculate a mean α_Q = 0.25 and 0.20 for Sextans A and B by finding the ratio Σ_g/Σ_c from the center to the Holmberg radius. This result suggests that the gas surface density in Sextans A and B is low to effectively form stars if the Toomre-Q stability criterion is used to determine the star formation in these galaxies.

The ratio Σ_g/Σ_A seems better suited to explain the star formation in Sextans A and B. In both galaxies, Σ_g/Σ_A exceeds the stability parameter α = 0.63 in the inner regions. We measure a mean α_A value of 0.64 and 5 for Sextans A and B respectively. These results suggest that shear may play an important role in facilitating cloud formation and later induce star formation in Sextans A and B.

Many different models have been used to examine the star formation threshold in dwarf galaxies. Hunter et al. (1998) used different models to determine regions of star formation using a sample of spiral and dwarf galaxies. Their results showed that for dwarf galaxies, the Toomre-Q ratio α_Q was too low to induce star formation at all radii. Examples of their derived average α_Q values include: 0.45 for IC 1613, 0.36 for DD0 154, 0.30 for DD0 155, and 0.26 for Sextans A. These values are in excellent agreement with our calculated α_Q values of Sextans A and B using the KAT-7 observations. We reach the same conclusion as Hunter et al. (1998) that the cloud-growth criterion based on shear is well suited to explain star formation in star forming regions of dwarf galaxies. In most cases, Hunter et al. (1998) derived α_A values close to 1. We see that the high values of Σ_g/Σ_A derived for Sextans B are not odd when compared with the literature. Hunter et al. (1998) records high Σ_g/Σ_A for IC 1613 and DD0 50, showing the highest peak ~ 10.

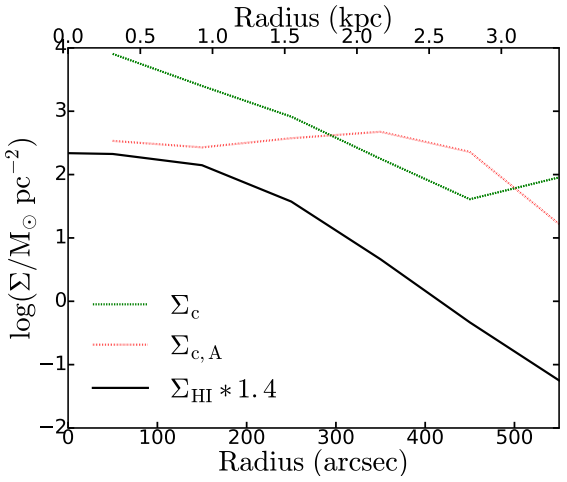

(a) Sextans A

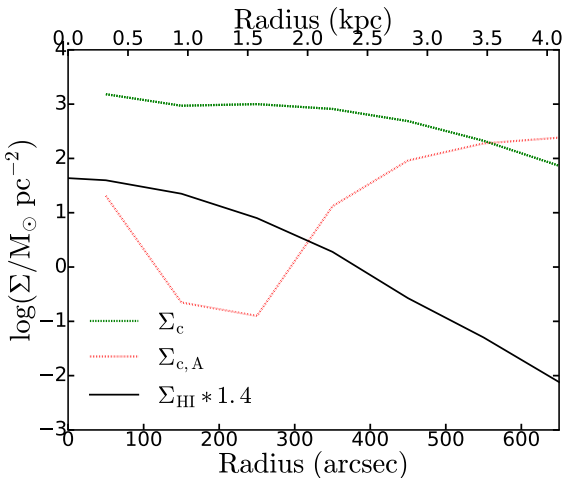

(b) Sextans B

Figure 3.19: Shows the gas surface density, black solid line (corrected for helium), the green dashed line shows the critical density derived using the Kennicutt (1989), and the red dash-dotted line shows the critical density as derived by Hunter et al. (1998).

3.8 Summary and conclusion

We have obtained high sensitivity, intermediate resolution HI observations of Sextans A and B and have used them to study the HI distribution, kinematics, and star formation thresholds. At column densities of 5.8 and 5.4 $\times 10^{18}$ cm^{-2} for Sextans A and B, we do not detect new HI emission. In fact, our results, which are close to the GBT and VLA, contradicts the large extents and fluxes claimed by Huchtmeier et al. (1981) from the Effelsberg observations.

A tilted ring model is fitted to the HI velocity fields to derive the rotation velocities. We measure the RCs of Sextans A and B out to 3.5 and 4.0 kpc respectively. The RCs of both galaxies are seen to decline at outer radii. However, considering the large

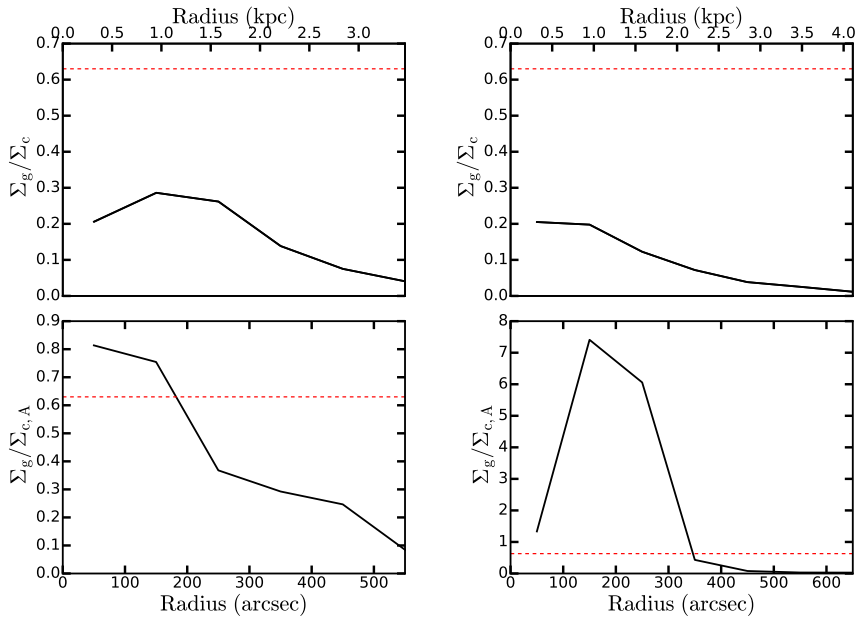

(a) Sextans A

(b) Sextans B

Figure 3.20: The radial variation in the ratios of the observed gas surface density to the critical densities for Sextans A (a) and Sextans B(b). The top panel shows the ratio $\alpha_c = \Sigma_{HI/\Sigma_c}$ calculated using the Toomre-Q while the bottom panel shows the ratio $\alpha_A = \Sigma_{HI/\Sigma_A}$ calculated using cloud-growth criteria based on shear. The red dashed line shows $\alpha_Q = 0.63$, the median value from Kennicutt (1989) above which the gas density is high enough for large scale star formation.

uncertainties in the rotation velocities and the fact that the decline is not Keplerian clearly shows that DM is still present in these galaxies. For Sextans A, we calculate a mean V_{sys} = 342 ± 0.6 km s^{-1}, P.A. = 34°, and inclination = 86° while V_{sys} = 302 ± 0.9 km s^{-1}, P.A. = 57°, and inclination = 49° are calculated for Sextans B.

Using the observed RCs as mass model inputs show that the galaxies have a higher fraction of dark matter compared to luminous matter (gas and stars). For Sextans A, the ISO DM model reproduces better the observed RC than the NFW model. In the case of Sextans B both DM models fail to represent properly the data but with a slightly better fit for the ISO model with a M/L of 0.2. Better mass model fittings are obtained when the stellar disk does not contribute significantly to the rotation curve. Fixing the M/L to a predetermined value of 0.2 (Lelli et al., 2016) produces better fits than using high M/L values of 0.9 and 0.8 for Sextans A and B derived in the infrared band using the WISE colors. For both galaxies, the MOND model produces better fit when a_0 is allowed to vary. This poses a challenge as a_0 should be considered as a universal constant.

The derived α_Q and α_A values suggest that the inner regions of Sextans A and

B, star formation can be better explained using the cloud-growth criterion based on shear as compared to the Toomre-Q criterion, as was found previously for NGC 6822 (Namumba et al., 2017). However, it is important to note that these studies are only based on the HI observations and therefore additional observations on star formation will be required to make a conclusive analysis on the star formation threshold of Sextans A and B.

Barnes D. G., de Blok W. J. G., 2004, MNRAS, 351, 333

Begeman K. G., 1989, A&A, 223, 47

Begeman K. G., Broeils A. H., Sanders R. H., 1991, MNRAS, 249, 523

Bottema R., Pestaña J. L. G., Rothberg B., Sanders R. H., 2002, A&A, 393, 453

Carignan C., Beaulieu S., 1989, ApJ, 347, 760

Carignan C., Purton C., 1998, ApJ, 506, 125

Carignan C., Beaulieu S., Freeman K. C., 1990, AJ, 99, 178

Carignan C., Frank B. S., Hess K. M., Lucero D. M., Randriamampandry T. H., Goedhart S., Passmoor S. S., 2013, AJ, 146, 48

Cluver M. E., et al., 2014, ApJ, 782, 90

Côté S., Carignan C., Freeman K. C., 2000, AJ, 120, 3027

Dicaire I., Carignan C., Amram P., Marcelin M., Hlavacek-Larrondo J., de Denus-Baillargeon M.-M., Daigle O., Hernandez O., 2008, AJ, 135, 2038

Dolphin A. E., et al., 2003, AJ, 126, 187

Famaey B., Binney J., 2005, MNRAS, 363, 603

Foley A. R., et al., 2016, MNRAS, 460, 1664

Gentile G., Salucci P., Klein U., Granato G. L., 2007, MNRAS, 375, 199

Heald G., et al., 2016, MNRAS, 462, 1238

Hess K. M., Cluver M. E., Yahya S., Leisman L., Serra P., Lucero D. M., Passmoor S. S., Carignan C., 2017, MNRAS, 464, 957

Huchtmeier W. K., Seiradakis J. H., Materne J., 1981, A&A, 102, 134

Hunter D. A., Plummer J. D., 1996, ApJ, 462, 732

Hunter D. A., Elmegreen B. G., Baker A. L., 1998, ApJ, 493, 595

Hunter D. A., Zahedy F., Bowsher E. C., Wilcots E. M., Kepley A. A., Gaal V., 2011, AJ, 142, 173

Hunter D. A., et al., 2012, AJ, 144, 134

Karachentsev I. D., et al., 2002, A&A, 389, 812

Kennicutt Jr. R. C., 1989, ApJ, 344, 685

Kniazev A. Y., Grebel E. K., Pustilnik S. A., Pramskij A. G., Zucker D. B., 2005, AJ, 130, 1558

Kreckel K., Peebles P. J. E., van Gorkom J. H., van de Weygaert R., van der Hulst J. M., 2011, AJ, 141, 204

Lelli F., McGaugh S. S., Schombert J. M., 2016, AJ, 152, 157

Lucero D. M., Carignan C., Elson E. C., Randriamampandry T. H., Jarrett T. H., Oosterloo T. A., Heald G. H., 2015, MNRAS, 450, 3935

Martin C. L., Kennicutt Jr. R. C., 2001, ApJ, 555, 301

McMullin J. P., Waters B., Schiebel D., Young W., Golap K., 2007, in Shaw R. A., Hill F., Bell D. J., eds, Astronomical Society of the Pacific Conference Series Vol. 376, Astronomical Data Analysis Software and Systems XVI. p. 127

Meurer G. R., Carignan C., Beaulieu S. F., Freeman K. C., 1996, AJ, 111, 1551

Milgrom M., 1983, ApJ, 270, 384

Milgrom M., 1988, ApJ, 333, 689

Namumba B., Carignan C., de Blok W. J. G., Passmoor S., 2017, Monthly Notices of the Royal Astronomical Society, 472, 3761

Navarro J. F., Frenk C. S., White S. D. M., 1997, ApJ, 490, 493

Nidever D. L., et al., 2013, ApJ, 779, L15

Oh S.-H., de Blok W. J. G., Brinks E., Walter F., Kennicutt Jr. R. C., 2011, AJ, 141, 193

Oh S.-H., et al., 2015, AJ, 149, 180

Ott J., et al., 2012, AJ, 144, 123

Pisano D. J., 2014, AJ, 147, 48

Randriamampandry T. H., Carignan C., 2014, MNRAS, 439, 2132

Sanders R. H., 1996, ApJ, 473, 117

Schmidt P., Józsa G. I. G., Gentile G., Oh S.-H., Schuberth Y., Ben Bekhti N., Winkel B., Klein U., 2014, A&A, 561, A28

Skillman E. D., Bothun G. D., 1986, A&A, 165, 45

Skillman E. D., Terlevich R., Teuben P. J., van Woerden H., 1988, A&A, 198, 33

Weldrake D. T. F., de Blok W. J. G., Walter F., 2003, MNRAS, 340, 12

Wilcots E. M., Hunter D. A., 2002, AJ, 123, 1476

Wilcots E. M., Miller B. W., 1998, AJ, 116, 2363

Worth R., Wilcots E. M., 2009, in American Astronomical Society Meeting Abstracts #213. p. 251

de Blok W. J. G., Walter F., 2000, ApJ, 537, L95

de Blok W. J. G., Walter F., 2006, AJ, 131, 363

de Blok W. J. G., Walter F., Brinks E., Trachternach C., Oh S.-H., Kennicutt Jr. R. C., 2008, AJ, 136, 2648

de Vaucouleurs G., de Vaucouleurs A., Corwin Jr. H. G., Buta R. J., Paturel G., Fouqué P., 1991, Third Reference Catalogue of Bright Galaxies. Volume I: Explanations and references

CHAPTER 4

HI OBSERVATIONS OF IC 10 WITH THE DRAO SYNTHESIS TELESCOPE

We present HI observations of the nearby blue compact dwarf galaxy IC 10 obtained with the DRAO synthesis telescope (DRAO). We do not detect the new 1.3° HI feature seen with the GBT in either the Effelsberg (EBHIS) survey or our DRAO data. In the inner disk, the rotation curve of IC 10 rises steeply, then flattens until the last point where it rises again, with a maximum velocity of 30 km s^{-1}. Based on our mass models, the kinematics of the inner disk of IC 10 can be described without the need of a dark matter halo. However, this does not exclude the possible presence of dark matter on a larger scale. It is unlikely that the features seen in the HI disk of IC 10 are caused by an interaction with M 31. Features seen from our simulations are larger and at lower surface density than can be reached by current observations. The higher velocity dispersions seen in regions were several distinct HI features meet with the main core of IC 10 may suggest that there is ongoing accretion.

4.1 Introduction

Dwarf galaxies are fundamental laboratories used to constrain the impact that structural and intrinsic properties have on the evolution of galaxies. Investigating the physical processes occurring in dwarf galaxies is therefore crucial for understanding a wide range of astrophysical phenomena, from star formation mechanisms to the way galaxies are connected to their environment. Among the different dwarf galaxies, blue compact dwarf galaxies (BCDs) are the most fascinating and puzzling objects. While star forming dwarf galaxies are generally known to be inefficient at transforming their gas into stars (Leroy et al., 2008), a different case is observed for BCDs. BCDs are known to be undergoing violent bursts of star formation
(Sargent & Searle, 1970; Meurer et al., 1994; Gil de Paz et al., 2003; Lee et al., 2004;

Wu et al., 2006). However it remains unclear what mechanisms are responsible for the ignition of the star bursts in these systems.

Whilst studies have shown that gravitational interaction, mergers, or accretion can explain the burst of star formation in certain BCDs Wilcots & Miller (1998); Noeske et al. (2001); Bekki (2008); Nidever et al. (2013); Cloet-Osselaer et al. (2014), the absence of nearby companions around most BCDs suggests that mergers or interactions are unlikely starburst triggers. This, however, does not completely rule out possible interactions with companions or HI clouds that may be too faint to be detected and may have been missed in earlier studies of BCDs.

The neutral hydrogen atomic (HI) gas has been known to be an ideal tracer for the starburst triggers in galaxies Taylor et al. (1993, 1995, 1996a,b). This is because external disturbances are detected easily in HI 21 cm-line images in comparison to the optical images. From the HI morphology, signatures of interactions and mergers can easily be seen in the form of bridges or tidal tails (Nidever et al., 2013). Bridges are often associated with early stages of mergers or on-going interactions while tidal tails are often linked to past close encounter events with other galaxies. In addition to this, progressive stages of interactions can be traced from HI kinematical disturbances.

IC 10 (UGC 192) located at a distance of 0.7 Mpc (Hunter et al., 2012) is the only known BCD galaxy in the Local Group. Its proximity makes it an excellent candidate for exploring starburst triggers in BCD galaxies. IC 10 is located at the low galactic latitude (l=118°.95,b=-3°.33) where the foreground reddening is expected to be large. In addition, the internal reddening of IC 10 may vary spatially due to its strong star-forming activity. Therefore, it is difficult to determine reliably the reddening and distance of IC 10 (Kim et al., 2009). The presence of so many WR stars (Mateo, 1998) and high Hα luminosity suggest that the starburst in IC 10 must have occurred ~ 10 Myrs ago (Richer et al., 2001). The basic parameters of IC 10 are given in Table 4.1. The first HI observations of IC 10 with the single dish 100 m Effelsberg telescope revealed a huge HI extending 80′ in diameter (Huchtmeier, 1979). Early interferometric HI observations showed that the outer regions of IC 10 were rotating counter-clockwise with respect to a regularly inner rotating disk (Shostak & Skillman, 1989; Wilcots & Miller, 1998). Recent HI observations with the Green Bank Telescope revealed a new extended faint feature stretching 1.3 degrees north-west of IC 10 (Nidever et al., 2013). Detailed analysis of these observations combined with high spatial resolution VLA data (LITTLE THINGS) showed that the HI disk of IC 10 is much more extended than previously reported (Ashley et al., 2014) if the faint features seen with the GBT are real (see Section 4.3.4).

Different mechanisms have been proposed to explain starburst triggers and the observed disturbed morphology and kinematics in IC 10. Shostak & Skillman (1989) suggested that the observed complex morphology of IC 10 could be the result of IC 10 colliding with the intergalactic medium. They, however, highlighted that given the similarity of IC 10 with other dwarf galaxies, it is likely that the HI observed in this galaxy is primordial gas which is still in a collapse phase. Wilcots & Miller (1998) analyzed high-resolution HI data of IC 10 and concluded that the observed extended and counter-rotating distribution of gas in IC 10 was due to accretion. They explained that the features seen in IC 10 correspond to what would be seen for a galaxy experiencing later stages of formation via the ongoing infall of the primordial material. Recent HI studies of IC 10 suggest that an interaction or merger with another unknown low surface density dwarf galaxy is the most probable explanation for the observed morphology of this galaxy (Nidever et al., 2013; Ashley et al., 2014). However, Gerbrandt et al. (2015) argued that the lack of streams or shells, or any disturbances in the stellar component of IC 10 strongly indicates that it is unlikely that IC 10 has undergone an interaction with an unknown companion. Nidever et al. (2013) used a Gravitylab N-body integrator code to perform orbit calculations to determine if the origin of the new HI feature near IC 10 was due to an IC 10-M 31 interaction. Their results show that the HI extension is inconsistent with the trailing portion of the orbit, making it unlikely that an M 31-IC 10 tidal interaction can explain the origin of this feature. We will explore this further in Section 4.5.

The majority of published HI synthesis observations on IC 10 discuss the disturbed morphology and kinematics of this galaxy based on observations only. The orbital simulations done by Nidever et al. (2013) focused on the origin of the new HI feature and not on the entire disturbed morphology of IC 10. To advance our understanding on possible mechanisms responsible for the observed HI structure of IC 10, we have combined new HI observations with the DRAO with simulations. The DRAO observations allow us to study the extended HI morphology and kinematics while the simulations provide detailed investigation of possible interactions between IC 10 and M 31. The outline of this paper is as follows. In Section 4.2 we discuss the observations and data reduction. In Section 4.3 we present the results of the HI distribution of IC 10. In Section 4.4 we discuss the tilted ring and mass model results of the main disk of IC 10. Then in Section 4.5 we provide simulations to see if M 31 could be responsible of the outer HI structure of IC 10. The summary and conclusions of this work are given in Section 4.6.

4.2 DRAO observations and data reduction

The primary observations for this study were made in the 21 cm line of neutral hydrogen with the Synthesis Telescope at the DRAO. This telescope is an East-West

Table 4.1: Basic parameters of IC 10

Parameter	
Morphology	BCD[b]
Right ascension (J2000)	00:20:24.6[a]
Declination (J2000)	+59:17:30.0[a]
Distance (Mpc)	0.7[e]
M_V (Mag)	-16.3[e]
α^{-1} (kpc)	0.40 ± 0.01[d]
$V_{heliocentric}$ (km s^{-1})	-348.0[c]
Optical PA$^{(\circ)}$	-38.0[e]
Optical inclination$^{(\circ)}$	41.0[e]
Total HI mass ($M_\odot$)	8.0 $\times 10^{7}$[c]
A_V (mag)	4.3[f]
Galactic latitude($^\circ$)	118.95[g]
Galactic longitude($^\circ$)	-3.33[g]

Notes. Ref(a) de Vaucouleurs et al. (1991a); (b) Richer et al. (2001); (c) Ashley et al. (2014); (d) Hunter & Elmegreen (2006); (e) Hunter et al. (2012); (f) Schlegel et al. (1998); (g) Kim et al. (2009)

Table 4.2: DRAO Synthesis Telescope observational set-up

Obs. data	Field center coordinates J2000	Beam parameter $\theta_{maj}('') \times \theta_{min}('')$	1-σ Noise at field center (mJy/beam)
20 Feb., 1997	0:20:23.1, +59:19:08.4	67.48 × 58.98	12.3
9 Sept., 2017	0:20:17.3, +59:14:14	67.63 × 59.13	12.5
9 Sept., 2017	0:20:17.3, +59:22:14.0	68.18 × 59.98	13.1
1 Oct., 2018	0:22:28.0, +60:25:09.0	66.19 × 59.11	13.0

Table 4.3: Observational parameters of the DRAO observation of IC 10 for full resolution mosaic

Parameter	Value
Total length of observation	432 hrs
Frequency center of band	1422.0643 MHz
Number of velocity channels	256
synthesized beam	$59'' \times 68''$
Velocity resolution	2.64 km s^{-1}
Number of spatial pixels	1024
Pixel angular size	$18''$
1σ RMS noise (single channel)	1 Kelvin (6.6 mJy/beam)
Measured 3σ column density over 16 km s^{-1}	4×10^{19}cm^{-2}

interferometer consisting of seven small (~9 m diameter) dishes spaced variously across a maximum baseline of 617.2 m. This longest baseline achieves a synthesized half-power beamwidth of $49''$(EW) $\times 49''/\sin\delta$(NS) with uniform weighting, although in the HI line we chose natural weighting (a Gaussian taper in the u,v plane) to increase the sensitivity at the slight expense of resolution ($58'' \times 58''/\sin\delta$). Further specifications and capabilities of the DRAO can be found in Landecker et al. (2000) and Kothes et al. (2010). Other observing frequencies of IC 10 were in a 30 MHz continuum band centered at 1420 MHz (λ = 21 cm), and a 2 MHz band at 408 MHz (λ = 74 cm). The telescope also produces fully calibrated and instrumental corrected Stokes U,Q,V polarization maps, observed in four 7.5 MHz-wide sub-bands centred on 1420 MHz; however the radio polarization and continuum data for IC 10 are not

presented here.

Two full synthesis fields were observed centered on IC 10 (12 hours per set of spacings times 12 days). The spectrometer was set to a 2 MHz-wide band in the line with 256 channels, each spaced by Δv =1.65 km s^{-1} per channel. The band was centered on a heliocentric velocity of $v_{\rm HEL} = -350$ km s^{-1}. The synthesized beam of these observations is $59'' \times 68''$, and the velocity resolution is 2.64 km s^{-1}. These resolution parameters give a typical 1σ-RMS noise in each (empty) channel of 1.5-1.7 K. To increase sensitivity to the extended HI disk of IC 10, another full-synthesis field with the same pointing centre was obtained from the DRAO archive (observed in 1997) and a fourth field was observed with a pointing 1-degree North of IC 10 to search for a possible satellite galaxy. Table 4.2 lists the field centers for the four individual fields (in J2000.0 coordinates).

Prior to mosaicking the four fields together, we perform standard data processing steps on each developed for the Canadian Galactic Plane Survey (described in Taylor et al., 2003). Channels that are free of line-emission are averaged at both the low and high velocity ends of the band to produce continuum-only maps, and a map that is linearly-interpolated from these two ends is subtracted from each channel in the data cube. To calibrate the flux scale of each continuum-subtracted cube, we compare point sources in the mean of both continuum end-channel maps to those in the 30 MHz continuum map of each field (these maps are first CLEANed around the stronger sources). The observed 30 MHz wide continuum maps are flux calibrated against several strong sources observed by the ST (e.g. 3C 48, 3C 286; see Table 1 of Taylor et al., 2003, for sources and fluxes). An error-weighted mean of the flux ratio $S_{1420cont}/S_{HIcont}$ for all point-sources above a cutoff level (20 mJy beam^{-1}) is obtained; this sample is further trimmed by rejecting sources $\pm 2\sigma$ away from the mean. Typically, 20-30 sources remained in the sample for each field. The uncertainty in the flux calibrated this way is $\sim$5%.

Each synthesis field is trimmed to the half-power width of the primary beam of the individual antennae ($107' \times 107'$), and the four fields were mosaicked together with weighting proportional to the inverse of their RMS noise. The final step was to recover missing spatial structures (aka "short-spacings") that the DRAO is not sensitive to (larger than about $45'$). We use the Effelsberg HI Survey Winkel et al. (2016), a single-dish survey with a beam of 10.82 arcminutes. The measured 1σ noise at the centre of the final short-spacings-added mosaic is ± 1 K per (empty) channel for the full resolution of $59'' \times 68''$. Table 4.3 shows the parameters for the final mosaic cube of IC 10.

4.3 HI distribution and kinematics of IC 10

The HI maps of IC 10 were created using the HI source finding algorithm, SoFiA (Serra et al., 2015). The ability of SoFiA to search for emission on multiple scales while taking into account artifacts and variations in noise allow us to deal with the complex HI structure of IC 10 with much ease. The smooth + clip source detection algorithm was used to search for emission by setting a detection limit of 2σ which corresponds to a column density limit of 10^{19} cm^{-2}. A detailed description of this software and how it is used is given in Serra et al. (2015).

4.3.1 The HI global profile

The HI global profile, derived from a primary beam corrected data cube is presented in Figure 4.1. We compare the DRAO global profile to the GBT (Nidever et al., 2013) and VLA LITTLE THINGS (Hunter et al., 2012) global profiles. The resulting profile is asymmetric with more HI around the southern extension (~-300 km s^{-1} to -250 km s^{-1}) where the HI is on scales > 15′ not seen by the VLA. From the profile, a mid-point velocity of -339 ± 6 km s^{-1} at 50% level is found, which is a better representation of the systemic velocity than the intensity weighted mean because of the asymmetry of the profile. This value is comparable to the value of -338 km s^{-1} found by Nidever et al. (2013). The profile widths calculated at the 20 and 50 per cent levels of the peak flux density are ΔV_{20} = 96 ± 3 km s^{-1} and ΔV_{50} = 61 ± 3 km s^{-1}. A total flux of 675 ± 6 Jy km s^{-1} is estimated from the global profile. The total HI mass is calculated as

$$M_{HI} = 2.36 \times 10^5 \Big(\frac{D}{\mathrm{Mpc}}\Big)^2 \int \mathrm{FdV} \tag{4.1}$$

where $\int$FdV is the source total flux in units of Jy km s^{-1} and D is the distance in Mpc. Adopting a distance of 0.7 Mpc (Hunter et al., 2012), a total HI mass of (7.8 ± 0.07)× 10^7 M$_\odot$ is calculated. This mass is larger by ~ 36% than the value of (5 ± 0.046) ×10^7 M$_\odot$ measured from the VLA data (Ashley et al., 2014) and is smaller by ~ 1% than the value of (7.9 ± 0.08) ×10^7 M$_\odot$ measured from the GBT data (Nidever et al., 2013). All masses are calculated using our adopted distance. This result shows that no flux has been missed by the DRAO observations. This is because the compact configuration of DRAO is sensitive to extended HI emission that is missed by the VLA and detected with the single dish GBT.

4.3.2 HI distribution

The HI intensity map extracted from the natural weighted HI data cube is shown in Figure 4.2(a). As has been seen in previous HI interferometric observations (Shostak & Skillman, 1989; Wilcots & Miller, 1998; Ashley et al., 2014), the HI distribution of IC 10 is characterized by several distinct HI features. These features include a

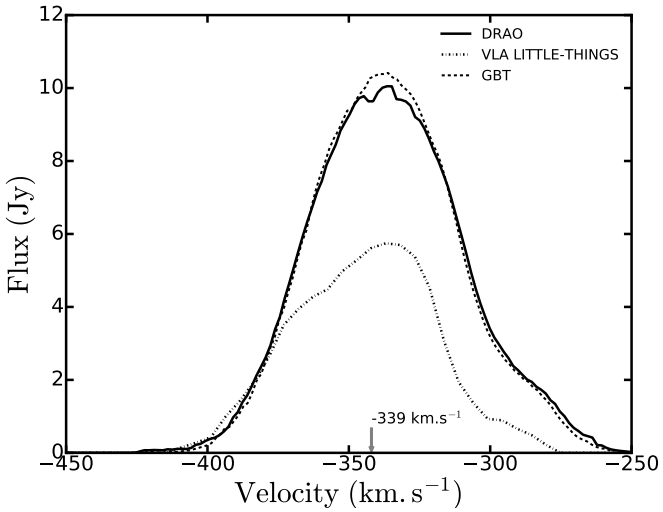

Figure 4.1: Comparison of the HI global profile of IC 10 from the DRAO map (solid line, this work), from the VLA LITTLE THINGS (dash-dotted line, Hunter et al. (2012)), and from the GBT map (dotted line, Nidever et al. (2013).

southern plume, a rotating arm, and spurs north-west and north-east of IC 10. It is important to note that although all these features were previously reported, the DRAO observations are sensitive to large scale structures and detect these features out to a much larger extent. For instance, the last VLA HI observations of IC 10 measure the southern plume out to 17′ (Hunter et al., 2012) while our DRAO observations measure this feature out to 32′. Figure 4.3 shows the total column density map of the central parts of IC 10 superposed on a WISE 3.4 μm band map, which is sensitive to light from the old stellar populations. The brightest HI peak coincides with the stars.

4.3.3 HI kinematics

The velocity field and dispersion maps of IC 10 are shown in Figure 4.2(b) and 4.2(c) respectively. As noted in previous HI observations, IC 10 is characterized by a distorted velocity field. The southern plume is seen to have velocities different from the rest of the galaxy. A closer look at the central region of the velocity field map shows that the central disk of IC 10 behaves like a rotating disk (see below, Figure 4.7(a)). On the other hand, the spurs and the southern plume are counter-rotating with respect to the central disk. The v elocity dispersions of IC 10 vary from ~ 10 km s^{-1} to ~ 35 km s^{-1}. High velocity dispersions are seen in regions where different velocity structures meet with each other (Figure 4.2(b)). This indicates that the southern plume, the west and east extensions are probably accreting on the main body of IC 10 as suggested by Wilcots & Miller (1998), and this could explain the recent starburst that occurred ~ 10 Myr ago in IC 10 (Richer et al., 2001).

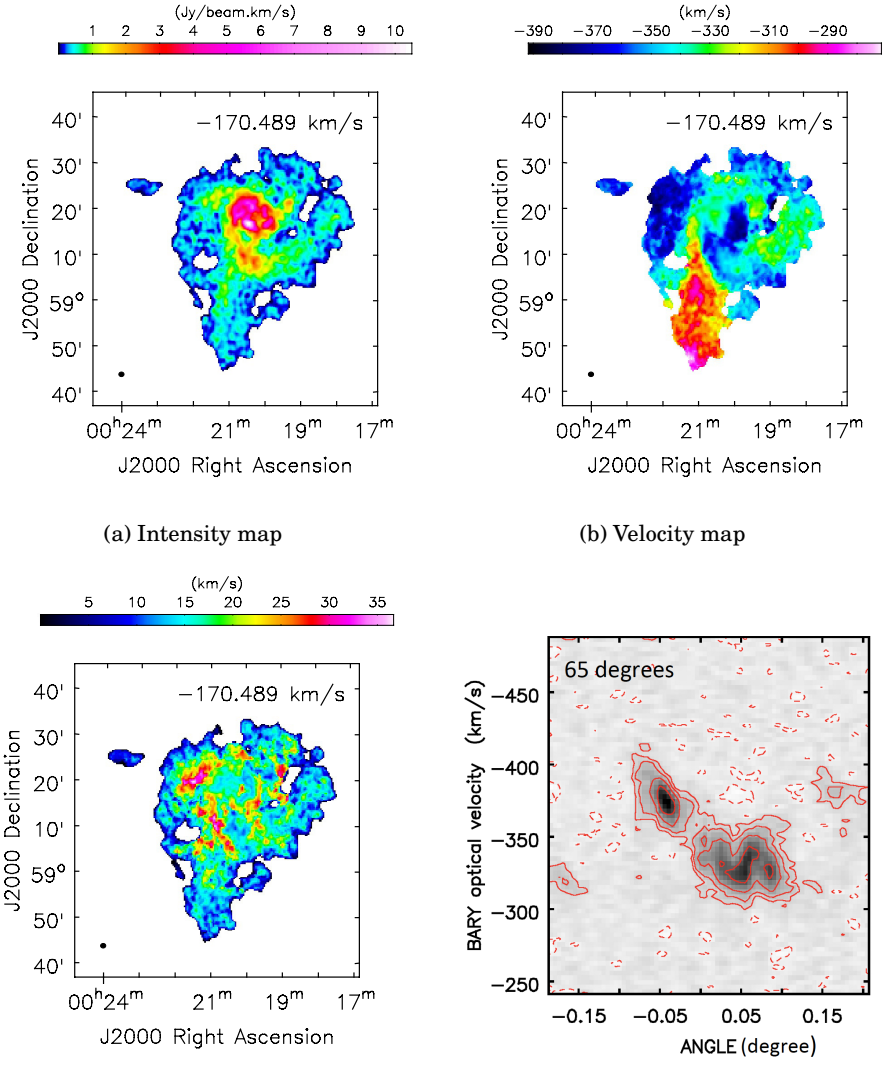

(a) Intensity map

(b) Velocity map

(c) Dispersion map

(d) PV diagram

Figure 4.2: Moment maps of IC 10 created using the SoFiA software. Figure 4.2(a) shows the intensity map, Figure 4.2(b), the velocity field map, Figure 4.2(c) is the dispersion map, and Figure 4.2(d) is the position-velocity diagram of IC 10 along the major axis.

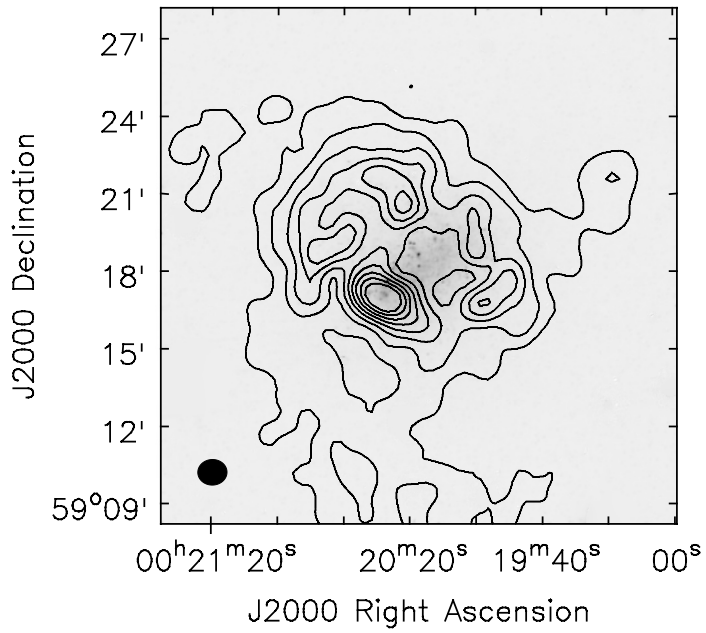

Figure 4.3: Integrated HI column density contours of IC 10 from the DRAO data overlaid on a WISE 3.4 μm map. The HI column density contours are at 1, 2, 3, 4, 5, 6, 7, and 8 × 10^{20} cm^{-2}. The synthesized beam is shown in the bottom left corner.

4.3.4 GBT new HI feature of IC 10

One of the aims of this study was to verify the existence of a new faint 21 cm HI feature discovered in the GBT observations detected at a column density N_{HI} ~ 2.5 × 10^{17} cm^{-2} (Ashley et al., 2014). This feature is not observed in the Effelsberg 21 cm survey (EBHIS) data, (see Figure 4.4). While the Effelsberg data is 3 times less sensitive than the targeted GBT observations we compare it to, it is a similar class telescope to the GBT. Thus, its failure to detect it begs the question whether the observed feature is real or is an artifact of GBT data. Verifying whether this feature is real or not is crucial for our interpretation of the HI data of IC 10. If this feature is an HI cloud it could explain the very disturbed and highly extended HI disk of IC 10 (through possible interaction, including tidal stripping and merging). If it is a new satellite galaxy of IC 10, the intermediate spatial resolution of DRAO will allow us to explore its kinematics and distribution, and look for more such clouds around IC 10. Analysis of the HI cubes from the DRAO and Effelsberg data fails to detect any such feature. The feature should roughly have a signal to noise of 3 in the Effelsberg data, taking into account that the GBT and Effelsberg have the same beam size. However, there is absolutely no trace of any emission signal in the

direction and velocity range of the reported feature. Taking into account that the Effelsberg and DRAO data are less sensitive than the GBT observations, additional observations which are currently underway will be necessary to verify if this feature is real or not.

4.4 Central HI disk of IC 10

From the velocity field map in Figure 4.7(a), it is clear that the central region of IC 10 is a regularly rotating disk. In that sense, the rotation velocities of this region can be determined. To separate the main disk from the rest of the galaxy, we first created regions in each channel around emission perceived to be associated with the disk (based on morphology and velocity). From this, a new cube consisting of only the selected emission was created. The MOMNT task in AIPS was used to derive the moment maps of the central part of IC 10. A second check in determining the extent of the central region was done using the dispersion map. For a regularly rotating disk, we expect the dispersion velocities to be high at the center and decrease uniformly with increasing radius. Using this approach, a mask was created around the velocity dispersion map excluding outer regions showing non-uniform dispersion values. This region was then applied to the intensity and velocity field maps. The final intensity, velocity field, and dispersion map of the central disk of IC 10 are shown in Figure 4.7(d), 4.7(a) and 4.7(e). A total flux of 196.2 ± 2.3 Jy km s^{-1} is measured from the intensity map, corresponding to an HI mass of (2.300 ± 0.026) × 10^7 $M_\odot$ adopting a distance of 0.7 Mpc. This corresponds to ~ 33% of the total HI mass of the complex. The dispersion velocities of the central region vary from ~ 30 km s^{-1} in the inner regions to ~ 10 km s^{-1} in the outer regions.

4.4.1 Tilted-ring modeling

We modeled the kinematics of the central part of IC 10 using the velocity field map shown in Figure 4.7(a). The rotation curve was derived by means of a tilted-ring model. The tilted ring model assumes that the gas rotates as a set of concentric rings, and that each ring can be described by the following dependent quantities: rotation velocity (V_{rot}), the systemic velocity (V_{sys}), the central position of the ring (x,y), the inclination (i), and the position angle (PA). The line of sight velocity at any position V(x,y) on a ring can be expressed as

$$V(x,y) = V_{sys} + V_{rot}\sin(i)\cos(\theta) \tag{4.2}$$

where θ is an angle from the major axis of the galaxy plane and is related to the PA by the following relation:

$$\cos(\theta) = \frac{-(x-x_0)\sin(\mathrm{PA}) + (y-y_0)\cos(\mathrm{PA})}{r}, \tag{4.3}$$

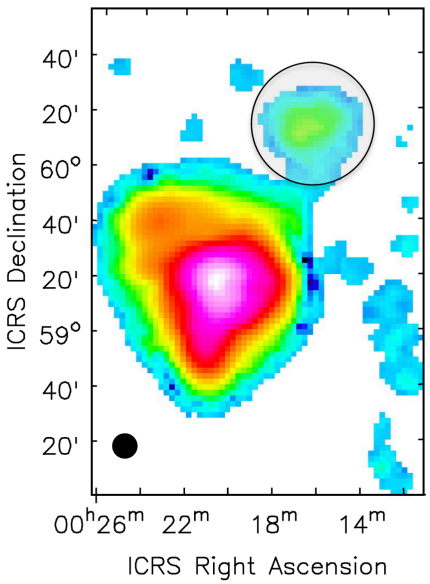

(a) GBT integrated map of IC 10

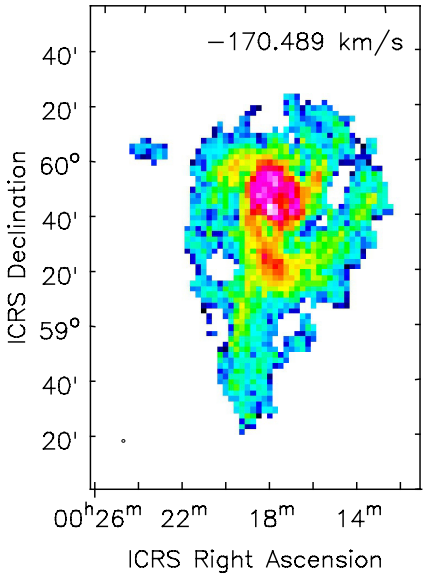

(b) DRAO integrated map of IC 10

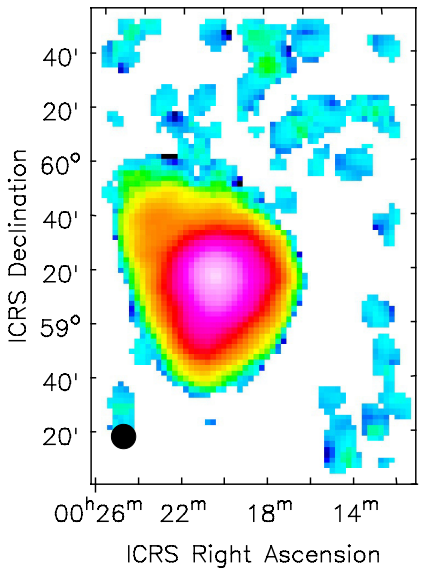

(c) Effelsberg integrated map of IC 10

Figure 4.4: Comparison between the GBT, DRAO and Effelsberg map of IC 10. The extended new faint HI feature reported in the GBT observation is shown by the black circle.

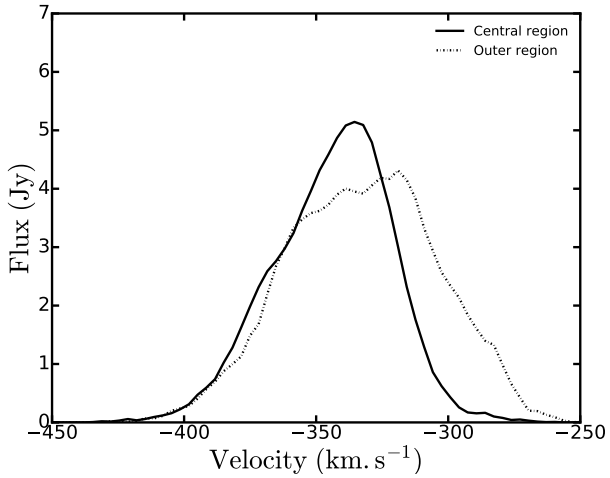

Figure 4.5: Comparison of the HI global profile of IC 10 central region (solid line) and the outer region of IC 10 (dash-dotted line).

$$\sin(\theta) = \frac{-(x - x_0\cos(\mathrm{PA})) - (y - y_0\sin(\mathrm{PA}))}{\mathrm{rcos(i)}} \tag{4.4}$$

where r is the radius of the ring in the galaxy plane. The GIPSY task ROTCUR (Begeman, 1989) was used to fit tilted ring models to the HI velocity field along rings that are spaced by half the spatial resolution, i.e, 32″ in this case. A $|\cos\theta|$ weighting function and an exclusion angle of ± 10° about the minor axis were applied to the data points to give less weight to pixels close to the minor axis. First, we carried out ROTCUR with all initial parameters kept free (PA, i, x, y, V_{sys}, and V_{rot}). Assuming that the kinematical center and V_{sys} do not vary from ring to ring, their mean values were determined from the first model and kept fixed throughout the fitting process. Different iterations were made either keeping PA or inclination or both fixed to determine the best fit model. After obtaining a satisfactory model for both sides, we made ROTCUR models of the approaching and receding sides separately.

4.4.2 Results of the tilted ring fit

The results of the tilted ring model to the velocity field are shown in Figure 4.6 and 4.7. The resulting kinematical parameters are presented in Table 4.4. The HI rotation curve of the central disk of IC 10 is measured out to 0.81 kpc. The rotation curve of IC 10 is similar in form to those of other dwarf galaxies (Namumba et al., 2017), having a linearly rising (solid body) inner portion and then turning over to become approximately flat. On the other hand, the slope of the inner part of IC 10 is ∼ 3 times steeper (65 km s^{-1}/kpc) than what has been derived for most dwarf galaxies. Namumba et al. (2017, 2018) calculates the inner slopes of 21, 21, and 13

km s^{-1}/kpc for NGC 6822, Sextans A and B while Meurer et al. (1996) and Meurer et al. (1998) derive the inner slopes of 25 km s^{-1}/kpc and 22 km s^{-1}/kpc for BCD galaxies NGC 2915 and NGC 1705. We find the kinematical V_{sys} = -351 ± 1.8 km s^{-1}, this value is different from the V_{sys} of -339 ± 6 km s^{-1} derived from the global profile due to the asymmetry. A mean PA = 65 ± 4 ° and i = 47 ± 6 ° are found. These values are in agreement with the results of Oh et al. (2015). Oh et al. (2015) measured V_{sys} = -348 km s^{-1}, PA ~ 60°, and i ~ 48°. Shostak & Skillman (1989) measured a V_{sys} = -352 km s^{-1} and slightly lower values of i = 40° and PA = 50°. Figure 4.9 compares the IC 10 DRAO rotation curve with the rotation curve derived by Oh et al. (2015) from high resolution VLA LITTLE THINGS data. The two curves agree well within the errors.

To check the reliability of our derived kinematical parameters, we built a model velocity field (4.7(b)) using the best-fitting values and compared this to the observed velocity field (Figure 4.7(a)). The two maps agree well with small deviations. The residual map (Figure 4.7(c)), which is the difference between the observed and the model velocity field does not show any large scale deviations which implies that the derived velocity field model is in good agreement with the observed velocity field. The mean value of the residual map is 1.0 km s^{-1} with a rms spread of 6.2 km s^{-1}. The residual velocity field shows some large scale structure in the sense that the south-east part shows negative residuals and the north and west parts predominantly positive residuals which are consistent with the velocity field in Figure 4.7. This indicates that the inner disk could be associated with non circular motions. 4.8 shows the rotation curve overlaid on a position-velocity (PV) diagram obtained along the major axis.

The errors on the final rotation curve are calculated as the quadratic sum of the dispersion in each ring and half the difference between the approaching and receding sides:

$$\Delta V = \sqrt{\sigma^2 + \left(\frac{|V_{app} - V_{rec}|}{2}\right)^2} \tag{4.5}$$

We take into account random motions by correcting the derived rotation velocities for the asymmetric drift. Following the procedure used by Côté et al. (2000), the corrected rotation velocities are given by:

$$V_c^2 = V_{rot}^2 - 2\sigma \frac{\delta\sigma}{\delta \ln R} - \sigma^2 \frac{\delta \ln \Sigma}{\delta \ln R} \tag{4.6}$$

4.4.3 Mass modeling

The rotation velocity is a direct reflection of the gravitational potential of the galaxy, and can therefore be used to derive the total distribution of matter. The gravitational

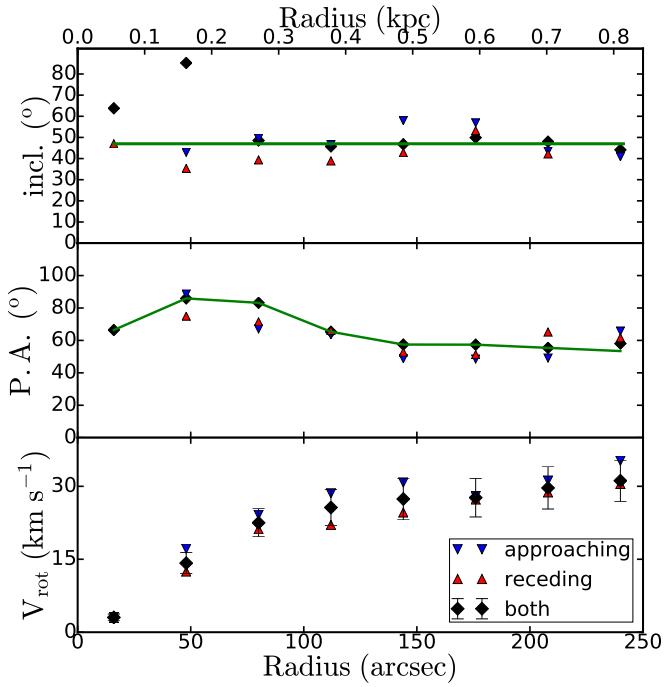

Figure 4.6: Results of the tilted ring fit of IC 10. The top panel shows the inclination, the middle panel the major axis position angle, and the bottom panel shows the final rotation curves. Red upward triangles are the results of the receding side, blue downwards triangles for the approaching side, and the black diamonds represent both sides. The green solid lines are the adopted values used to derive the final rotation velocities.

Table 4.4: Radial HI distribution and kinematical parameters of IC 10.

Radius	Σ_g	σ	V_{rot}	ΔV	V_{corr}	V_c
arcsec	$M_\odot pc^{-2}$	km s^{-1}	km s^{-1}	km s^{-1}	km s^{-1}	km s^{-1}
0.0	9.4	13.7	0.0	0.0	0.0	0.0
16	9.1	13.2	3.0	0.7	1.8	4.9
48	9.3	12.8	14.2	3.2	0.6	14.8
80	9.9	12.4	22.5	3.2	0.3	22.8
112	9.7	12.5	25.6	4.8	0.8	26.4
144	9.0	12.7	27.4	5.3	0.7	28.1
176	8.8	12.4	27.6	3.9	2.1	29.7
208	9.7	13.3	29.7	4.5	3.8	33.5
240	10.6	13.2	31.1	4.8	2.3	33.4

Notes. Column (1) gives the radius, column (2) the surface densities, column (3) the velocity dispersion, column (4) the observed rotation velocities, column (5) the errors of those velocities, column (6) correction from asymmetric drift, and column (7) the corrected velocities used for the mass models.

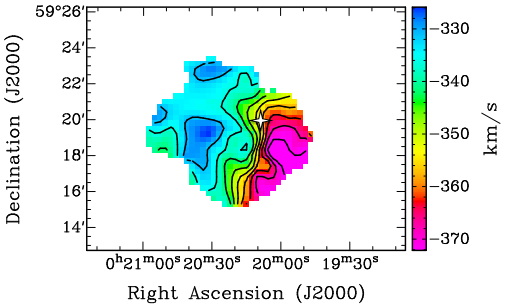

(a) Observed velocity field

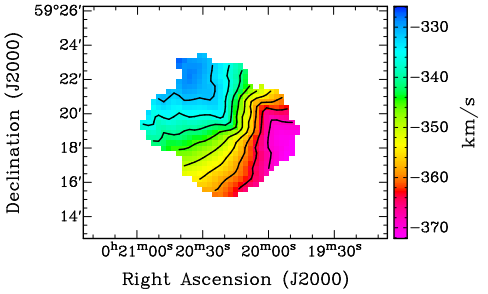

(b) Model velocity field map

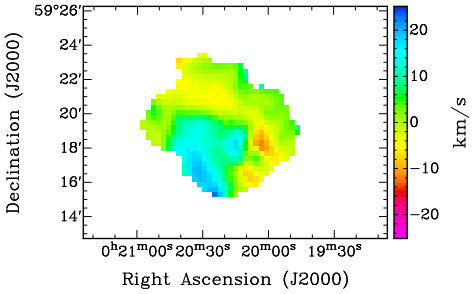

(c) Residual map

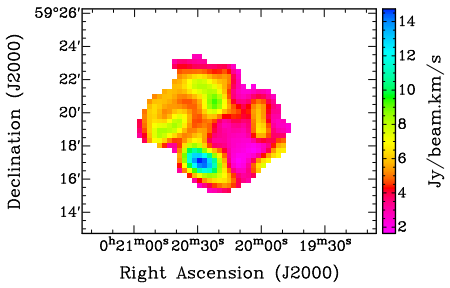

(d) Intensity map

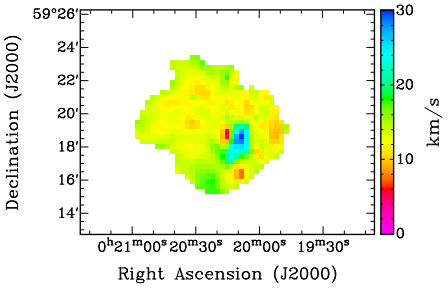

(e) Velocity dispersion map

Figure 4.7: Maps of the central disk of IC 10: Observed velocity field 4.7(a), model velocity field map 4.7(b), residual map 4.7(c), intensity map 4.7(d), and velocity dispersion map 4.7(e). The observed and model velocity field contours run from -370 to -330 km s^{-1} in steps of 5 km s^{-1}. The white star in Figure 4.7(a) represents the position of the kinematical center.

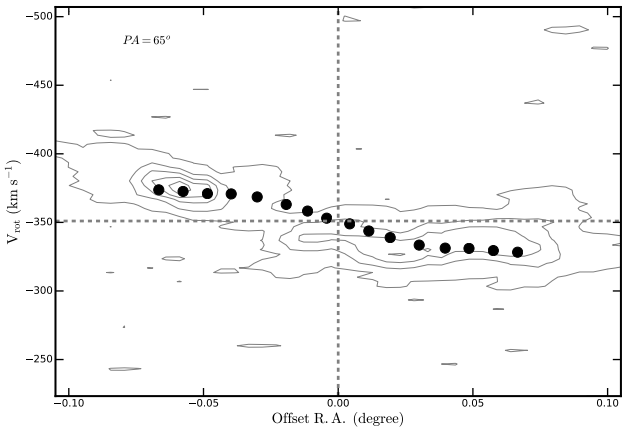

Figure 4.8: Position velocity diagram of IC 10 central regions with the projected rotation curve over plotted. The dotted grey lines represent the centre of the galaxy and the systemic velocity. Superimposed is the rotation curve derived from the tilted ring model, corrected for the inclination of a slice along the galaxy major axis.

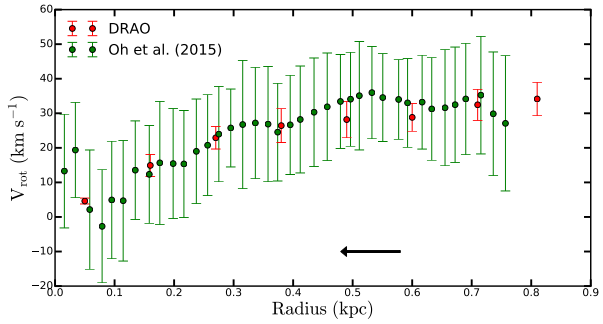

Figure 4.9: Comparison of the IC 10 DRAO rotation curve (red circles) with the analysis by Oh et al. (2015) (green circles). The black arrow indicates the region used in the Oh et al. (2015) analysis.

potential is the sum of the individual mass components in each galaxy. Expressed in velocities, this sum becomes:

$$V_{\rm rot}^2 = V_g^2 + V_d^2 + V_h^2 \tag{4.7}$$

with $V_{\rm rot}$ being the observed total rotation velocity, V_g the contribution of the gas disk to the total rotation curve, V_d the contribution of the stellar disk and V_h the contribution of the dark matter halo component.

4.4.3.1 Stellar and gas component

The contribution of the gaseous disk was computed using the HI surface density profile shown in Figure 4.10. The profile was derived from the HI column density

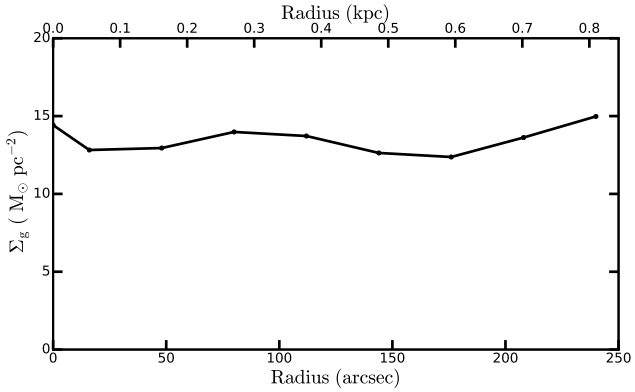

Figure 4.10: HI surface density profile of IC 10 derived from GIPSY task ELLINT.

map using a GIPSY task ELLINT and applying the kinematical parameters derived from the tilted ring fit. The HI surface distribution was then multiplied by a factor of 1.4 to account for helium and other metals. The gas surface density profile were then converted to the corresponding gas rotation velocities assuming the gas component is mainly distributed in a thin disk. This was done using the GIPSY task ROTMOD. We used the WISE 3.4 μm surface brightness profile to derive the stellar rotation velocities. The 3.4 μm WISE band traces light from the old stellar population and therefore is an effective measure of stellar mass. The surface brightness profile in mag arcsec^{-2} was converted into luminosity density profile in units of $L_\odot$ pc^{-2} and then to mass density using the expression

$$\Sigma[M_\odot pc^{-2}] = (M/L)_{*,3.4} \times 10^{-0.4\times(\mu_{3.4}-C_{3.4})} \tag{4.8}$$

where $\mu_{3.4}$ is the stellar brightness profile, $(M/L)_{*,3.4}$ is the mass to light ratio in the 3.4 μm WISE band, and $C_{3.4}$ is the constant used for conversion from mag arcsec^{-2} to $L_\odot$ pc^{-2} and is calculated as $C_{3.4} = M_\odot + 21.56$. $M_{\odot 3.4} = 3.24$, is the absolute magnitude of the Sun in the 3.4 μm WISE band. The mass to light ratio was calculated based on the stellar distribution models using the (W1-W2) color. Using the method of Cluver et al. (2014), the $M/L_{3.4}$ at 3.4 μm is given by

$$\log_{10} M_{\rm stellar}/L_{\rm W1} = -1.93(W_{3.4\mu m} - W_{4.6\mu m}) - 0.04 \tag{4.9}$$

with (W1-W2) = 0.08, a mass to light ratio of 0.6 is derived for IC 10. However, Equation 4.9 may not be usable for certain dwarf galaxies with bluer colors.

4.4.3.2 Dark matter models

We have considered two different models to study the properties of dark matter in IC 10: the Navarro Frenk and White (NFW) (Navarro et al., 1997) (NFW) and the pseudo-isothermal (Begeman et al., 1991) (ISO) models. The NFW profile is derived from the results of dark matter only cosmological simulations performed within the

frame of the ΛCDM theory. The density $\rho_{\rm NFW}$ is given by

$$\rho_{\rm NFW}(r) = \frac{\rho_s}{\Big(r/r_s\Big)\Big(1+r/r_s\Big)^2}, \tag{4.10}$$

where ρ_s and r_s are the characteristic density and scale radius of the NFW halo. The NFW halo rotation curve is given by

$$V(r) = V_{200}\Big[\frac{\ln(1+cx) - cx/(1+cx)}{x[\ln(1+c) - c/(1+c)}\Big]^{1/2} \tag{4.11}$$

where c = r_{200}/r_s is the concentration parameter, x = r/r_{200}, and V_{200} is the characteristic velocity. The radius r_{200} is the radius where the density contrast with respect to the critical density of the universe exceeds 200, roughly the virial radius.

The ISO model results from the shape of the observed rotation curves, and models the halo as a central constant-density core. The form of this core-like halo is given by:

$$\rho_{\rm ISO}(r) = \frac{\rho_0}{1+\Big(r/r_c\Big)^2} \tag{4.12}$$

where ρ_0 is the central density and r_c is the scaling radius. The corresponding halo rotation curve is given by

$$V(r) = 4\pi G\rho_0 r_c^2\Big[1 - \frac{r_c}{r}\arctan\Big(\frac{r}{r_c}\Big)\Big] \tag{4.13}$$

4.4.3.3 Mass modeling results

The results of the mass modeling of IC 10 are summarized in Figure 4.11 and Table 4.5. The GIPSY task ROTMAS was used to decompose the observed rotation curve into luminous and dark matter components. The inverse squared weighting of the rotation curve data points with their uncertainties were used during the fitting. The M/L value of 0.6 derived from Equation 4.9 was too large to fit the stellar component of IC 10, therefore we used the best fitting model by letting M/L freely vary. It can be seen from Figure 4.11 that the ISO model reproduces better the observed rotation curve of the inner disk of IC 10 with a reduced χ^2 value of 1.0. However, a M/L of 0.04 ($\sim$ 15 times smaller than predicted from the WISE infrared color) derived from this fit is too small to make physical sense. On the other hand, the NFW fit gives a reduced χ^2 value of 1.6. The difference between the two models is seen in the inner most part where the ISO model fits better than the NFW model. The large errors derived for the NFW fitted parameters (see Table 4.5) suggest that this model does not produce a good fit to the observed rotation curve. Moreover, the value of the concentration parameter c found is unphysical: c = 1 means no

Table 4.5: Results for the Mass Models of IC 10. The densities have the units of $10^{-3} M_{\odot} pc^{-3}$ and the radii are in units of kpc.

Model	values			
ISO	Υ_*	r_c	ρ_0	χ^2_{red}
	0.04 ± 0.04	0.21 ± 0.03	476.33 ± 230.02	1.00
NFW	Υ_*	c	R_{200}	χ^2_{red}
	0.11 ± 0.02	0.03± 186.95	852.42 ± 205987.91	1.60
no-DM	Υ_*			χ^2_{red}
	0.17 ± 0.08			2.2

collapse and c < 1 is impossible in the ΛCDM context (de Blok et al., 2008). The bottom panel of Figure 4.11 shows the results of the mass model fit without a dark matter component. Although a larger χ^2 value of 2.2 is derived, it is clear that the kinematics of the inner disk of IC 10 can be reproduced without the need of a dark matter halo. In this case, a M/L of 0.17 ± 0.08 is obtained. This value is closer to a M/L of 0.2 expected at the lower end for most dwarf galaxies as derived by Lelli et al. (2016). It is important to note that this result does not exclude the possibility that dark matter may be present on larger scales in IC 10.

Oh et al. (2015) derived their mass model fit of IC 10 using high resolution VLA data. By fitting the inner disk out to $\lesssim$ 0.57 kpc (see black arrow in Figure 4.9), they derived lower χ^2 values of 0.23 and 0.07 for the NFW and ISO resepctively with the stellar component dominating the gravitational potential at most radii. The differences between our results and that of Oh et al. (2015) may arise from the different radii used during the fits, taking into account that the shape of the outer rotation curve contributes to the outcome of the mass model results. Comparing with the results of other BCDs from the literature, Lelli et al. (2012a) and Lelli et al. (2012b) showed that baryons may dominate the gravitational potential in the inner regions of UGC 4483 and I ZW 18, with the stellar component contributing ~ 50% of the observed rotation curve of UGC 4483. This could suggest, as from our result of IC 10, that the kinematics of the inner disks of most BCDs can be described without a dark matter halo.

4.5 Simulations

The origin of the stream-like features seen in IC 10 has been widely discussed (see Nidever et al. (2013); Ashley et al. (2014) and references therein). In general, these discussions focus on whether they are caused by an interaction with M 31 or whether they arise from dwarf-dwarf interactions or some other trigger. We have focused on

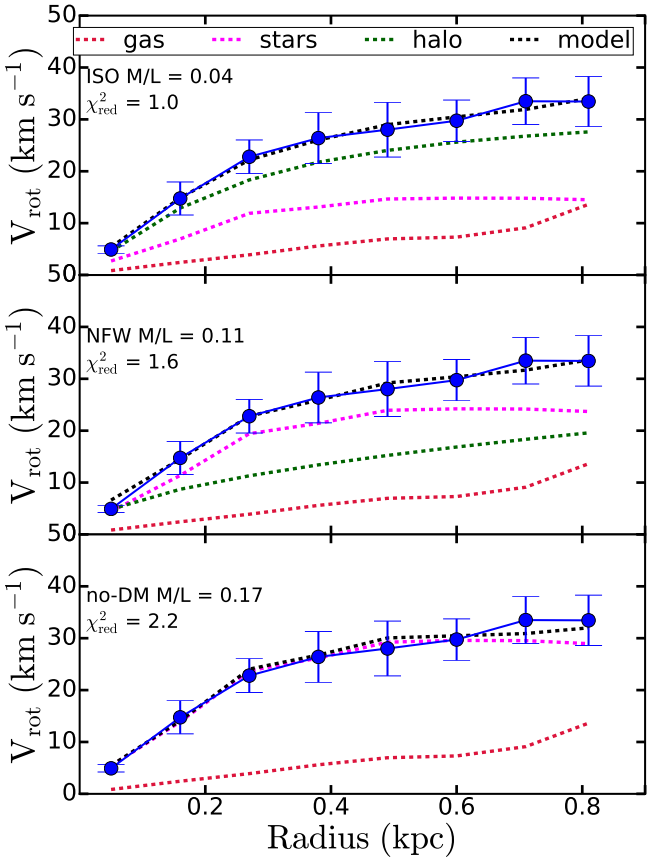

Figure 4.11: Mass distribution models of IC 10 with ISO (top panel), NFW (middle panel) and no dark matter halo (bottom panel). The blue filled circles present the observed rotation curve, the black dotted lines the model rotation curve, the darkgreen dotted lines indicate the dark matter rotation velocities, the crimson dotted lines show the gas rotation velocities, and the magenta dotted lines show the rotation velocities of the stellar components.

the possibility of an interaction with M 31 using a suite of tailored simulations.

The parameter space of the IC 10-M 31 system is quite large. It includes the individual galaxy properties as well as the relative geometry between the two systems. While the system has been studied in detail, the uncertainties in these parameters allow for quite different orbital histories. In this work we have focused on the effects of uncertainties in IC 10's proper motions. For simplicity, we run nine simulations, where the only difference is the proper motion vector. While these are representative of the orbits allowed by IC 10's tangential motion, it is important to be cautious when interpreting the results of these simulations.

We have generated the initial conditions (ICs) for each galaxy using the GALACTICS code (Kuijken & Dubinski, 1995; Widrow et al., 2008; Deg et al., 2018). The version of the code given in Deg et al. (2018) can generate equilibrium models with a bulge, two stellar disks, a gas disk, and a dark halo. Once the ICs for M 31 and IC 10 are determined, the combined system is evolved using the GADGET-2 smoothed particle hydrodynamics code (Springel, 2005).

4.5.1 Models

The GALACTICS code generates equilbrium models using a Sérsic bulge, two exponential stellar disks, an exponential gaseous disk, and a double power law halo. Prugniel & Simien (1997) found that the density that gives rise to a Sérsic profile is

$$\rho_b(r) = \rho_{0,b}\left(\frac{r}{r_b}\right)e^{\left[-b\left(\frac{r}{r_b}\right)^{1/n}\right]}, \tag{4.14}$$

where r is the spherical radius and $p = 1 - 0.6097/n + 0.05563/n^2$. However, GALACTICS parameterizes the bulge with a scale velocity, σ_b, given by

$$\sigma_b = [4\pi n b^{n(p-2)}(n(2-p))r_b^2\rho_b]^{1/2}. \tag{4.15}$$

The exponential stellar disks have a density of

$$\rho_d(R,z) = \frac{M_d}{4\pi R_d^2 z_d}e^{(-R/R_d)}\mathrm{sech}^2(z/z_d)C(R;R_t,\delta R_t), \tag{4.16}$$

in cylindrical coordinates where M_d is the disc mass, R_d is the disc scale length, z_d is the disc scale height, and $C(R;R_t,\delta R_t)$ is a truncation factor given by

$$C(R;R_t,\delta R_t) = \frac{1}{2}\mathrm{erfc}\left(\frac{R-R_t}{\sqrt{2}\delta R_h}\right). \tag{4.17}$$

The double-power law halo density is

$$\rho(R) = \frac{2^{2-\alpha}\sigma_h^2}{4\pi r_h^2}\frac{1}{u^\alpha(1+u)^{\beta-\alpha}}C(r;r_t,\delta r_t)\ , \tag{4.18}$$

where σ_h is a scale velocity, $u = r/r_h$, r_h is a scale radius, α and β are the inner and outer slopes respectively, $C(r,r_t,\delta r_t)$ is another truncation factor.

M 31 is the most well studied galaxy after the MW. As such, it has been constrained quite well by a variety of observations. We have chosen to use the isothermal model found by Chemin et al. (2009) to build the M 31 ICs. The specific parameters of this model are listed in Table 4.6. For IC 10, we modified the NFW mass model to a GALACTICS analogue with the same general rotation curve, gas mass, and scale lengths. The parameters for this model are also listed in Table 4.6.

Table 4.6: Summary of the model parameters.

Parameter	Units	M 31	IC 10
Halo scale velocity: σ_h	km s^{-1}	390	31
Halo scale radius: R_h	kpc	5.1	2
Inner slope:α	-	0	1
Outer slope:β	-	3	3
Halo Truncation: r_t	kpc	100	8
Halo Truncation Length: δr_t	kpc	20	3
Disk mass:M_d	10^9 $M_\odot$	59.	0.12
Disk scale length: R_d	kpc	5.6	0.3
Disk truncation: R_t	kpc	25	1.1
Disk truncation length: δR_t	kpc	3	0.1
Gas mass:M_g	10^9 $M_\odot$	10.	0.12
Gas scale length: R_g	kpc	8.5	0.9
Gas Temperature: T	K	10^4	10^4
Gas trunctation: $R_{g,t}$	kpc	40	4
Gas trunctation length: $\delta R_{g,t}$	kpc	2	0.9
Bulge Sérsic index: n	-	1.1	-
Characteristic bulge velocity:σ_b	km s^{-1}	250	-
Bulge scale length:R_b	kpc	1.3	-

4.5.2 Geometry

M 31 is located at (783 kpc, $121.2°, -21.6°$) with a radial velocity of $v_r = -300$ km s^{-1} (de Vaucouleurs et al., 1991b). van der Marel et al. (2012) utilized HST observations to determine that the proper motions of M 31 are $(-76.3,\ 45.1)$ km s^{-1} in RA and Dec. IC 10 is located at (794 kpc, $119°$, $-3.3°$) (Hunter et al., 2012) with a radial velocity of $v_r = -348$km s^{-1} (Ashley et al., 2014). Unlike many dwarf galaxies, there are measurements of IC 10's proper motions. Brunthaler et al. (2007) used the Very Large Baseline Array to see the movement of the galaxy relative to background masers. They found IC 10's proper motions to be $(-122 \pm 31,\ 97 \pm 27)$ km s^{-1} in RA and Dec.

4.5.3 Simulations

Determining the initial relative phase-space coordinates for simulation of an IC 10-M 31 system that will end up with IC 10 at the current position and velocity relative to M 31 is not a trivial task. Our solution is to essentially run each simulation twice. First, M 31 is placed at the origin and the model IC 10 system is placed at the current phase-space coordinates. With IC 10 orbiting around M 31, the system is then evolved backwards for 6 Gyr. The center-of-mass and velocity of IC 10 in the final snapshot of this first simulation is used as the initial phase-space coordinates for the forwards simulation. The IC 10 system in the final snapshot of the forwards simulation is used for our analysis. This results in a system that is close to the observed phase-space coordinates of IC 10, with some small differences caused by

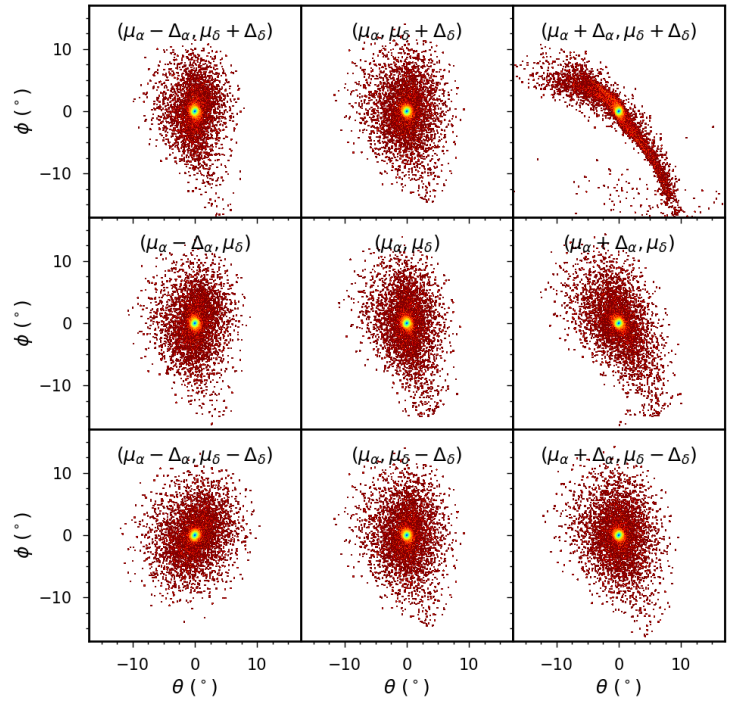

Figure 4.12: Mock images of the final state of the IC 10 gas disk in the nine simulations. The labels indicate the proper motions used to determine the initial conditions. The maps use a logarithmic surface density. The axes are in units of degrees.

dynamical friction and the disruption of the IC 10 model.

Given the relatively large uncertainty in the proper motions of IC 10, we ran a set of nine simulations exploring the range of possible tangential velocity vectors. Each simulation has 1.6×10^6 M 31 particles broken up into 2×10^5 gas particles, 3×10^5 disk particles, 10^5 bulge particles, and 10^6 halo particles, and 3×10^5 IC 10 particles, with 5×10^4 gas particles, 5×10^4 disk particles, and 2×10^5 halo particles. Each simulation was evolved for 6 Gyr using the GADGET 2 code with a softening length of 0.05 kpc. The evolution time was chosen to give IC 10 enough time to complete at least one orbit.

Figure 4.12 shows mock observations of the IC 10 gas disk at the final time step of each simulation. These observations are made using 120 arcsec pixels with a 300 arcsec beam. Most of the systems do not show clear tidal features other than a cloud of disrupted particles around the central regions. However, the simulation with $(\mu_\alpha + \Delta_\alpha, \mu_\delta + \Delta_\delta)$ shows a clear tidal stream. Therefore, there are at least some possible orbits for IC 10 that can produce tidal features.

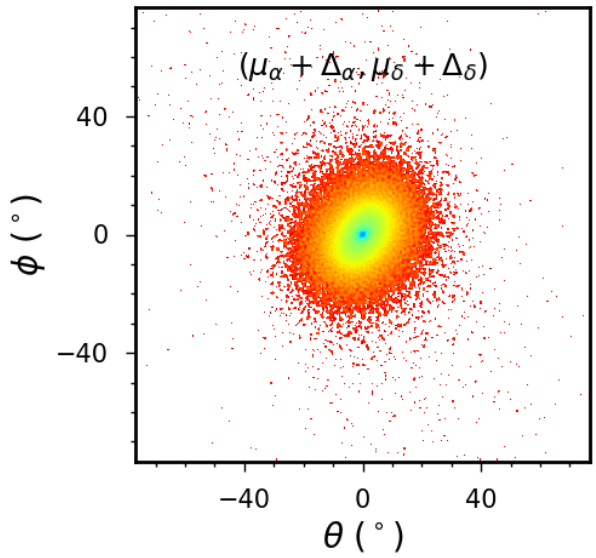

Figure 4.13: A mock observation of the $(\mu_\alpha + \Delta_\alpha, \mu_\delta + \Delta_\delta)$ snapshot using 18 arcmin pixels and truncated the surface density below 6.9×10^{18} cm^{-2}. The axes are in units of degrees.

The tidal feature seen in $(\mu_\alpha + \Delta_\alpha, \mu_\delta + \Delta_\delta)$ (top right of Fig. 4.12) is quite interesting. It is much larger than the stream-like feature in the HI disk of IC 10. Moreover, it is a very low surface-density feature. To investigate this in greater detail, Figure 4.13 is a mock image with the same pixel scale and column density as the DRAO observations. To be clear, the image is limited to a column density of 6.9×10^{18} cm^{-2}, corresponding to a surface density of 0.055 M$_\odot$pc^{-2}. Any pixel values lower than this limit are artificially set to zero. With these limits and at this scale, the image does not show strong evidence of a tidal feature as the extended tidal tails lies below the detection limit.

These results suggest that it is possible that IC 10 is on an orbit that allows for a disruption by M 31. However, the features from such a disruption are more extended than those observed. Moreover they are at a lower surface density than can be reached by current observations. Thus, it is unlikely that the actual features seen in the HI disk of IC 10 are caused by the interaction with M 31 as suggested by Nidever et al. (2013).

It is important to note that these conclusions have been reached using a limited number of simulations. While these are representative of possible orbital histories for IC 10, there is a large area of parameter space that we have yet to explore. We have not included the potential of M33, which may affect IC 10's orbital history. Nor have we varied the M 31 or IC 10 models, or explored the effects of uncertainties in distance or radial velocities.

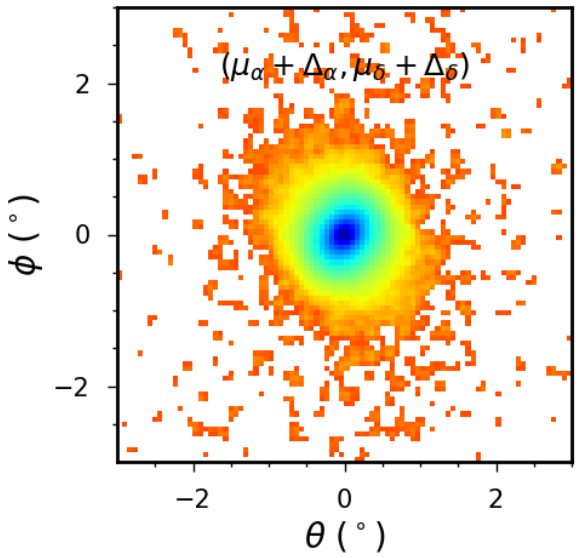

Figure 4.14: A mock observation of the $(\mu_\alpha + \Delta_\alpha, \mu_\delta + \Delta_\delta)$ snapshot using 4 arcmin pixels and truncated the surface density below 7×10^{17} cm^{-2}. The axes are in units of degrees.

Nonetheless, the results are quite interesting and suggest that further observations that reach to lower column densities be carried out. While the currently observed features are unlikely to be caused by M 31, the presence or absence of extended features will further constrain the orbital history of IC 10. Returning to the observed features, it appears that a mechanism other than the IC 10-M 31 interaction is needed to explain the observed disruption in the IC 10 disk. The simulations do rule out M31 as a source for the Southern stream. While there may be some issues with conversions, it is highly unlikely that the low column density stream of the simulation could be enhanced to such a large extent as to generate that particular feature. However, it is possible that the stream in the simulation could be related to the Northern extension. To that end, We have reproduced the GBT limited observation, see Figure 4.14. For this new image, the pixel size is $4'$, the beam FWHM is $10'$, and the image is limited to a +/- 3 degrees about the IC 10 center. This new plot does not rule out an M31 origin as the column density of the stream is near the GBT limit. We will need to compare some P-V diagrams or velocity maps in the future to be able to say anything more definitive about these results.

4.6 Summary

We have analyzed new DRAO HI observations of the blue compact dwarf galaxy IC 10 combined with simulations to study the HI morphology and kinematics, and investigate if an interaction of IC 10 with M 31 can reproduce the observed HI features we see in the outer regions of IC 10. The main outcome of this study are:

1. The compact configuration of the DRAO has allowed us to detect the extended HI disk of IC 10 further than previous HI interferometric studies. The HI mass of 7.8 × $10^7 M_\odot$ derived from our DRAO data is comparable to the HI mass derived from the single dish GBT data. We detect ~ 33% more HI mass than the VLA LITTLE THINGS data.

2. The rotation curve of IC 10 is similar in form to those of other dwarf galaxies (Namumba et al., 2017), having a linearly rising (solid body) inner portion and then turning over to become approximately flat. On the other hand, the slope of the inner part of IC 10 is ~ 3 times steeper (65 km s^{-1}/kpc) than what has been derived for most dwarf galaxies. Namumba et al. (2017, 2018) calculates the inner slopes of 21, 21, and 13 km s^{-1}/kpc for NGC 6822, Sextans A and B while Meurer et al. (1996) and Meurer et al. (1998) derive the inner slopes of 25 km s^{-1}/kpc and 22 km s^{-1}/kpc for BCD galaxies NGC 2915 and NGC 1705. We derive a mean V_{sys} = -351 ± 1.8 km s^{-1}, PA = 65 ± 4°, and i = 47 ± 6°, these values are consistent with the literature.

3. We ran mass models with a dark matter halo component. A M/L of 0.04 derived from the ISO fit is too small and does not make physical sense. On the other hand, the large errors derived for the NFW fitted parameters and the unphysical small value of the concentration parameter c suggest that this model is not suitable to explain the mass distribution of the inner disk of IC 10. Although a no dark matter model has a slightly higher reduced χ^2, we find that we can represent the kinematics of the inner disk of IC 10 without the need of a dark matter halo, which does not exclude that dark matter may exist on a larger scale in this galaxy.

4. It is unlikely that the HI features observed in IC 10 are caused by an interaction with M 31. The disruptions seen in our simulations are at lower densities and larger than those observed. We think that, as suggested by Wilcots & Miller (1998), the HI extensions with different kinematics seen south, east and west of the main core of IC 10 may be the result of accretion, as suggested by their counter-rotation and by the increase in velocity dispersion observed at the point of contact of those regions with the inner regular disk. The accreted material might be coming from the low column density HI gas that is not visible to the sensitivity of our existing telescopes.

Ashley T., Elmegreen B. G., Johnson M., Nidever D. L., Simpson C. E., Pokhrel N. R., 2014, AJ, 148, 130

Begeman K. G., 1989, A&A, 223, 47

Begeman K. G., Broeils A. H., Sanders R. H., 1991, MNRAS, 249, 523

Bekki K., 2008, MNRAS, 388, L10

Brunthaler A., Reid M. J., Falcke H., Henkel C., Menten K. M., 2007, A&A, 462, 101

Chemin L., Carignan C., Foster T., 2009, ApJ, 705, 1395

Cloet-Osselaer A., De Rijcke S., Vandenbroucke B., Schroyen J., Koleva M., Verbeke R., 2014, MNRAS, 442, 2909

Cluver M. E., et al., 2014, ApJ, 782, 90

Côté S., Carignan C., Freeman K. C., 2000, AJ, 120, 3027

Deg N., Widrow L. M., Randriamampandry T. H., Carignan C., 2018, in prep

Freeman K. C., 1970, ApJ, 160, 811

Gerbrandt S. A. N., McConnachie A. W., Irwin M., 2015, MNRAS, 454, 1000

Gil de Paz A., Madore B. F., Pevunova O., 2003, ApJS, 147, 29

Grebel E. K., 1999, in Whitelock P., Cannon R., eds, IAU Symposium Vol. 192, The Stellar Content of Local Group Galaxies. p. 17 (arXiv:astro-ph/9812443)

Huchtmeier W. K., 1979, A&A, 75, 170

Hunter D. A., Elmegreen B. G., 2006, ApJS 162, 49

Hunter D. A., Elmegreen B. G., Baker A. L., 1998, ApJ, 493, 595

Hunter D. A., et al., 2012, AJ, 144, 134

Kennicutt Jr. R. C., 1989, ApJ, 344, 685

Kim M., Kim E., Hwang N., Lee M. G., Im M., Karoji H., Noumaru J., Tanaka I., 2009, ApJ, 703, 816

Kormendy J., 1987, in de Zeeuw P. T., ed., IAU Symposium Vol. 127, Structure and Dynamics of Elliptical Galaxies. pp 17–34

Kothes R., Landecker T. L., Gray A. D., 2010, in Kothes R., Landecker T. L., Willis A. G., eds, Astronomical Society of the Pacific Conference Series Vol. 438, The Dynamic Interstellar Medium: A Celebration of the Canadian Galactic Plane Survey. p. 415 (arXiv:1010.6109)

Kuijken K., Dubinski J., 1995, MNRAS, 277, 1341

Landecker T. L., et al., 2000, A&AS, 145, 509

Lee J. C., Salzer J. J., Melbourne J., 2004, ApJ, 616, 752

Lelli F., Verheijen M., Fraternali F., Sancisi R., 2012a, A&A, 537, A72

Lelli F., Verheijen M., Fraternali F., Sancisi R., 2012b, A&A, 544, A145

Lelli F., McGaugh S. S., Schombert J. M., 2016, AJ, 152, 157

Leroy A. K., Walter F., Brinks E., Bigiel F., de Blok W. J. G., Madore B., Thornley M. D., 2008, AJ 136, 2782

Mateo M. L., 1998, ARA&A, 36, 435

Meurer G. R., Mackie G., Carignan C., 1994, AJ, 107, 2021

Meurer G. R., Carignan C., Beaulieu S. F., Freeman K. C., 1996, AJ, 111, 1551

Meurer G. R., Staveley-Smith L., Killeen N. E. B., 1998, MNRAS, 300, 705

Namumba B., Carignan C., de Blok W. J. G., Passmoor S., 2017, MNRAS, 472, 3761

Namumba B., Carignan C., Passmoor S., 2018, MNRAS, 478, 487

Navarro J. F., Frenk C. S., White S. D. M., 1997, ApJ, 490, 493

Nidever D. L., et al., 2013, ApJ, 779, L15

Noeske K. G., Iglesias-Páramo J., Vílchez J. M., Papaderos P., Fricke K. J., 2001, A&A, 371, 806

Oh S.-H., et al., 2015, AJ, 149, 180

Prugniel P., Simien F., 1997, A&A, 321, 111

Richer M. G., et al., 2001, A&A, 370, 34

Sargent W. L. W., Searle L., 1970, ApJ, 162, L155

Schlegel D. J., Finkbeiner D. P., Davis M., 1998, ApJ, 500, 525

Serra P., et al., 2015, MNRAS, 448, 1922

Shostak G. S., Skillman E. D., 1989, A&A, 214, 33

Springel V., 2005, MNRAS, 364, 1105

Taylor C., Brinks E., Skillman E. D., 1993, AJ, 105, 128

Taylor C. L., Brinks E., Grashuis R. M., Skillman E. D., 1995, ApJS, 99, 427

Taylor C. L., Brinks E., Grashuis R. M., Skillman E. D., 1996a, ApJS, 102, 189

Taylor C. L., Thomas D. L., Brinks E., Skillman E. D., 1996b, ApJS, 107, 143

Taylor A. R., et al., 2003, AJ, 125, 3145

Weldrake D. T. F., de Blok W. J. G., Walter F., 2003, MNRAS, 340, 12

Widrow L. M., Pym B., Dubinski J., 2008, ApJ, 679, 1239

Wilcots E. M., Miller B. W., 1998, AJ, 116, 2363

Winkel B., Kerp J., Flöer L., Kalberla P. M. W., Ben Bekhti N., Keller R., Lenz D., 2016, A&A, 585, A41

Wu Y., Charmandaris V., Hao L., Brandl B. R., Bernard-Salas J., Spoon H. W. W., Houck J. R., 2006, ApJ, 639, 157

de Blok W. J. G., Walter F., Brinks E., Trachternach C., Oh S.-H., Kennicutt Jr. R. C., 2008, AJ, 136, 2648

de Vaucouleurs G., de Vaucouleurs A., Corwin Jr. H. G., Buta R. J., Paturel G., Fouqué P., 1991a, Third Reference Catalogue of Bright Galaxies. Volume I: Explanations and references

de Vaucouleurs G., de Vaucouleurs A., Corwin Jr. H. G., Buta R. J., Paturel G., Fouqué P., 1991b, Third Reference Catalogue of Bright Galaxies. Volume I: Explanations and references. Volume II: Data for galaxies between 0^h and 12^h. Volume III: Data for galaxies between 12^h and 24^h.

van der Marel R. P., Fardal M., Besla G., Beaton R. L., Sohn S. T., Anderson J., Brown T., Guhathakurta P., 2012, ApJ, 753, 8

CHAPTER 5

SUMMARY AND HIGHLIGHTS

In this thesis, we investigated the HI properties of four of the local group dwarf galaxies: NGC6822, Sextans A, Sextans B, and IC 10. We collected 21 cm-line observations with the SKA pathfinder KAT-7 and the DRAO synthesis telescope. The focus of these observations has been to take advantage of the compact configurations of the two instruments to detect, if present, large scale extended HI structures which are not visible to high spatial resolution arrays such as the VLA and ATCA. The KAT-7 and the DRAO allow us to detect large scale structures of more than $\sim 30'$. Our HI data sets have column density sensitivities of $N_{HI} = 10^{18}$ to 10^{19} cm^2. Comparing this to the literature, this sensitivity is an order of magnitude higher than most previous HI observations of nearby galaxies such as the VLA LITTLE THINGS. From these observations, we carried out a comprehensive study of the HI distribution, kinematics, star formation thresholds, and possible mechanisms for the disturbed HI morphology of IC 10. Here we summarize our main results, followed by prospects of future research.

The KAT-7 datasets were reduced, calibrated and imaged using the software package CASA. The KAT-7 was initially built as an engineering test-bed for MeerKAT. In its commissioning phase, careful data inspection was carried out to ensure high quality scientific data. For this study, two major artifacts were identified in the KAT-7 data: 1) horizontal stripes in the image plane of all our cubes. These artifacts have been attributed to the presence of radio frequency interference (RFI) generated internally and seen in the radio UV plane for $|u| \leqslant 25\ \lambda$ (Carignan et al., 2016; Hess et al., 2015). The presence of these strips increased the noise in our data cubes, limiting the detection of the faint HI emission. After carrying different tests, we were

able to get rid of these artifacts by flagging data ($|u| \leqslant 10\lambda$). Moreover, in the case of NGC 6822, we uncovered further artifacts in the form of broader horizontal diagonal lines parallel to the major axis. Careful inspection of the data showed that the baseline using antennas 4 and 5 was affected. Since the cause of these artifacts was not identified, the affected baseline was removed from the final data. After getting rid of these artifacts, the noise level reduced by a factor of 2, allowing us to reach the expected theoretical noise in line free channels for NGC 6822. For Sextans A and B, the data were calibrated down to 1.5 times the theoretical noise.

In Chapter 2, the HI distribution, kinematics and star formation threshold of NGC 6822 were derived. The KAT-7 configuration ($\sim 3.5'$ spatial resolution and $T_{sys} \sim 26$ K) and the total observation time of $\sim$ 105 hrs on NGC 6822 allowed us to detect the extended gas, reaching low column densities of 1×10^{19} atoms cm^{-2}, which is an order of magnitude lower than the measured value for the ATCA observations. Due to the proximity of NGC 6822, part of our data was contaminated with Galactic HI. To accurately estimate the general properties of NGC 6822, careful subtraction of the Galactic HI was applied to the data cube using a PYTHON code. This method proved to be effective in removing the Galactic HI while retaining the galaxy flux. A flux loss of only $\sim$ 0.3% was calculated. From these observations, we find that:

- The KAT-7 intermediate spatial resolution data clearly resolves the HI features within NGC 6822 such as the HI hole as well as the arm in the south-east. The HI distribution is measured out to a diameter of $\sim 1.2^\circ$. A total HI mass of $1.3 \times 10^8 M_\odot$ is measured for NGC 6822 using the adopted distance of 0.48 Mpc. This HI mass is 23% larger than the value calculated using the ATCA observations and consistent with that detected by the single dish Parkes observations. We have derived the mid-point velocity of -55 $\pm$ 2 km s^{-1}, which corresponds to the systemic velocity found by ROTCUR.

- The rotation curve of NGC 6822 was derived from the velocity field map using a tilted ring model. The rotation curve is measured out to $\sim$ 5.8 kpc. We derive V_{sys} = -55 km s^{-1}, mean P.A. = 118°, and mean i = 66°, with very little difference between the approaching and receding sides. Our derived kinematical parameters are in agreement with the values derived from the ATCA observations (V_{sys} = -54.4 km s^{-1}, mean P.A. $\sim$ 118°, and mean $i \sim 63^\circ$). The KAT-7 RC extends to $\sim$ 1 kpc further out than the ATCA rotation curve. The larger HI extent of the KAT-7 RC comes from the increased sensitivity which allows us to detect the low column density gas in the outer radii.

- We have explored the dark matter properties in this galaxy using the pseudo-isothermal (ISO) and Navarro Frenk and White (NFW) halo models. We use the

Wide Field Infrared Survey Explorer (WISE) surface brightness profiles at 3.4 micron to account for the stellar contribution. At 3.4 microns, WISE probes the emission from the old stellar disk population and is also less affected by dust. The gas component was obtained from the KAT-7 HI column density map by applying the kinematical parameters from the tilted ring fit. The observationally motivated DM ISO model reproduces very well the observed RC while the NFW model gives a much poorer fit, especially in the inner parts. This confirms previous results that NGC 6822 has a cored and not a cuspy DM halo. Our derived best fit M/L, 0.12 ± 0.01, is consistent with the literature value of 0.10 ± 0.13. The small M/L ratio of NGC 6822 shows that the stellar distribution has no significant contribution to the total mass of the galaxy. The MOND fit fails to reproduce the observed mass distribution in NGC 6822.

- The one-dimensional Toomre-Q and cloud-growth based on shear criterion instability models have been used to describe the star formation regions in NGC 6822. We find that using the Toomre-Q criterion, the stability parameters at all radii are below the expected value of 0.63 above which the gas density is high enough for large scale star formation. This suggests that the gas density in NGC 6822 is low to effectively form stars if the Toomre-Q criterion is used to determine star formation in this galaxy. On the other hand, the stability parameters based on the cloud-growth criterion is $\geqslant 0.63$ in regions of observed star formation. This implies that the local shear rate could be a key player in cloud formation for irregular galaxies such as NGC 6822.

The HI spectral line observations of the *twin* galaxies Sextans A and B with the SKA pathfinder KAT-7 have been presented in Chapter 3. The HI distribution, kinematics, and star formation thresholds have been explored at intermediate spatial resolution. The main results from this study are as follows:

- At column densities of 5.8 and 5.4 $\times 10^{18}$ cm^{-2} for Sextans A and B, we do not detect new HI emission. In fact, our results, which are close to the GBT and VLA, contradicts the large extents and fluxes claimed by Huchtmeier et al. (1981) from the Effelsberg observations. HI masses of 7.3 $\times$ 10^7 M$_\odot$ and 4.2 $\times$ 10^7 M$_\odot$ are calculated for Sextans A and B. These values are in agreement with the VLA LITTLE THINGS results, suggesting that the two galaxies are not associated with large scale HI structures beyond the VLA resolvable angular scales.
- A tilted ring model is fitted to the HI velocity fields to derive the rotation velocities. For Sextans A, the rotation curve rises as V(R) $\propto$ R out to $\sim 250''$. The

analysis of the rotation curve of GR 8 (Carignan et al., 1990) showed that the RC of the galaxy was declining in the outer regions (see also e.g. the case of the late-type spiral NGC 7793: Dicaire et al. (2008)). We calculate a mean V_{sys} = 342 ± 0.6 km s^{-1}, P.A. = 34°, and inclination = 86°. We measure the rotation curve of Sextans B out to 650″, which corresponds to ~ 4 kpc. The rotation curve is seen to be rising out to ~ 550″. We measure mean V_{sys} = 302 ± 0.9 km s^{-1}, P.A. = 57°, and inclination = 49°, values consistent with the literature. The slight decline in the RCs of Sextans A and B should suggest the absence of dark matter. However, given the large uncertainties of the derived rotation curves and the fact that the decline is not Keplerian shows that DM is still present in these galaxies.

- Using the observed RCs as mass model inputs show that the galaxies have a higher fraction of dark matter compared to luminous matter (gas and stars). For Sextans A, regardless of the assumption made for the M/L ratio, the ISO model produces a better fit compared to the NFW at radius $\leqslant$ 1.3 kpc. Beyond that radius, the two models tend to give similar fits to the observed rotation curve. For the ISO halo models, we find the lowest χ^2 of 3.4 when the M/L value of 0.2 (Lelli et al., 2016) is used. The mass models yields DM halo parameters of $R_0 \sim 0.5$ kpc and $\rho_0 \sim 0.1$ $M_\odot$ pc^{-3}. For Sextans B, both ISO and NFW models give larger χ^2 values but again ISO model with a disk M/L of 0.2 (Lelli et al., 2016) gives the best fit to the data but with a small overestimate in rotation velocity for r < 1.3 kpc. This suggests that M/L should be slightly smaller. One thing to note from our KAT-7 mass model fits is that although we do not get perfect fits to our observed RCs, the parameters we derived for Sextans A and B are in agreement and within the ranges found for other dwarf galaxies

- We see that for both galaxies, the stability parameters derived from the Toomre-Q critical densities Σ_g/Σ_c fail to predict the observed star formation. At all radii, Σ_g/Σ_c is below the stability parameter α = 0.63, the median value from Kennicutt (1989) above which the gas density is high enough for large scale star formation. We calculate a mean α_Q = 0.25 and 0.20 for Sextans A and B by finding the ratio Σ_g/Σ_c from the center to the Holmberg radius. This result suggests that the gas surface density in Sextans A and B is low to effectively form stars if the Toomre-Q stability criterion is used to determine the star formation in these galaxies. The stability parameter based on cloud growth Σ_g/Σ_A seems better suited to explain the star formation in Sextans A and B. In both galaxies, Σ_g/Σ_A exceeds the stability parameter α_Q = 0.63 in the inner regions. We measure a mean α_A value of 0.64 and 5 for Sextans A and B respectively. Although this result may suggest that the presence of shear may play an important role in facilitating cloud formation, it is important to note that additional observa-

tions on star formation are required to make a conclusive analysis on the star formation thresholds in Sextans A and B.

Finally, in Chapter4, we analyzed new DRAO HI observations of the blue compact dwarf galaxy, IC 10. The HI morphology, kinematics of the inner disk, and the possible mechanisms for the observed chaotic HI structure of IC 10 have been presented in detail. The main outcome of this study are:

- The compact configuration of the DRAO has allowed us to detect the extended HI disk of IC 10 further than previous HI interferometric studies. For instance, the last VLA HI observations of IC 10 measure the southern plume out to $17'$ (Hunter et al., 2012) while our DRAO observations measure this feature out to $32'$. The HI profile is asymmetric with more HI around the southern extension (~-300 km s^{-1} to -250 km s^{-1}) where the HI is on scales > $15'$ not seen by the VLA. An HI mass of (7.8 ± 0.07)× 10^7 $M_\odot$ is calculated. This mass is larger by ~ 36% than the value measured from the VLA data (Ashley et al., 2014) and is in agreement within the error with the HI mass measured from the GBT data (Nidever et al., 2013). Detailed analysis of the HI cubes from the DRAO and Effelsberg data fails to detect the new faint HI feature north-west of IC 10 observed with the GBT. The feature should roughly have a signal to noise of 3 in the Effelsberg data, taking into account that the GBT and Effelsberg have the same beam size. However, there is absolutely no trace of any emission signal in the direction and velocity range of the reported feature. It is also surprising that it is not resolved in our DRAO map as it is supposed to be $10'$ or smaller. We therefore conclude that this feature is an artifact and not a real feature.
- In the inner region, the rotation curve rises slowly out to ~ 0.35 kpc. Beyond this radius the rotation velocities are almost constant and then rise slightly to the last point, with a maximum velocity ~ 30 km s^{-1}. We find the kinematical V_{sys} = -351 ± 1.8 km s^{-1}, this value is different from the V_{sys} of -339 ± 6 km s^{-1} derived from the global profile due to the asymmetry of the system. A mean PA = 65 ± 4 ° and i = 47 ± 6 ° are found, these values are consistent with the literature.
- We ran mass models with a dark matter halo component. A M/L of 0.04 derived from the ISO fit is too small and does not make physical sense because it is so low. On the other hand, the large errors derived for the NFW fitted parameters and the unphysical small value of the concentration parameter c suggest that this model is not suitable to explain the mass distribution of the inner disk of IC 10. Although a no dark matter model has a slightly higher reduced χ^2, we find that we can represent the kinematics of the inner disk of IC 10 without

the need of a dark matter halo. In this case, a M/L of 0.17 ± 0.08 is obtained. This value is closer to a M/L of 0.2 expected at the lower end for most dwarf galaxies as derived by Lelli et al. (2016). Comparing with the results of other BCDs from the literature, Lelli et al. (2012a) and Lelli et al. (2012b) showed that baryons may dominate the gravitational potential in the inner regions of UGC 4483 and I ZW 18, with the stellar component contributing ~ 50% of the observed rotation curve of UGC 4483. This could suggest, as from our result of IC 10, that the kinematics of the inner disks of most BCDs can be described without a dark matter halo.

- It is unlikely that the HI features observed in IC 10 are caused by an interaction with M 31. The disruptions seen in our simulations are at lower densities and larger than those observed. Follow up studies with high sensitivity HI observations with telescopes such as MeerKAT and ultimately the SKA will be necessary to detect such faint features, if they exist. We think that, as suggested by Wilcots & Miller (1998), the HI extensions with different kinematics seen south, east and west of the main core of IC 10 may be the result of accretion, as suggested by their counter-rotation and by the increase in velocity dispersion observed at the point of contact of those regions with the inner regular disk.

5.1 Future prospects

The results presented in this thesis provide enormous opportunity for continued research. There are several lines of research arising from this work which should be pursued:

- In this thesis, we studied 4 nearby gas rich dwarf galaxies. A detailed study of the HI properties in each individual galaxy has been performed. To obtain better statistics and a more extensive comparison between the properties of these systems, a larger sample would be essential for future studies.
- Our intermediate spatial resolution HI observations have revealed that even neutral hydrogen mass resided in the outer discs of most nearby dwarf galaxies, strengthening the conclusion that a vast, nearly untapped gas reservoir is present in these systems. These observations have allowed us to accurately determine the general properties such as HI mass, HI flux, HI diameter, and line widths. To further investigate the presence of lower column density HI emission beyond our observing limit, it would be interesting to extend this study with telescopes such as MeerKAT. MeerKAT combination of high to intermediate spatial resolution combined with high sensitivity will allow us to probe even lower column densities < 10^{18} cm^{-2} than KAT-7, making it possible to trace even the faintest HI emission if present.

- We have studied the star formation thresholds in dwarf irregular galaxies. These results suggest that shear plays an important role in facilitating cloud formation which leads to star formation. The next step will be to explore the relevance of direct gas accretion in relation to star formation in dwarf galaxies. Dwarf galaxies have been implicitly assumed to grow mostly through mergers, while the relevance of direct gas accretion in dwarf galaxies has never been scrutinized. The lack of studies of the tenuous gas in and around dwarf galaxies has not been explored in detail because it has been very expensive to obtain the required high resolution high sensitivity observations of the extended low column density outskirts of these galaxies. With MeerKAT ready for science, data from the MeerKAT HI Observations of Nearby Galactic Objects: Observing Southern Emitters (MHONGOOSE) survey (de Blok et al., 2016) will be used to uncover possible signatures of gas accretion properties and feedback, inflow, and outflows of neutral gas.

- This study has focused on understanding the properties of nearby gas rich dwarf galaxies using HI. Neutral hydrogen, the raw material from which stars form, plays an important role in the various processes that occur in galaxies. A detailed analysis of the HI kinematics (rotation curve) can reveal important physical characteristics of the rotating material. These physical quantities regulate the gravitational stability and, consequently, the large scale distribution and properties of star formation in galaxies. The next step will be to combine detailed HI kinematics with other multi-wavelength data to explore the link between HI and star formation processes such as star formation thresholds, star formation rates, and star formation histories.

- In the recent past, there has been distinct differences between the observed and simulated dark matter distribution in galaxies. These differences have been associated to, among others, lack of detailed kinematical analysis. The inner parts of the rotation curves are a key tool to distinguish between cuspy or cored DM profiles and therefore must be derived with care. In this study, the rotation velocities are derived from the tilted-ring model by fitting of 2D velocity fields. Although the tilted-ring model returns good kinematic models, one of the main problems with using this method is however beam smearing (Di Teodoro & Fraternali, 2015). The finite beam size of the telescope causes the gradients in the velocity fields to become flatter, therefore underestimating the inner rotation velocities. The next step will be to extend this study and use 3D kinematical analysis which allows for the derivation of the rotation curve without the effect of beam smearing for the detailed analysis of dark matter distribution of galaxies.

- Choosing a constant inclination to derive the rotational velocities is not an ideal

case when the position angle of a galaxy is changing. As much as ROTCUR correctly approximates the galaxy position angle, in most cases, it fails to give good solutions for the inclinations. As seen from this work, the inclinations tend to be randomly distributed across the entire radii making it difficult to to fit their radial distribution. The most realistic approach is to choose a constant inclination to determine a model that agrees well with the observed kinematics of galaxies. Future work will require the use of new techniques being developed to address this issue.

Ashley T., Elmegreen B. G., Johnson M., Nidever D. L., Simpson C. E., Pokhrel N. R., 2014, AJ, 148, 130

Carignan C., Beaulieu S., Freeman K. C., 1990, AJ, 99, 178

Carignan C., Libert Y., Lucero D. M., Randriamampandry T. H., Jarrett T. H., Oosterloo T. A., Tollerud E. J., 2016, A&A, 587, L3

Di Teodoro E. M., Fraternali F., 2015, MNRAS, 451, 3021

Dicaire I., Carignan C., Amram P., Marcelin M., Hlavacek-Larrondo J., de Denus-Baillargeon M.-M., Daigle O., Hernandez O., 2008, AJ, 135, 2038

Hess K. M., Jarrett T. H., Carignan C., Passmoor S. S., Goedhart S., 2015, MNRAS, 452, 1617

Huchtmeier W. K., Seiradakis J. H., Materne J., 1981, A&A, 102, 134

Hunter D. A., et al., 2012, AJ, 144, 134

Kennicutt Jr. R. C., 1989, ApJ, 344, 685

Lelli F., Verheijen M., Fraternali F., Sancisi R., 2012a, A&A, 537, A72

Lelli F., Verheijen M., Fraternali F., Sancisi R., 2012b, A&A, 544, A145

Lelli F., McGaugh S. S., Schombert J. M., 2016, AJ, 152, 157

Nidever D. L., et al., 2013, ApJ, 779, L15

Wilcots E. M., Miller B. W., 1998, AJ, 116, 2363

de Blok W. J. G., et al., 2016, in Proceedings of MeerKAT Science: On the Pathway to the SKA. 25-27 May, 2016 Stellenbosch, South Africa (MeerKAT2016). Online at <A href="href=">href="https://pos.sissa.it/cgi-bin/reader/conf.cgi?confid=277</A>, id.7. p. 7 (arXiv:1709.08458)